



HAL
open science

Modeling of underexpanded reactive CO₂-into-sodium jets, in the frame of sodium fast reactors

Daniele Vivaldi

► **To cite this version:**

Daniele Vivaldi. Modeling of underexpanded reactive CO₂-into-sodium jets, in the frame of sodium fast reactors. Chemical and Process Engineering. Ecole Nationale Supérieure des Mines de Saint-Etienne, 2013. English. NNT : 2013EMSE0707 . tel-01082806

HAL Id: tel-01082806

<https://theses.hal.science/tel-01082806>

Submitted on 14 Nov 2014

HAL is a multi-disciplinary open access archive for the deposit and dissemination of scientific research documents, whether they are published or not. The documents may come from teaching and research institutions in France or abroad, or from public or private research centers.

L'archive ouverte pluridisciplinaire **HAL**, est destinée au dépôt et à la diffusion de documents scientifiques de niveau recherche, publiés ou non, émanant des établissements d'enseignement et de recherche français ou étrangers, des laboratoires publics ou privés.

THÈSE

présentée par

Daniele VIVALDI

pour obtenir le grade de
Docteur de l'École Nationale Supérieure des Mines de Saint-Étienne

Spécialité : Génie des procédés

MODELING OF UNDEREXPANDED REACTIVE CO₂-INTO-SODIUM JETS, IN THE FRAME
OF SODIUM FAST REACTORS

soutenue à Cadarache, le 4 Octobre 2013

Membres du jury

| | | |
|----------------------|--------------------|--|
| Rapporteurs : | Michel Lance | Professeur, Université Claude-Bernard Lyon 1 |
| | Jean-Pierre Bellot | Professeur, Ecole des Mines de Nancy |
| Président du jury : | Marco Ricotti | Professeur, Politecnico di Milano |
| Examineurs : | Philippe Grosseau | Professeur, Ecole des Mines de Saint Etienne |
| | Craig Gerardi | Docteur, Argonne National Laboratory |
| | Pierre Coste | Ingénieur, Commissariat à l'Energie Atomique |
| | Christophe Perrais | Docteur, Commissariat à l'Energie Atomique |
| Directeur de thèse : | Frédéric Gruy | Professeur, Ecole des Mines de Saint Etienne |

Alla mia mamma e al mio papà

Abstract

This PhD work was motivated by the investigations in the frame of supercritical CO₂ Brayton cycles as possible energy conversion cycles for the Sodium-cooled Fast nuclear Reactors (SFRs). This technology represents an alternative to conventional steam Rankine cycles, with the main advantage represented by the elimination of the accidental sodium-water reaction scenario. Nevertheless, CO₂ chemically reacts with sodium, through an exothermic reaction leading to solid reaction products, mainly sodium carbonate. Following an accidental leakage inside the sodium-CO₂ heat exchanger of a SFR, the CO₂, having an operating pressure of about 200 bars, would be injected into the low-operating-pressure liquid sodium, creating an underexpanded reactive CO₂-into-sodium jet. The underexpanded jet features a sonic gas injection velocity and an underexpansion in the first region downstream the leakage, where the CO₂ is accelerated to supersonic velocities. The exothermic reaction between the CO₂ and the sodium causes an increasing of the temperature inside the heat exchanger.

An experimental facility was built at CEA Cadarache, for the realization of CO₂-into-sodium jets: this facility has provided preliminary results in terms of temperature variations inside the jet due to the exothermic reaction. However, this type of experimental tests are complicated to realize and to analyse, due to the technical difficulties of realizing the contact between CO₂ and sodium, and to the uncertainties of temperature measurement inside a two-phase high velocity jet. It follows that a numerical model of this kind of jets is required, in order to comprehend the CO₂-sodium kinetics of reaction inside the jet and being able to transpose the phenomenon to relevant SFR sodium-CO₂ heat exchangers. This would allow to understand the consequences of a leakage inside a sodium-CO₂ heat exchanger, in terms of, for instance, temperature profiles inside the heat exchanger and on tube surfaces, and reaction products concentration profiles.

The goal of this PhD work is the development of a numerical model of the two-phase reactive CO₂-into-sodium jet.

As a first step, experimental and bibliographic studies on underexpanded non-reactive gas-into-liquid jets have been investigated, in order to understand what types of two-phase patterns characterise the jet: a first region has been identified, close to gas injection, featuring a mist flow of liquid droplets inside continuous gas, whereas a region further downstream the gas injection is characterised by bubbly flow. The informations obtained have been employed for the development of a numerical model of an underexpanded non-reactive gas-into-liquid jet, adopting a 3D unsteady multi-fluid CFD approach. An experimental facility, employing optical probe technique, was developed for the void fraction measurement inside the two-phase jet, in order to perform a comparison with the numerical results. It is found that numerical results well agree with the experimental ones.

Once the underexpanded non-reactive jet numerical model was validated, the following step was the development of a numerical model for the chemical

reaction between sodium and CO₂. The approach takes into consideration the specific contact mechanism between the CO₂ and the sodium: one model for the reaction of a liquid sodium droplet with the surrounding CO₂ and one model for the reaction of a CO₂ bubble with the surrounding liquid sodium were separately developed. These models allow to determine the depletion rate of droplets and bubbles, as a function of the main influencing parameters, such as temperature and reaction kinetics parameters.

The results obtained through the chemical reaction models have been used for building correlations describing the sodium (or CO₂) reaction rate, as a function of the influencing parameters. These correlations have been implemented inside the non-reactive jet model, in order to add the chemical reaction. The resulting model allows to determine the temperature profiles inside the reactive jet, as a function of the different reaction kinetics parameters employed, and the CO₂ penetration length before its completed consumption by the chemical reaction. The numerical temperature profiles have been compared with the ones obtained experimentally, in order to understand which kinetics of reaction employed in the numerical model give the results closest to the experimental values.

The numerical model here developed can be applied to real sodium-CO₂ heat exchanger geometries, in order to obtain informations about the temperature profiles inside the heat exchanger, temperature and mechanical stresses on tubes, and reaction products distribution.

The model can be easily adapted to the investigation of other jets, such as the steam-into-sodium jets developed following an accidental leakage inside the steam generator of a SFR coupled with a steam Rankine cycle.

Résumé

Ce travail de thèse s'est inscrit dans le contexte d'utilisation d'un cycle de conversion de l'énergie de type Brayton au CO₂ supercritique, pour les réacteurs à neutrons rapides refroidis au sodium (RNRNa). Cette technologie représente une alternative aux cycles Rankine conventionnels à vapeur d'eau, ayant pour avantage principal l'élimination du scénario de réaction accidentelle sodium-eau. Cependant, le CO₂ réagit chimiquement avec le sodium, avec une réaction exothermique donnant des produits de réaction solides, dont le principal est le carbonate du sodium. Dans le cas d'une fuite accidentelle dans l'échangeur de chaleur Na – CO₂ d'un RNRNa, le CO₂, avec une pression opérative d'environ 200 bars, serait injecté dans le sodium liquide qui se trouve à basse pression, provoquant un jet sous-détendu et réactif de CO₂ dans le sodium. Le jet sous-détendu est caractérisé par une vitesse de sortie sonique et une expansion dans la région en aval de la fuite, où le CO₂ est accéléré à des vitesses supersoniques. La réaction exothermique entre le CO₂ et le sodium provoque une augmentation de la température dans l'échangeur de chaleur.

Un dispositif expérimental a été développé au CEA Cadarache, pour la mise en œuvre de jets de CO₂ dans du sodium liquide : ce dispositif a donné des premiers résultats en terme d'augmentation de température obtenue dans le jet du fait de la réaction exothermique. Cependant, ce type d'essais expérimentaux est difficile à réaliser et à exploiter, à cause de la difficulté technique de mise en œuvre du contact CO₂–Na et de l'incertitude des mesures de température au sein d'un jet diphasique à haute vitesse. Par conséquent, un modèle numérique de ce type de jet est requis, pour comprendre les cinétiques de la réaction CO₂–Na au sein du jet et pouvoir transposer le phénomène à des géométries réelles d'échangeur Na – CO₂ des RNRNa. Cela permettrait de connaître les conséquences d'une fuite dans un échangeur Na – CO₂, en termes, par exemple, de profils de température dans l'échangeur et sur la surface des tubes, et de profils de concentration des produits de réaction.

L'objectif principal de ce travail de thèse était le développement d'un modèle numérique du jet réactif diphasique de CO₂ dans du sodium.

Dans une première étape, les jets sous-détendus non-réactifs de gaz dans du liquide ont été étudiés d'un point de vue expérimental et bibliographique, pour comprendre les types d'écoulements diphasiques présents au sein du jet : une première région a été identifiée, près du point d'injection du gaz, caractérisée par un écoulement à goutte de liquide dans le gaz, tandis qu'une région plus éloignée a été caractérisée par des bulles de gaz dans le liquide. Les informations obtenues ont été utilisées pour le développement d'un modèle numérique d'un jet sous-détendu non-réactif de gaz dans du liquide, utilisant une approche 3D non-stationnaire de type multi-fluide CFD. Un dispositif utilisant une fibre optique pour la mesure du taux de gaz dans le jet a été développé, de façon à pouvoir réaliser une comparaison avec les résultats numériques du modèle. Les résultats numériques sont en bon accord avec les résultats expérimentaux, en termes de profils axial et radiaux du taux de vide.

Une fois le modèle numérique du jet sous-détendu non-réactif validé, l'étape suivante a été le développement d'un modèle décrivant la réaction chimique

entre le sodium et le CO_2 . L'approche prend en compte le contact spécifique entre le CO_2 et le sodium dans le jet : un modèle de réaction entre une goutte de sodium liquide et le CO_2 gazeux et un modèle de réaction entre une bulle de CO_2 avec le sodium liquide ont été développés séparément. Les modèles permettent d'obtenir les taux de disparition des gouttes et des bulles, en fonction des principaux paramètres, comme la température et les paramètres cinétiques de réaction.

Les résultats des modèles de réaction chimique ont été utilisés pour obtenir des corrélations décrivant le taux de réaction du sodium (ou du CO_2), en fonction des paramètres influents. Ces corrélations ont été implémentées dans le modèle du jet non-réactif, de façon à y introduire la réaction chimique. Le modèle résultant permet de calculer les profils de température obtenus au sein du jet, en fonction des paramètres cinétiques de réaction utilisés, ainsi que la longueur de pénétration du CO_2 avant sa totale consommation par la réaction chimique. Les profils de température calculés numériquement ont été comparés avec les profils obtenus expérimentalement, de façon à comprendre quelle cinétique de réaction utilisée numériquement donne les résultats les plus proches des valeurs obtenues expérimentalement.

Le modèle développé peut être appliqué à des géométries réelles d'échangeur Na – CO_2 , pour obtenir des informations sur les profils de température dans l'échangeur, les températures et les contraintes mécaniques sur les tubes, ainsi que la distribution des produits de réaction. Le modèle peut être facilement transposé à l'étude d'autres jets, comme par exemple, des jets de vapeur d'eau dans du sodium liquide, suite à une fuite accidentelle dans le générateur de vapeur d'un RNRNa avec cycle Rankine à eau.

Remerciements

Un grand nombre de personnes ont contribué, pendant ces trois années de travail, à l'obtention d'importants résultats qui m'ont permis de soutenir ma thèse de doctorat.

Ma première pensée va à Nicole Simon, qui a élaboré le sujet de thèse en 2010 et m'a choisi comme doctorant. Son aide et son attention vers chaque aspect du travail ont été fondamentaux, j'ai beaucoup appris par son esprit de vie, sa façon d'être et de travailler. Le destin a décidé de me priver de la possibilité de pouvoir la remercier, mais cela ne m'empêchera pas de me rappeler d'elle chaque fois que je penserai à cette période de ma vie.

C'est simplement impossible de pouvoir exprimer tout mon remerciement pour Professeur Frédéric Gruy, sûrement la personne qui a enrichi le plus ma connaissance scientifique dans toute ma vie. Chaque jour passé à l'Ecole des Mines de Saint-Etienne en discutant ensemble a représenté pour moi une possibilité d'approfondissement des mes compétences et de ma rigueur scientifiques. Je le suis redevable pour toutes les heures et tous les jours qu'il m'a dédiés pendant ces trois ans, j'ai beaucoup apprécié sa volonté de toujours m'aider, et je lui en serai toujours reconnaissant.

Un merci particulier, je veux le dédier à Christophe Perrais, chef du "Laboratoire d'études des Interactions et Procédés sur les Caloporteurs" (LIPC) du CEA-Cadarache, dont j'ai fait partie pendant trois ans. Son management, son aide et sa disponibilité ont contribué significativement à mon enrichissement personnel et à la qualité de mon travail. Je dois aussi le remercier pour toutes les conférences et les cours auxquels j'ai pu participer, cela m'a donné la possibilité de présenter mes travaux à l'international et d'améliorer mes compétences sur des thématiques spécifiques du génie nucléaire.

Quand, en octobre 2010, je suis arrivé au CEA depuis l'Italie, je ne connaissais pas un seul mot de français. Mais j'ai eu la chance de travailler dans un laboratoire de personnes fantastiques, où je me suis senti tout de suite comme chez moi: je veux remercier mes collègues Anna, Karine, Michelle, Nayiri, Marie et Marie, Audrey, Thierry, Pierre, Laurent, Jérémy, Thomas, Aurélien, Serge, Nicolas, Alice, avec qui j'ai passé la plupart de mes repas et aussi des moments très sympas hors du contexte professionnel.

J'ai apprécié d'avoir pu travailler avec Serge Trambaud: on a passé des journées entières habillés avec la confortable "combinaison orange anti-Sodium", travaillant intensément pour obtenir quelques résultats expérimentaux exploitables. Même si un an et demi d'essais n'ont pas suffi pour obtenir ces résultats, je le remercie pour le temps qu'il m'a dédié, et parce que l'expérience que j'ai accumulée travaillant avec le sodium solide et liquide a sûrement été unique et très enrichissante.

Je veux remercier Christine Biscarrat, Silvain Madeleine, Lionel Cachon and Christophe Garnier du LCIT, pour m'avoir accueilli dans leur laboratoire pour pouvoir réaliser mes calculs numériques. Je suis conscient d'y avoir passé beaucoup plus de temps de ce que j'avais prévu initialement, et je les remercie pour

m'avoir laissé tout le temps dont j'ai eu besoin pour pouvoir compléter de façon adéquat mon travail.

Quand j'ai proposé la volonté de réaliser des mesures expérimentales de taux de vide, je n'aurais jamais pu penser que le dispositif expérimental aurait été développé et terminé en seulement un mois. Si cela a été possible, je dois tout d'abord beaucoup remercier Eric Hervieu, qui m'a dédié un temps précieux pour me transmettre les compétences fondamentales concernant les mesures expérimentales des écoulements diphasiques. Je ne peux pas oublier le rôle fondamental de Gilles Gobillot, et de le remercier pour avoir réalisé tous les travaux techniques nécessaires pour le dispositif en seulement deux semaines.

Je remercie Gilles Rodriguez, pour m'avoir guidé avec son management, pour m'avoir constamment fourni documents et articles techniques utiles, pour m'avoir toujours aidé dans de nombreuses occasions quand j'en avais besoin, pour m'avoir proposé de contribuer à des projets externes à la thèse, et enfin pour m'avoir donné la possibilité de participer et présenter mes travaux à des meetings internationaux. Je considère cette dernière opportunité comme un aspect valorisant, très positif et formateur de ma période de thèse.

Un autre remerciement particulier s'adresse à Christian Latge, pour son intérêt constant dans l'avancement des mes travaux scientifiques, pour ses commentaires très enrichissants concernant diverses problématiques techniques, et enfin pour son aide fondamentale pour chaque aspect de mon expérience de thèse au CEA.

Je remercie Pierre Charvet, pour sa disponibilité et son aide indispensable concernant les problématiques informatiques relatifs à mes calculs CFD.

Je remercie Nicolas Alpy, Thierry Cadiou et Gilles Avakian pour leur aide et pour les discussions et réunions enrichissantes qu'on a eu ensemble.

Je remercie Leila Gicquel, pour les conseils qu'elle m'a donné et pour le constant aide pratique pendant ces trois ans.

Je remercie Francesco Vitillo, pour les discussions hautement scientifiques qu'on a constamment eues ensemble, pour sa contribution technique en plusieurs aspects de mon travail, et enfin pour son amitié.

Je ne peux pas oublier de remercier Denis Tschumperlè et tout l'équipe d'Ansys Fluent France, pour leur disponibilité et leur aide. Je souhaite aussi remercier Sergio Vasquez-Malebran d'Ansys.

Je remercie Professeur Marco Ricotti, pour toute la connaissance technique qu'il m'a transmis et pour l'aide et les conseils indispensables qu'il m'a constamment fourni depuis quand j'ai eu la chance de réaliser ma thèse de Master of Science avec lui au Politecnico di Milano.

Je tiens également à souligner la gentillesse de tous mes collègues de travail durant ces trois années de thèse.

Au-delà de toutes ces personnes avec qui j'ai travaillé pendant ma période de thèse au CEA de Cadarache, je ne peux pas oublier les personnes fondamentales de ma vie personnelle, grâce auxquelles j'ai pu atteindre cet objectif. Tout d'abord, merci Mamma et Papi, pour l'exemple que vous avez été et vous êtes pour moi, pour les valeurs que vous m'avez apprises, pour être toujours

à côté de moi pendant les choix importants de ma vie et pour faire toujours tout le possible pour m'aider. Merci Mélanie pour me supporter (en tous les sens), pour me montrer toujours la bonne route à suivre et pour être toujours à côté de moi. Merci Silvia pour être la meilleure sœur du monde. Je tiens à remercier mon Nonno, une personne spéciale qui, pour son caractère, sa sagesse et sa culture, a toujours représenté un exemple à suivre pour moi. En fin, je remercie mes Nonne.

Contents

| | |
|---|-----------|
| Contents | 1 |
| 1 Context and scope of the work | 3 |
| 1.1 Context | 3 |
| 1.2 Sodium Fast Reactors and Supercritical CO ₂ Brayton cycles | 6 |
| 1.3 Scope of the work | 10 |
| 1.4 Thesis outline | 13 |
| 2 Bibliographic study | 15 |
| 2.1 Bibliography on underexpanded gas-into-liquid jets | 15 |
| 2.1.1 Experimental studies | 15 |
| 2.1.1.1 Gas-into-liquid versus gas-into-gas underexpanded jets | 15 |
| 2.1.1.2 Entrained droplet size | 17 |
| 2.1.1.3 Temperature profiles | 23 |
| 2.1.2 Modeling studies | 26 |
| 2.1.3 Assessment of the studies on underexpanded gas-into-liquid jets | 29 |
| 2.2 Bibliography study on sodium-CO ₂ reaction | 30 |
| 2.2.1 Studies by the Japan Atomic Energy Agency (JAEA) | 30 |
| 2.2.2 Studies by the Korea Atomic Agency Research Institute (KAERI) | 31 |
| 2.2.3 Studies by the CEA | 33 |
| 2.2.4 Assessment of the experimental studies on sodium – CO ₂ reactions | 34 |
| 3 The experimental facilities | 37 |
| 3.1 Experimental study on CO ₂ -into-sodium jets | 37 |
| 3.1.1 Facility | 37 |
| 3.1.2 Experimental conditions and test procedures | 38 |
| 3.2 Experimental study on underexpanded gas-into-water jets | 41 |
| 4 Non-reactive gas-into-liquid jet | 44 |
| 4.1 Modeling approach | 45 |
| 4.1.1 Preliminary considerations | 45 |
| 4.1.2 Two-phase flow modeling approach | 49 |
| 4.1.3 Euler-Euler interfacial momentum closure laws | 53 |
| 4.1.4 Interfacial friction and heat transfer for underexpanded gas-into-liquid jets | 56 |

| | | |
|----------|--|------------|
| 4.1.5 | Turbulence modeling | 61 |
| 4.2 | Results and validation | 65 |
| 4.2.1 | Computational geometry and numerical details | 66 |
| 4.2.2 | Velocity profiles | 72 |
| 4.2.3 | Pressure profiles | 75 |
| 4.2.4 | Void fraction profiles | 76 |
| 4.2.5 | Final remarks | 81 |
| 5 | Sodium-CO₂ chemical reaction model | 87 |
| 5.1 | Sodium droplet reaction | 89 |
| 5.1.1 | Model equations and boundary conditions | 90 |
| 5.1.2 | Solving method | 93 |
| 5.1.3 | Results | 99 |
| 5.2 | CO ₂ bubble reaction | 105 |
| 5.2.1 | Model equations and boundary conditions | 106 |
| 5.2.2 | Solving method | 107 |
| 5.2.3 | Results | 108 |
| 5.3 | Integral method for depletion rate calculation | 111 |
| 5.3.1 | The integral method for the CO ₂ bubble | 111 |
| 5.3.2 | The integral approach for the sodium droplet | 113 |
| 6 | Reactive CO₂-into-sodium jet | 115 |
| 6.1 | Modeling approach | 116 |
| 6.1.1 | Mass transfer due to chemical reaction | 117 |
| 6.1.2 | Momentum transfer due to chemical reaction | 118 |
| 6.1.3 | Heat transfer due to chemical reaction | 119 |
| 6.1.4 | Species transport equation | 119 |
| 6.2 | Implementation of the chemical reaction into the two-fluid model | 120 |
| 6.2.1 | Reaction rate for droplet flow ($\alpha \geq \alpha_d$) | 121 |
| 6.2.2 | Reaction rate for bubbly flow ($\alpha \leq \alpha_b$) | 123 |
| 6.2.3 | Reaction rate for the transition flow ($\alpha_b < \alpha < \alpha_d$) | 124 |
| 6.3 | Results | 125 |
| 6.3.1 | Preliminary considerations on experimental results | 125 |
| 6.3.2 | Numerical results and validation | 129 |
| 6.3.2.1 | Numerical details | 129 |
| 6.3.2.2 | Numerical results | 129 |
| | Bibliography | 144 |

Chapter 1

Context and scope of the work

List of most cited acronyms:

- CEA: Commissariat à l'énergie atomique et aux énergies alternatives
- AGR: Advanced Gas-cooled Reactor
- MOX: Mixed OXide fuel
- FR: Fast Reactor
- FBR: Fast Breeder Reactor
- SFR: Sodium-cooled Fast Reactor
- GFR: Gas-cooled Fast Reactor
- LFR: Lead-cooled Fast Reactor
- ASTRID: Advanced Sodium Technological Reactor for Industrial Demonstration
- SWR: Sodium-Water Reaction
- sCO₂: supercritical carbon dioxide
- SCR: Sodium-CO₂ Reaction

1.1 Context

As of May 2013, there are 436 operational nuclear reactors worldwide, corresponding to a total capacity of 372,686 MWe [1]. In 2012, the nuclear generation was 2.351 BkWh, corresponding to a contribution of 12.3 percent of the world electricity production [2][1].

Based on the International Energy Outlook 2011 Reference case assessed by the U.S. Energy Information Administration (EIA) [3], world marketed energy consumption grows by 53 percent from 2008 to 2035. Total world energy use rises from 505 quadrillion British thermal units (Btu) in 2008 to 619 quadrillion Btu in 2020 and 770 quadrillion Btu in 2035. In this projection period, world demand for electricity increases by 2.3 percent per year from 2008 to 2035,

for a world net electricity generation increase of 84 percent, passing from 19.1 trillion kWh in 2008 to 25.5 trillion kWh in 2020 and 35.2 trillion kWh in 2035. Although the 2008-2009 global economic recession slowed the rate of growth in electricity use in 2008 and resulted in negligible change in electricity use in 2009, worldwide electricity demand increased by an estimated 5.4 percent in 2010.

Nuclear energy represents one of the main candidates for facing this growing trend of electricity consumption. Taking a look at the two countries with the highest nuclear capacity in the world, U.S. and France, the average age of their commercial reactors is 32 and 28 years, respectively. Considering the current assumed 40-year reactor life-time, a significant investment on new nuclear units has to be expected for the next decades.

Current nuclear electricity production is based on the so-called thermal-reactor technology. This nomenclature comes from the fact that nuclear fissions are induced by neutrons at thermal energies (lower than 1eV). The uranium-235 is the fissile isotope used in thermal reactors: neutrons generated by its nuclear fission have an average energy of about 2 MeV. In order to slow down neutron's energy to thermal values, a moderator is required: among the possible moderator technologies, water is the most commonly employed in current thermal reactors. Even when not employed as moderator, water is always (with the exception of the English AGRs) present as coolant in thermal reactors, aimed at transferring heat from the nuclear fuel to the electricity production cycle.

Considering that the isotope 235 represents only the 0.7% of the natural uranium (the remaining 99.3% being composed mainly by the isotope 238), current thermal reactors can make use of only a small part of total natural uranium. Thermal reactors require nuclear fuel enriched in fissile isotope 235, from the natural 0.7% to 3 to 5%: this represents the only portion of fuel available for energy production during the reactor operation (in reality, another energy source must be taken into account during a fuel cycle, represented by the fission of a portion of plutonium-239 generated by neutron absorption of uranium-238). The global energy efficiency (ratio between energy produced and amount of fuel introduced) increases when one takes into account spent fuel reprocessing for the separation of plutonium and its reutilization as MOX fuel; but fissile plutonium represents only about 1% of spent fuel mass inventory, and, generally, spent fuel reprocessing for MOX production is achievable only once, since further reprocessing leads to a significant increase of actinides production at the end of the MOX fuel cycle.

In order to keep nuclear energy a reliable source of electricity for the future, an improvement in uranium utilization is needed, provided that uranium is a fossil resource and that its availability will allow the operation of the worldwide installed current reactor technology for an estimated period of 65 years [4]. In this context, Fast Reactors (FRs) represent a technology originally conceived to burn uranium more efficiently and thus extend the world's uranium resources: estimations say that a factor of about 60 could be achieved [5]. In FRs, moderation is avoided, in order to employ fast spectrum neutrons: in this region (0.1 - 1 MeV), the ratio between U-235 fission cross-section and U-238 capture cross-section is significantly lower than in the thermal spectrum, meaning that much more U-238 capture events occur in the fast spectrum than in the thermal one. The capture of extra neutrons by U-238 leads to U-239,

which in turn undergoes a series of decays to form Pu-239. Pu-239 is the fissile isotope used in FRs. Compared to thermal reactors, a much higher enrichment in fissile isotopes is required for the fresh fuel in order to achieve criticality in a FR, due to more prominent U-238 captures. Nevertheless, while this fissile part is burned during reactor operation, new fissile material is generated by U-238 captures: in this way, FRs can be designed even to produce more plutonium than they consume (Fast Breeder Reactors - FBRs).

Since transuranic nuclides (Pu-238, Pu-240, Pu-242, Am-241, Am-243, Cm-244 and Cm-246), have much higher probabilities to undergo fission in a fast neutron spectrum than in a thermal one, much lower accumulation of highly radioactive long-lived minor actinides results from the operation of a FR, compared to thermal reactors. Moreover, FRs give the possibility of burning minor actinides produced by thermal reactors in order to transmute them into short-lived nuclides with lower radiotoxicities.

With the International Generation IV Forum (GIF) in 2000, a new generation of nuclear reactors was proposed: a roadmap was elaborated so that the future nuclear power plants should improve safety, sustainability (reduced demand of fossil resources, treatment and disposal of wastes), economical competitiveness and proliferation resistance. Six different concepts of reactors are proposed for Generation IV. Three of them are based on thermal neutrons technology, preserving water as a cooling fluid but under supercritical conditions, or using a gas, for instance helium, at high pressure/temperature. The other concepts are based on the fast reactor technology. In Europe, the Strategic Research Agenda (SRA) of the Sustainable Nuclear Energy Technology Platform (SNETP) has identified three FR technologies as eligible routes towards the deployment of a sustainable nuclear energy supply chain: SFRs (Sodium-cooled fast reactors), LFRs (Lead-cooled fast reactors) and GFRs (Gas-cooled fast reactors) technologies. Among the possible FR technologies, SFRs is the one with higher accumulated experience, since several prototype and commercial SFRs operated and operate worldwide. Six reactors are in operation, BOR60 and BN600 in Russia, Joyo and Monju in Japan, FBTR in India and CEFR in China; two reactors are presently being constructed, PFBR (500MWe) in India and BN800 (800MWe) in Russia, and several projects are currently developed: CFBR in India, BN1200 in Russia, JSFR in Japan, KALIMER in Korea, CDFR in China.

In France, which is one of the nine original members of the GIF, the first prototype of SFR (Rapsodie) achieved criticality in 1967. After this prototype, two commercial SFRs, Phenix and Superphenix, operated and were connected to the electric grid in 1973 and in 1986, respectively. In 2010, the French gouvernement committed to the “Commissariat à l’énergie atomique et aux énergies alternatives” (CEA) the mission of performing the initial design studies for a prototype of the fourth-generation sodium-cooled fast reactor, known as ASTRID (Advanced Sodium Technological Reactor for Industrial Demonstration). The main objectives of this reactor, which will have a power of 1500 MWth, are the achievement of safety level at least equivalent to 3rd generation reactors associated, including Fukushima accident feedbacks, a load factor of 80% and demonstration of minor actinides transmutation. Following preliminary schedule, the first criticality of ASTRID is expected in 2023.

1.2 Sodium Fast Reactors and Supercritical CO₂ Brayton cycles

Sodium pool type reactor concept is shown in figure 1.1. The primary vessel, containing the core, is circulated by liquid sodium, which behaves as coolant. Intermediate heat exchangers (IHX) are also placed in the primary vessel, allowing the primary sodium to exchange thermal power with the secondary loop, also circulated by liquid sodium. The aim of the secondary loop is to avoid any radioactive material outlet from the primary vessel: through neutron capture, Na-23 turns into Na-24, which is gamma emitting with 15 hours half-time. The secondary loop transfers thermal power from the primary loop to the third one, which is the energy conversion cycle. Sodium circulating the first loop is practically at atmospheric pressure, being pressurized at not more than 3 bar. Its core inlet and outlet temperatures are 395°C and 545°C, respectively. The secondary loop is slightly more pressurized than the primary one, in order to avoid primary sodium transfer to the secondary loop in case of leakage.

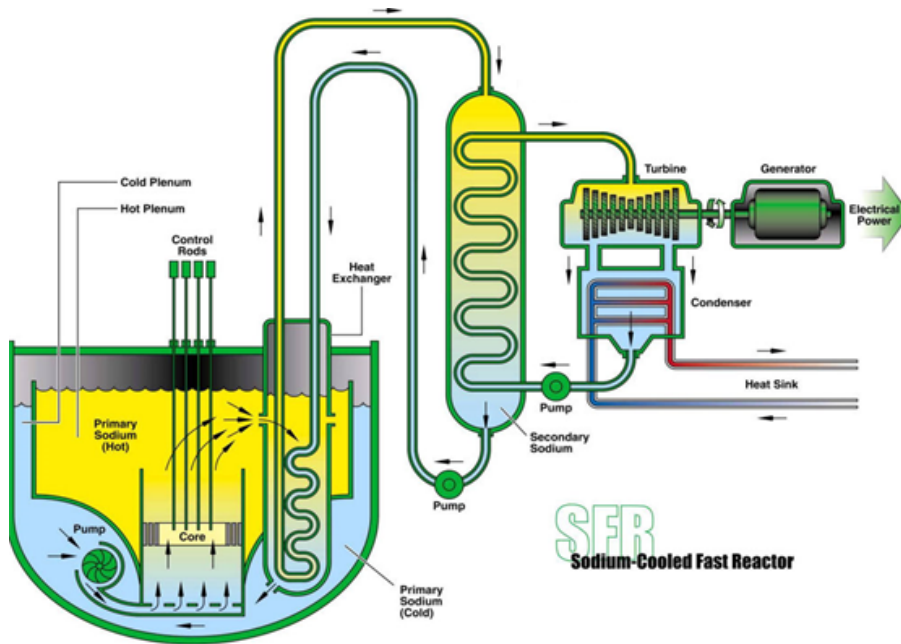
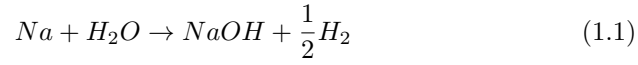


Figure 1.1: Sodium pool type reactor scheme.

Concerning the energy conversion cycle, conventional water Rankine cycle was employed for the French Phenix and Superphenix power plants, and for all the others commercial SFRs worldwide. In this configuration, one or more steam generators couple the secondary sodium loop with the Rankine cycle, as shown in figure 1.1. Standard steam generator design employs water in the tube side (which can be straight or helicoidal) and sodium in the shell side. Sodium-water reaction (SWR) in case of leakage inside the steam generator is an important security issue in SFRs: sodium and water react exothermically producing soda and hydrogen, through the following reaction path:



The enthalpy of this reaction is $141 \text{ kJ} \cdot (\text{mol}_{Na})^{-1}$ ($188 \text{ kJ} \cdot (\text{mol}_{Na})^{-1}$ if the heat of dissolution of NaOH in water is considered). Following an accidental tube leakage inside the steam generator, this reaction has been proven to cause corrosion and erosion phenomena. If a hole is developed on one tube wall, high pressurized steam (or water) is ejected into shell-side liquid sodium, creating a jet impinging on the adjacent tube. The mechanism of this scenario is shown in figure 1.2.

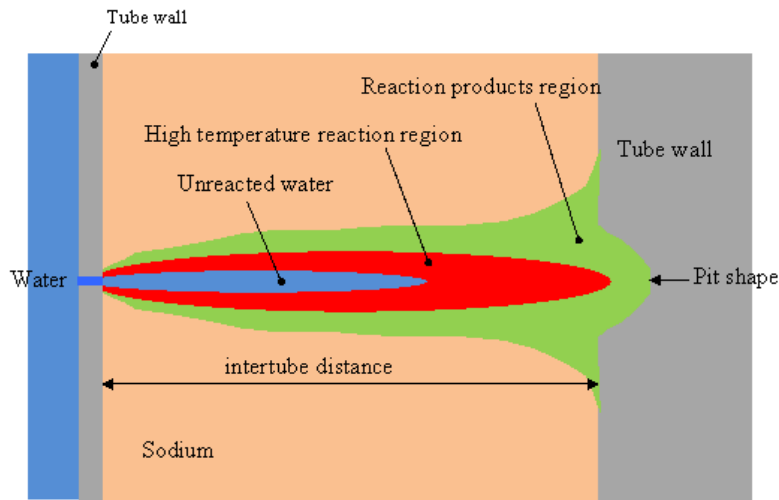


Figure 1.2: Schematic representation of SWR following a tube leakage in the steam generator of an SFR.

Steam, which is at about 18 MPa, leaks from the hole, accelerating and expanding reaching sonic conditions inside the orifice throat, since the pressure ratio between the water and the sodium side is largely higher than the critical value. If the pressure at sonic conditions is still higher than the sodium side pressure, as it is for the specific case considered, the steam flow will expand at the outlet of the orifice down to the sodium pressure: this further expansion is referred to as underexpansion, and the resulting gas jet is called underexpanded jet. As a consequence of the underexpansion, steam velocity increases from the sonic condition (Mach=1) inside the orifice, to supersonic conditions (Mach>1) in the first region downstream the orifice. The presence of NaOH as reaction product causes corrosion on the adjacent tube wall, and the high velocity jet causes erosion by removing the corrosion products from the tube surface, eventually leading to complete perforation of it: this new leak can cause further perforations in adjacent tube walls, in a sort of chain-reaction phenomenon, leading to an exponential increase of the global leaking flow rate with time.

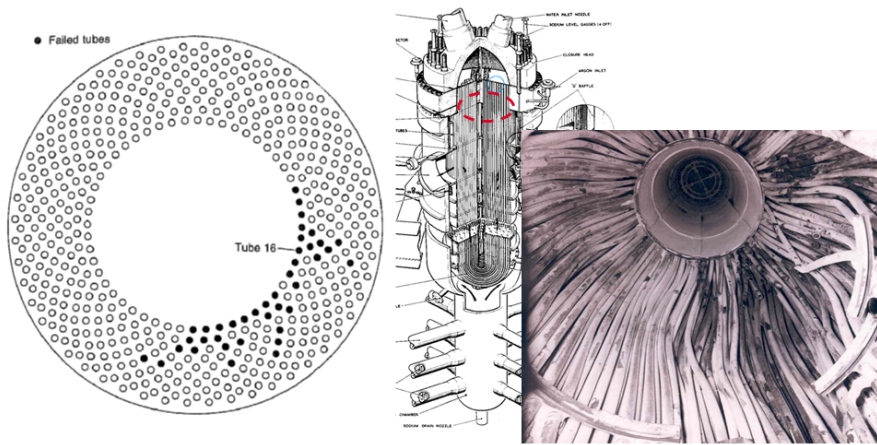


Figure 1.3: Damages caused by water leakage and consequent wastage in Dounreay's Prototype Fast Reactor [6].

This accidental scenario, referred to as wastage, has occurred in operating SFRs [6] (as shown in figure 1.3) and has been widely experimentally studied [7, 8, 9, 10]. Beside the wastage problem, SWR also produces gaseous hydrogen, whose presence must be adequately handled.

In order to avoid the accidental SWR scenario, Brayton cycles have been recently investigated as alternative concept for the energy conversion cycle [11, 12, 13, 14, 8]. Supercritical carbon dioxide and nitrogen are the two main candidate gases for such cycles. Compared to the N_2 option, supercritical CO_2 (sCO_2) cycles feature higher thermodynamic efficiency, taking advantage of CO_2 compression near its critical point, where gas density significantly increases (see figure 1.4): typical efficiency of supercritical CO_2 cycles is higher than 42%, whereas N_2 Brayton cycles cannot reach more than 38.5% [11]. The high fluid density of supercritical CO_2 remarkably reduces the size of turbine and compressors, resulting in significant reductions in the size and capital cost of the turbomachinery. In the configuration of an SFR coupled with a Brayton cycle, the steam generator is replaced by a heat exchanger, whose final design has not been defined yet: beside typical shell&tube configurations, the Printed Circuit Heat Exchanger (PCHE) types are being investigated.

Focusing on a sCO_2 Brayton cycle, the recompression cycle, shown in figure 1.5, is a closed Brayton type cycle and is highly recuperated, with the recuperated heat flux typically greater (150%) than that of the main heat source. The cycle operates at supercritical conditions throughout and features a flow split that allows a portion of the CO_2 to be recompressed by a second bypass compressor without first rejecting heat. The flow split decreases the mass-flow rate through the cold-side of the Low Temperature Recuperator (LTR) to counter the imbalance in the specific heat capacity (resulting from the strongly non-ideal nature of CO_2 close to the critical point, see figure 1.4) and so increase the temperature of the fluid leaving the High Temperature Recuperator (HTR). The corresponding increase in temperature at the inlet of the IHX means heat is added to the cycle at a higher temperature and the cycle efficiency is thus increased. One further important feature of the cycle is that it is high pres-

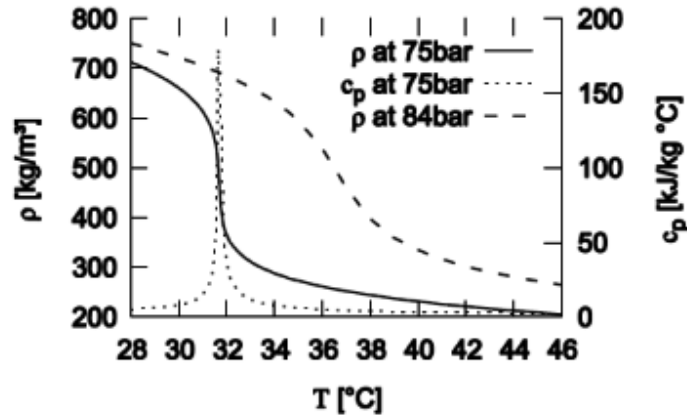


Figure 1.4: The CO_2 specific heat capacity and density close to the fluid critical point (31°C, 74 bar). The fluid properties are determined as per Span and Wagner (1996).

sure, with maximum pressures typically in excess of 20 MPa when the cycle is optimized for an SFR.

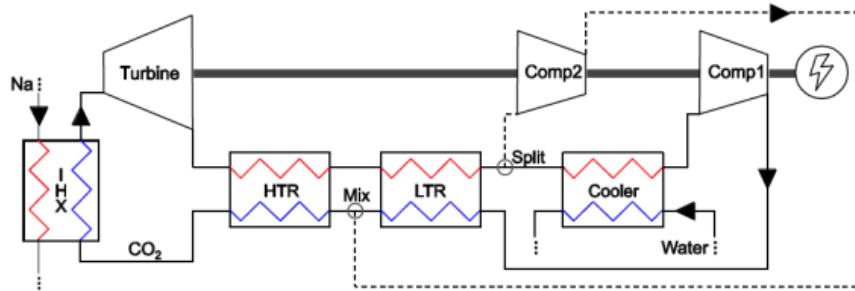


Figure 1.5: The sCO_2 recompression cycle arrangement [12]. HTR and LTR refer to High and Low Temperature Recuperators and the IHX is the Intermediate Heat eXchanger.

The sCO_2 Brayton cycle design and optimization has been performed by Floyd et al. [12] for the French SFR project ASTRID. For ASTRID inlet/outlet core temperature range and assuming two 750 MWth loops, the sCO_2 recompression cycle is appropriate as it is relatively simple but still yields high efficiency: 42–43% (see figure 1.6) at a Turbine Inlet Temperature (TIT) of 515°C. The final optimized full cycle for a T_{in} (inlet temperature in the main compressor) of 35°C is shown on figure 1.8, which shows the whole ASTRID-three-loop balance of plant, and achieves a net plant efficiency of 42.2%. The balance between turbine and compressors work provides 330.25 MW, which are first decreased to 325.96 MW once taken into account generator mechanical efficiency (98.7%), then to 319.44 MW once taken into account auxiliary plant system consumption

(2%), and finally to 316.4 MW once taken into account the sum of the sodium pumps power. The ratio between these available 316.4 MW over the 750 MW core power input, achieves the above mentioned 42.2% net plant efficiency.

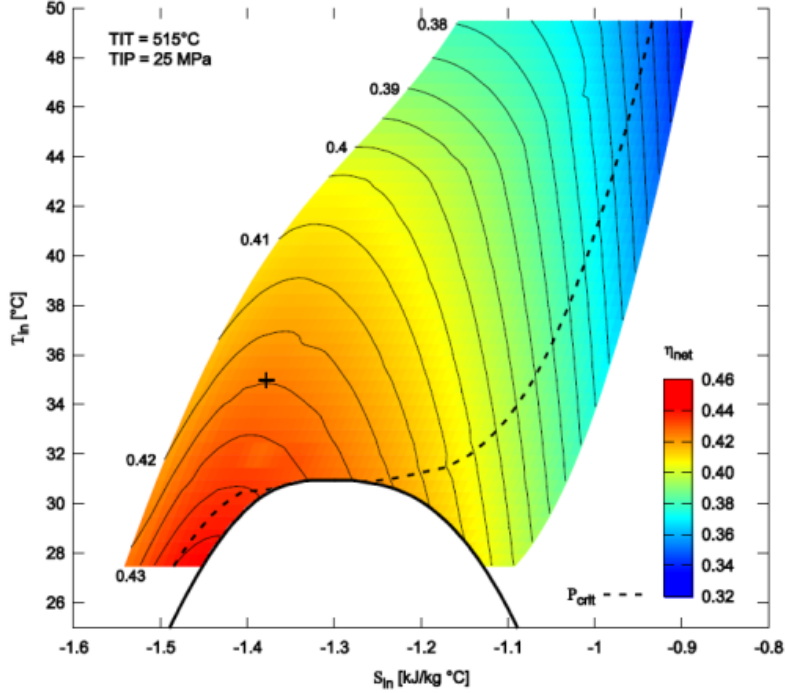


Figure 1.6: An optimized, on-design efficiency map for the recompression cycle generated as per Floyd et al., using constant polytropic turbomachines efficiencies. The compressor inlet temperature T_{in} is total. The efficiency η is net of the sodium pumps electric power, generator mechanic efficiency (98.7%), and auxiliary plant systems (2% of alternator power) [12].

1.3 Scope of the work

This PhD thesis has been realized at the CEA of Cadarache, with the Ecole Nationale supérieure de Mines de Saint Etienne (EMSE). Several studies have been realized at CEA, in the frame of $s\text{CO}_2$ Brayton cycles coupled with SFRs. These studies concern both the $s\text{CO}_2$ cycle balance of plant (optimal pressures and temperatures, turbomachines and heat exchangers design) [12, 11, 13] and the Na- CO_2 interactions, in case of an accidental contact between them during the operation of the nuclear power plant. In fact, despite its potential advantages from the thermo-dynamic and economical point of view and, of course, the elimination of the SWR accidental scenario, the drawback of $s\text{CO}_2$ for SFRs is the fact that CO_2 reacts exothermically with sodium, forming solid reaction products such as sodium carbonate and carbon. For this reason, a first PhD thesis was realized at CEA by Gicquel [15], who performed different experimental tests in order to investigate the occurrence of the sodium- CO_2 reaction

(SCR) and the reaction products. The exothermic reaction has been proven to occur in the range of temperature between 300 and 700°C. The analysis of reaction products showed the presence of the carbon, oxygen and sodium elements, which is consistent with previous literature studies that list CO, Na₂CO₃ and Na₂C₂O₄ as reaction products [16]. The specific reaction pathways found are different, depending on reactants temperature, as it will be detailed in paragraph 2.2. The present work is aimed at improving the comprehension of the actual interaction mechanism and consequences of a SCR inside a Na-CO₂ heat exchanger of a SFR, following the previous results obtained by Gicquel.

Considering the operative pressures, a leakage in the CO₂-Na heat exchanger would result in a phenomenon analogous to the one already described for the steam generator SWR accidental scenario: an underexpanded reactive CO₂-into-liquid-sodium jet. One main difference, from the safety point of view, between the SWR and the SCR, is the proven absence of wastage phenomena in case of SCR [8]. In fact, no corrosive products are created by the SCR. Eoh et al. investigated steam-into-sodium and CO₂-into-sodium jet impingement consequences, using an experimental facility allowing to inject highly pressurized gas into liquid sodium. Figure 1.7 shows the different consequences of SWR and SCR on a 9Cr-1Mo steel target placed at a distance of 12.0 mm from a 0.3 mm diameter nozzle. Injection pressure was 5.5 MPa for the CO₂ case and 15.0 MPa for the steam case. Liquid sodium initial temperature was 400°C and 450°C. Injection time was 120 seconds for the SCR case and 30 seconds for the SWR case.

Eoh et al. observed that, concerning the CO₂ injection case, since a large amount of reaction heat was allocated to the impinging area, the target surface experienced a kind of thermal damage. Hence, the region directly impinged by the CO₂ jet became dark as the initial sodium temperature increased, as shown in the figure 1.7 A and B. In spite of the apparent damage, little mechanical degradation was observed on the target surface. The damaged depth was far less than 10 μ m, which was not much different from the manufacturing roughness of the tube material. Although the kinetics of the sodium-CO₂ interaction is strongly affected by the reaction temperature, a combined corrosion/erosion effect was not observed, even in high-temperature tests. In order to compare this feature with the SWR case, high-pressure steam injection tests were carried out in the same manner as the CO₂ injection test. Figures 1.7 C and D show the results of the steam wastage effect tests. The post-test view of the target assembly of the SWR case is significantly different from the result of the SCR: the target surface was apparently damaged to a depth of 1.4 - 2.4 mm depending on the test conditions. Hence, the surface degradation rate of the SWR case was determined to be approximately 4 mm/min on average, while that of the SCR was less than 0.005 mm/min. This is mainly because a highly corrosive by-product was produced during the SWR period, and a combined corrosion/erosion effect took place vigorously on the target surface. This is very different from the SCR, which has no sodium hydroxide formation. This comparison confirms that the potential surface degradation resulting from CO₂ impingement could be negligible for normal sodium operating temperatures, and thus the wastage scenario, including additional damage propagation, does not need to be considered for the conditions of the identical target distance and nozzle diameter used in the SWR wastage tests.

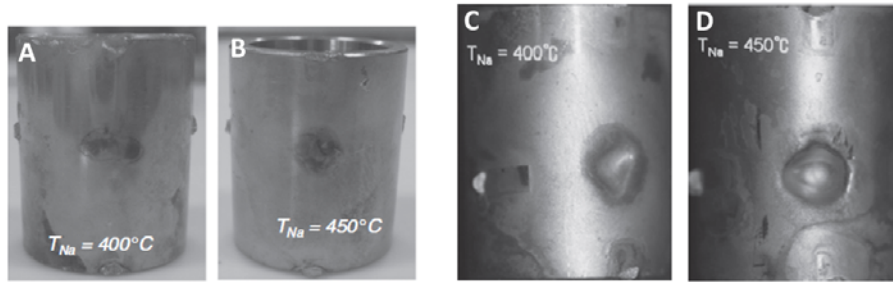


Figure 1.7: Post-examination of target tubes after CO_2 (A and B) and steam (C and D) injection [8].

In order to fully comprehend the feasibility of future applicability of sCO_2 cycles for SFRs, CO_2 -Na interactions, occurring in a leakage accidental scenario, must be further investigated. Even if no wastage phenomena are caused by the SCR, kinetics of the reaction must be known in order to foresee the increase of temperatures caused by the reaction, as well as the space and time distribution of the solid reaction products inside the CO_2 -sodium heat exchanger.

The comprehension of the actual physical phenomena taking place inside the reactive two-phase flow caused by the leakage event is still an open issue. Moreover, even if the SCR paths have already been investigated and are now quite well known, much less knowledge exists concerning the kinetics of this reaction. When one considers the kinetics of a heterogeneous reaction, a crucial parameter is the contact typology between the liquid and gaseous reactants. Without a comprehension of the two-phase mixing phenomena occurring inside the jet, describing the heterogeneous reaction and determining its kinetics parameters would result to be a difficult task.

The present work is aimed at studying reactive underexpanded gas-into-liquid jets, with the purpose of gaining knowledge about hydrodynamic and chemical phenomena taking place in such a two-phase flow. The final goals of this work can be summarized through the following points:

- the preliminary understanding of the two-phase behavior of non-reactive and reactive gas-into-liquid jets;
- the numerical modeling of the CO_2 -into-Na jet, with the aim of determining the chemical reaction kinetic rate of the Na- CO_2 chemical reaction occurring inside it;
- the future utilization of the developed numerical model for the prediction of the consequences of a leakage event inside the Na- CO_2 heat exchanger, in terms of temperature distribution on the tube surfaces and inside the heat exchanger, and mass fraction distribution of reaction products inside the heat exchanger.

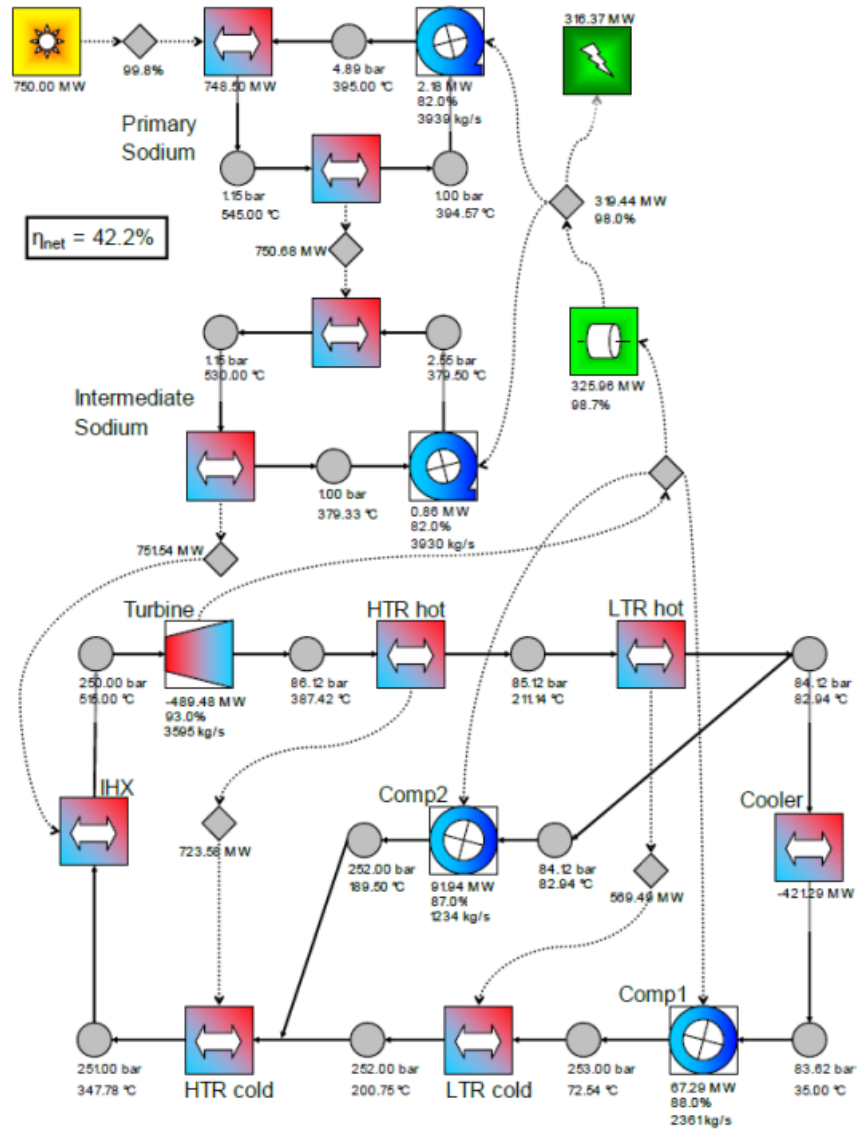


Figure 1.8: The optimized sCO₂ cycle based on the ASTRID specifications including sodium loops [12]. All values are total, dotted lines represent energetic transfer.

1.4 Thesis outline

After the introduction to the context and scope of the present work, the second part of the thesis, chapter 2, will focus on a bibliography study on two different subjects: the first concerns the research available on underexpanded gas-into-liquid jets, the second the current knowledge on sodium-CO₂ interactions.

In the third part, chapter 3, the two experimental facilities employed in the

present work will be described. Both facilities have been built at the CEA: one is dedicated to the investigation of underexpanded gas-into-water jets and the other to the study of CO₂-into-sodium jets.

The fourth part of this work, chapter 4, will be dedicated to the development of a numerical model for the representation of non-reactive underexpanded gas-into-liquid jets. The two-phase modeling approach adopted will be described in detail; the results will be presented and compared with the experimental results obtained with the facility built at CEA (described in chapter 3).

The fifth chapter of the thesis deals with the development of a Na-CO₂ reaction model. The modeling approach considers the sodium-CO₂ contact typology occurring in the specific two-phase flow investigated.

In the last part of this work, chapter 6, the modeling approaches developed in chapter 4 and 5 will be coupled, in order to build a numerical model for the description of an underexpanded reactive CO₂-into-liquid-sodium jet. The results obtained will be presented and compared with the experimental data obtained during the tests performed with the experimental facility built at CEA (described in chapter 3). This last step will allow to identify the characteristic kinetics parameters of the considered Na-CO₂ chemical reaction.

Chapter 2

Bibliographic study

2.1 Bibliography on underexpanded gas-into-liquid jets

Underexpanded gas-into-liquid jets is a subject that has not been widely investigated in literature. Some available studies are found in the context of underwater propulsion, where high pressurized gas is injected into water at sonic or supersonic velocities, in order to generate thrust [17]. Recently, interest towards this kind of two-phase flow has been raised in the frame of SFRs steam generator accidental scenarios. Most of modeling studies available in literature focus on water vapor into liquid sodium jets. Even if several attempts of numerically describing this kind of two-phase flow have been realized, the correct representation of all the physical aspects regarding underexpanded gas-into-liquid jets is a challenging task: therefore, most of existing works are based on assumptions ignoring some complex and important physical aspects, with the aim of decreasing the numerical complexity of modeling. Besides modeling work, even less data exist concerning experimental studies on such flows. Once again, some interesting work has been recently realized in the context of the SWR in SFRs. In the following, an overview of the useful available experimental and modeling studies on underexpanded gas-into-liquid jets will be given.

2.1.1 Experimental studies

2.1.1.1 Gas-into-liquid versus gas-into-gas underexpanded jets

Interesting experimental results on underexpanded gas-into-liquid jets were obtained by Loth and Faeth [18, 19], who studied the structure and mixing properties of round turbulent air jets submerged in still water, considering subsonic and sonic jet exit conditions with underexpansion ratios (defined as the injection to ambient gas pressure ratio) as high as 8:1. Pressure transducers with static pressure tap, gamma-ray absorption and laser Doppler anemometer were employed for static pressure, void-fraction and velocity measurements, respectively. Results, reported in figure 2.1, showed how the static pressure variations along the axis for injection of air into water are similar to those observed for injection of air into air, at least for the first few shock cells.

Notably, Surin et al. [20] observed similar agreement of oscillatory dynamic pressure variations along the axis of underexpanded gas jets in gases and liq-

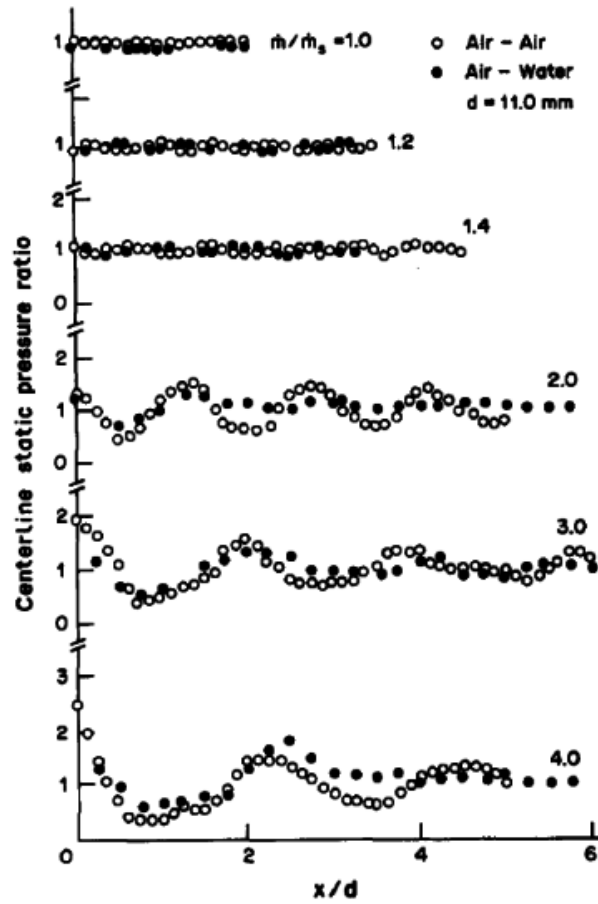


Figure 2.1: Mean static pressure along the axis for various mass flow ratios, obtained by Loth and Faeth (\dot{m}_s is the mass flow rate for an exactly adapted jet, meaning that gas pressure at choke conditions is equal to the downstream ambient pressure) [18].

uids.

This provides strong evidence that a shock wave containing external expansion region is present for underexpanded gas jets in liquids. The main difference, between the static pressure records for underexpanded air jets in air and in water, is that the external-expansion region decays more rapidly for injection into water. This behavior is expected since turbulent mixing is more rapid when a low-density material is injected into a high-density environment.

To investigate the possible gas dynamic region within the two-phase jet, shadowgraphs were taken by Loth and Faeth, for both air injected into air and air injected into water. Figure 2.2A shows the typical underexpanded shock cells for air injected into an ambient air environment for an underexpansion ratio of 3.0. Figure 2.2B shows the analogous photograph for air injected into water at the same underexpansion ratio. Liquid along the glass walls obscures much

of the flow field, however, the similarly shaped first shock cell, as well as some of the compression waves and expansion fans seen in the air-air case, can still be observed. Thus, these shadowgraphs provide evidence of the compressible wave pattern within the air core for an underexpanded plane air jet injected into water.

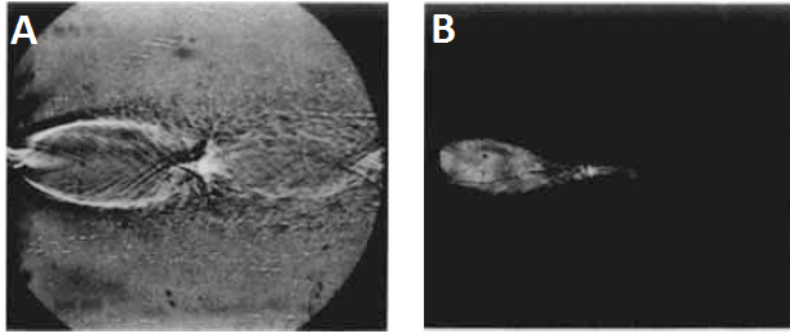


Figure 2.2: Shadowgraph results obtained by Loth and Faeth: air-into-air for $\dot{m}/\dot{m}_s = 3.0$ (A) and air-into-water for $\dot{m}/\dot{m}_s = 3.0$ (B) [19].

2.1.1.2 Entrained droplet size

Epstein et al. [21] performed experimental investigations on underexpanded gas-into-liquid jets, in the frame of the development of an analytical model to predict the peak temperature in a sodium-water reaction jet. Specifically, an experimental investigation was performed to determine the effective droplet size (Sauter mean diameter: SMD) of liquid entrainment in the near field of a submerged jet. The apparatus was designed to allow controlled steady-state vertical injection of N_2 gas through an orifice located just below the surface of a water pool. The water pool was contained within a rectangular plastic tray. The dimensions of the water pool were 21.5 cm wide, 60.8 cm long and approximately 15 cm deep. N_2 was injected at stagnation pressures up to 1.2 MPa. The upward directed spray produced by the slightly submerged (up to 2 mm) sonic jet was sampled with a Malvern spray droplet sizer, which measured the droplet size distributions of sprays through diffractive scattering. One size distribution measurement is made every 400 ms. Each size distribution recorded by the Malvern instrument is an average of 1,000 to 2,000 measurements. All the measurements made in the study were averages of approximately 30 to 60 recorded size distributions reported at 1 to 2 s intervals. Epstein built a correlation, following the results of SMD obtained as a function of the main parameters such as nozzle diameter, injection pressure and nozzle submergence depth. Typical values of SMD as a function of these parameters are shown in figure 2.3, 2.4 and 2.5.

Two different sampling locations (denoted by the symbol z_{beam}) were investigated in these tests: 19 and 48 orifice diameters. The results are essentially independent of the sampling location, as shown in figure 2.3. A decrease in SMD with decreasing orifice depth is indicated by the data at 0.31 and 0.52 MPa, the opposite is true at 0.2 MPa and essentially no effect of orifice depth

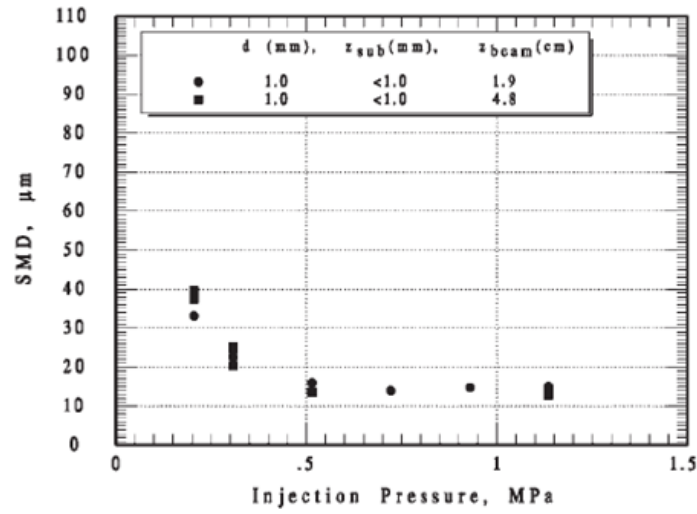


Figure 2.3: Sauter mean diameter vs. injection pressure obtained by Epstein; effect of orifice-to-laser distance (z_{beam}) [21].

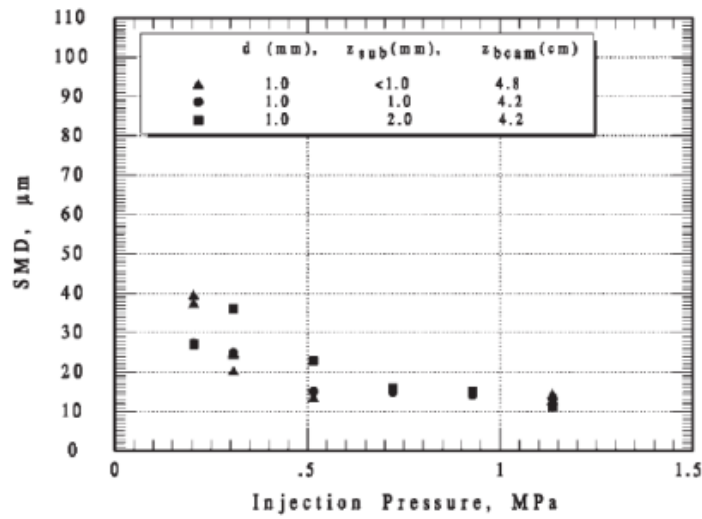


Figure 2.4: Sauter mean diameter vs. injection pressure obtained by Epstein; effect of orifice submergence depth (z_{sub}) [21].

is revealed at the other pressures investigated, as shown in figure 2.4. This insensitivity implies that the drop number density at the liquid surface was too small to result in significant drop coalescence between the liquid surface and the sampling location. The data obtained with the 1.0- and 2.0-mm diameter nozzles reveal small to modest changes in droplet size with changing sampling location and water depth, as shown in figure 2.5. As shown in fig-

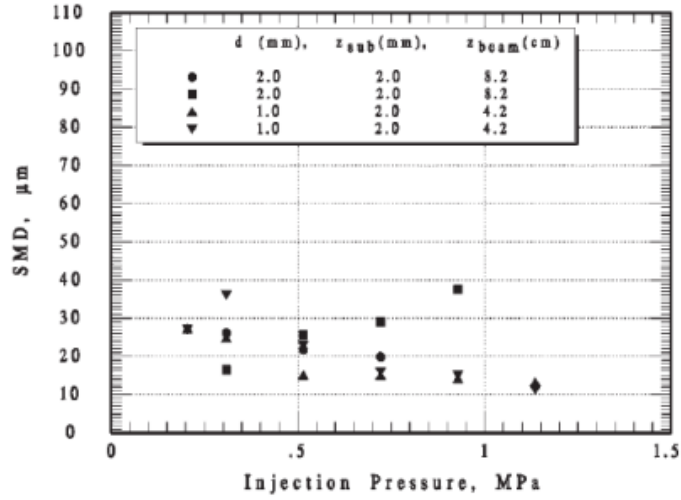


Figure 2.5: Sauter mean diameter vs. injection pressure obtained by Epstein; effect of nozzle diameter [21].

Figure 2.6, Epstein found that the following relationship properly correlates the results obtained:

$$\frac{SMD}{d_0} = 0.39 \left[\frac{\sigma}{u_0^2 \rho_g d_0} \right]^{0.4} \quad (2.1)$$

Where d_0 , σ , u_0 and ρ_g are the nozzle diameter, the surface tension, the velocity of gas jet at end of expansion zone and the density of the depressurized gas jet, respectively.

Kudoh et al. [22] investigated size distributions and mean diameters of liquid sodium droplets entrained into gas jets, stating that the understanding of the mechanisms of the entrainment of sodium and the generation of sodium droplets, in addition to the prediction of the droplet size distributions, are a prerequisite in order to accurately model and predict the peak temperature in SWR. A test section of stainless steel vessel with an inner diameter of 80 mm and a height of 700 mm was used. A glass tube of 19 mm in outer diameter, which simulates an adjacent heat transfer tube inside a steam generator of a SFR, was inserted horizontally into the test section at a height of 180 mm from the bottom. The diameter of the nozzle-hole was 3.5 mm, and the axial distance between the nozzle exit and the glass tube was 25 mm. The test section was filled with static liquid sodium, and the liquid level was adjusted to 550 mm from the bottom. High-purity argon gas was injected upward from the nozzle. An endoscope was inserted inside the glass tube. Images of the gas jet behavior were captured by a high-speed camera at a frame rate of 2000 fps connected to the endoscope. Three conductivity probes for void fraction measurement were placed around the glass tube. The liquid sodium and argon gas temperatures were both maintained at 120°C. The gas jet velocities at the nozzle exit were

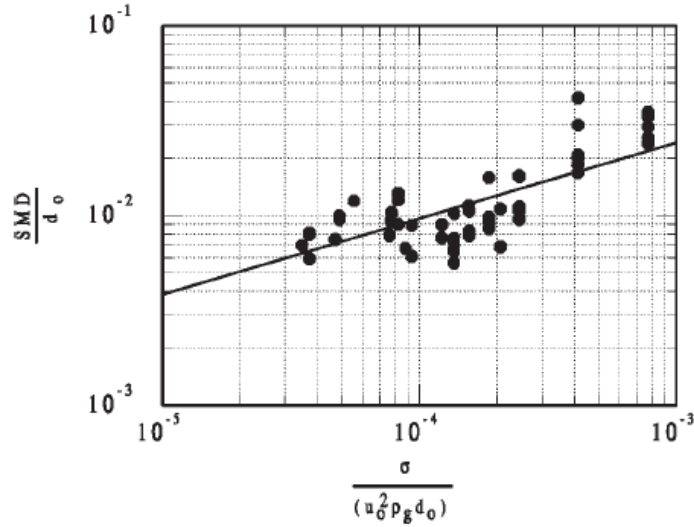


Figure 2.6: Correlation of drop size data found by Epstein [21]. Dark line is least squares fit given by equation 2.1.

chosen to be from 13 to 125 m/s. The pressure difference between the sodium pressure (atmospheric pressure) and the stagnation pressure of the gas jet at injection velocity of 125 m/s was calculated from the isentropic assumption as 20 kPa. As one can notice, these conditions do not represent an underexpanded gas-into-liquid jet, since injection-to-ambient pressure ratio is lower than the critical value. Nevertheless, gas injection velocity is high and considered by Kudoh et al. representative of the actual underexpanded gas-into-sodium jet.

When the gas jet injection velocity exceeds 50 m/s, a number of liquid droplets impinging on the glass tube surface were observed. Kudoh et al. distinguished two different droplet formation mechanisms. A clear formation of liquid droplets was observed when the gas jet diameter decreases towards the center of the nozzle: this sort of instability can be observed because the nozzle exit, during a certain time, is hidden by liquid sodium (meaning that the nozzle exit is covered by liquid sodium), in the experimental observation. Kudoh et al. refer this mechanism as the near region generation, and typical images of this process are shown in figure 2.7. Typical images of another formation process of droplets were obtained at the far region from the nozzle, that refers to the moment where the gas-liquid interface was more distant from the nozzle, as shown in Figure 2.8. Liquid sodium ligaments appeared in the gas jet region (0 ms) and were then broken up into numerous droplets at the tube surface (0.5 ms). The transient time (in ms) reported by Kudoh et al. does not correspond to the beginning of the gas injection and/or of the recording of images: it is employed just as a time scale of the high speed recordings and of the physical phenomena. Kudoh et al. note that over 95% of the droplet formation observed in the present study occurred at the near region of the nozzle exit.

Following the obtained results, Kudoh qualitatively explain the mechanism for the droplet generation that occurred intermittently in a short-time period

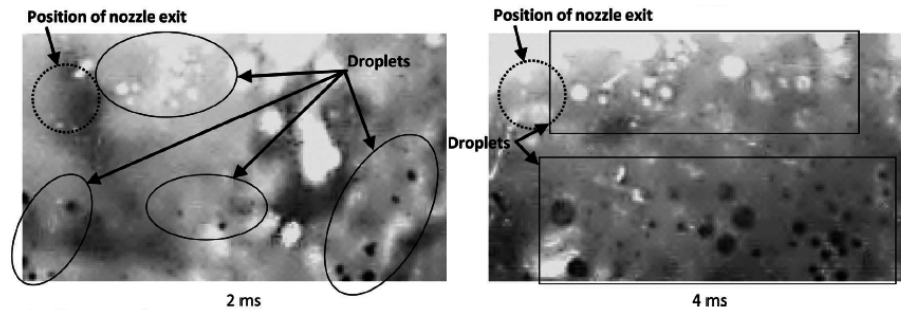


Figure 2.7: Image obtained by Kudoh et al.: droplet generation in the near region from the nozzle (gas injection velocity: 75 m/s)[22].

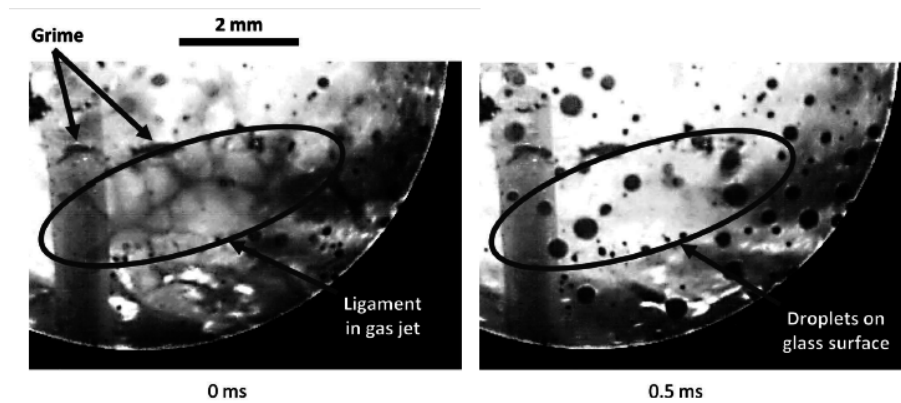


Figure 2.8: Image obtained by Kudoh et al.: droplet generation in the far region from the nozzle (gas injection velocity: 75 m/s) [22].

in the vicinity of the nozzle, as shown in figure 2.9a. Considering that the velocity distribution of the gas jet in the injecting direction depends on the cross-sectional area of the gas jet, the relative velocity between the gas jet and the ambient liquid sodium reaches a maximum value when the jet diameter in the vicinity of the nozzle is approximately equal to the nozzle diameter. Therefore, sodium droplets are considered to have been produced by liquid sodium shearing off from the unstable gas–liquid interface that formed just above the nozzle exit due to the momentum exchange between the gas jet and the ambient liquid. Figure 2.9b explains the mechanism of droplet formation at the far region from the nozzle. The gas–liquid interface at the submerged gas jet causes numerous surface waves and highly rolled-up waves are generated with increasing gas jet velocity. The crests of the rolled-up waves are then entrained into the gas jet and form liquid ligaments. Liquid droplets are then produced by the disintegration of the liquid ligaments.

Optical images with liquid droplets were selected for obtaining the droplet size distributions, and the diameters of approximately 800–1000 droplets were measured by counting the number of pixels corresponding to the droplet diameter. Figure 2.10 shows the droplet size distributions, $\Delta n/N$, obtained in each ex-

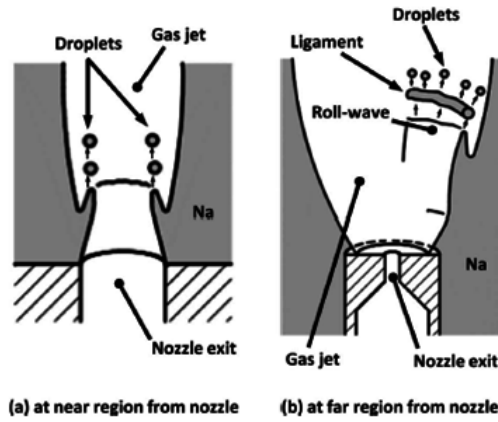


Figure 2.9: Illustration of droplet generation in the near and far region, given by Kudoh et al. [22].

periment for various gas jet velocities. Here, N is the total number of liquid droplets measured and Δn is the number of liquid droplets included in every $56.7\text{-}\mu\text{m}$ increment. The figure shows that the number of smaller droplets increases with increasing gas jet velocity.

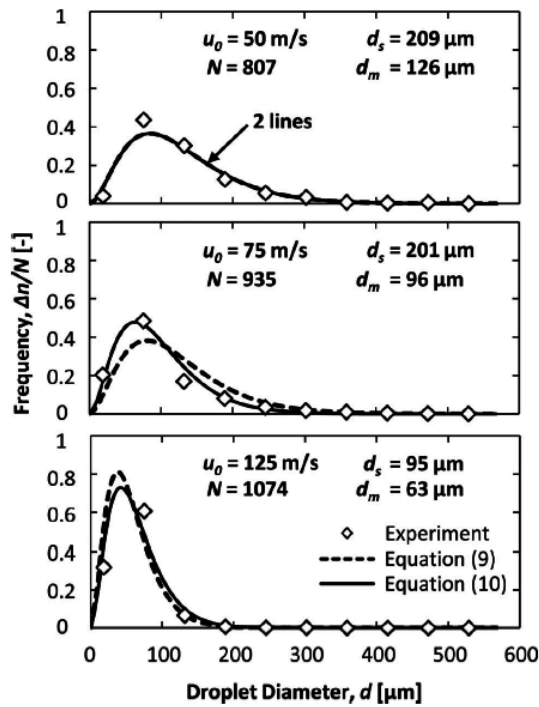


Figure 2.10: Droplet size distribution obtained by Kudoh et al. [22].

Figure 2.11 shows the measured mean droplet diameters in the coordinate

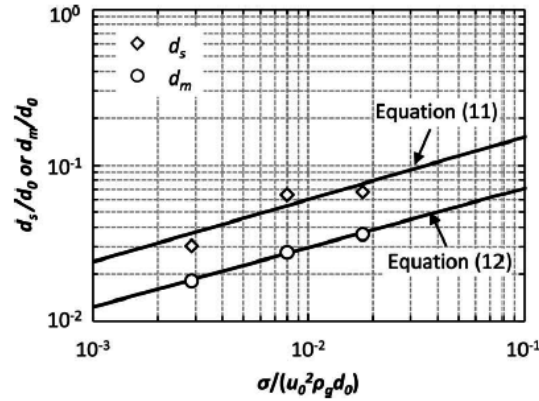


Figure 2.11: Correlation of mean droplet diameter found by Kudoh et al. [22]. In the original reference [21], Equation (11) refers to Epstein's correlation, d_s to Sauter mean diameter and d_m to arithmetic mean diameter. Equation (12) refers to the empirical equation, found by Kudoh et al., which correlated the results for d_m .

system suggested by Epstein's correlation (equation 2.1). The plotted values were obtained using the physical properties for liquid sodium and argon gas at 120°C. As shown in the figure, good agreement between equation 2.1 and Kudoh's data on Sauter mean diameter is obtained. This indicates that Epstein's correlation, which was obtained from a water experiment, is applicable to liquid sodium atomization, which has a higher surface tension than water.

2.1.1.3 Temperature profiles

In the frame of the SWR, interesting experimental results were obtained by Sekkouti [23], who investigated the temperature distribution inside reactive steam-into-sodium jets. The measurements were performed through a comb of thermocouples placed in different radial and axial positions inside the jets. The underexpanded jets were realized employing pressurized water steam injected into a liquid sodium pool, through sonic nozzles with diameters ranging from 0.7 to 1.0 mm. Figure 2.12 shows the temperature profile measured along the jet axis, for different steam injection pressures, a 1.0 mm-diameter nozzle, an initial sodium temperature of 350°C. Water steam temperature was not specified.

Gicquel [15] performed similar experimental tests as Sekkouti, but using CO₂ as gas, in the frame of employing supercritical CO₂ Brayton cycles for SFRs. Using a comb of twenty thermocouples, axial and radial temperature profiles were determined inside a CO₂-into-liquid-sodium jet, realized injecting pressurized CO₂ inside a liquid sodium pool, through a sonic nozzle of 0.7 mm of diameter. The experimental facility used by Gicquel will be described in detail in paragraph 3.1. Typical temperature profiles obtained by Gicquel are reported in figure 2.13, corresponding to a jet of CO₂ at stagnation pressure of 1.0 MPa and different temperatures (as detailed in figure), injected into sodium

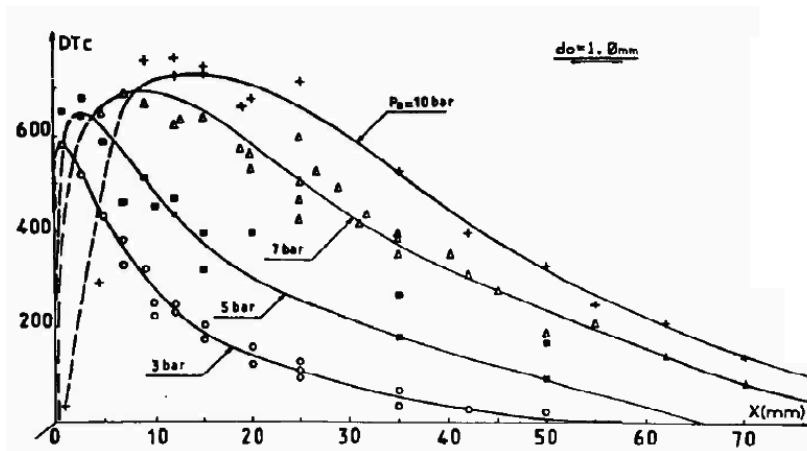


Figure 2.12: Temperature distribution, found by Sekkouti, along a steam-into-sodium jet axis, as a function of steam injection pressure (pressures value are to be intended as stagnation pressures of gas upstream the sonic nozzle) [23]. DT_c represents the difference between the measured temperature and the sodium temperature in the pool far away from the jet.

at atmospheric pressure and at an initial different temperatures (as detailed in figure), using a nozzle of 0.7 mm diameter.

Even if the gases used by the two authors are different, some qualitative conclusion can be derive by comparing Sekkouti and Gicquel experimental results. First of all, it can be seen that the maximum temperature inside the jet is likely to occur on the jet axis, with a sort of Gaussian distribution along the radial profile [15]. Secondly, the reaction seems to occur starting from a very short distance from the injection nozzle: for the same gas injection pressure, Sekkouti and Gicquel measured the maximum temperature at a distance corresponding to about 10-15 nozzle diameters and 4 nozzle diameters, respectively.

One important critical aspect must be taken into account when interpreting Sekkouti and Gicquel results. The thermocouples employed for the temperature measurements are placed at distances very close to the nozzle, where gas void fraction and gas velocity are very high: in these conditions, the difference between the gas static and stagnation temperature is significant (since the total temperature is conserved and equal to the injection total temperature, whereas the static value decreases due to the underexpansion) and, since thermocouples are supposed to always measure a stagnation temperature (due to the fact that the flow must slow down to zero velocity on the thermocouple surface), temperatures reported by the measurements close to the nozzle are likely to be the stagnation temperature inside the jet. Considering Sekkouti and Gicquel results, this would mean that the real static temperatures achieved inside the jet are lower than the ones actually reported by the authors. Since the enthalpy of the exothermic reaction is supposed to increase the jet temperature, attention must be payed in order to discern and separate the contribution of the exothermicity of the reaction and the contribution of the compressibility effect in the gas phase.

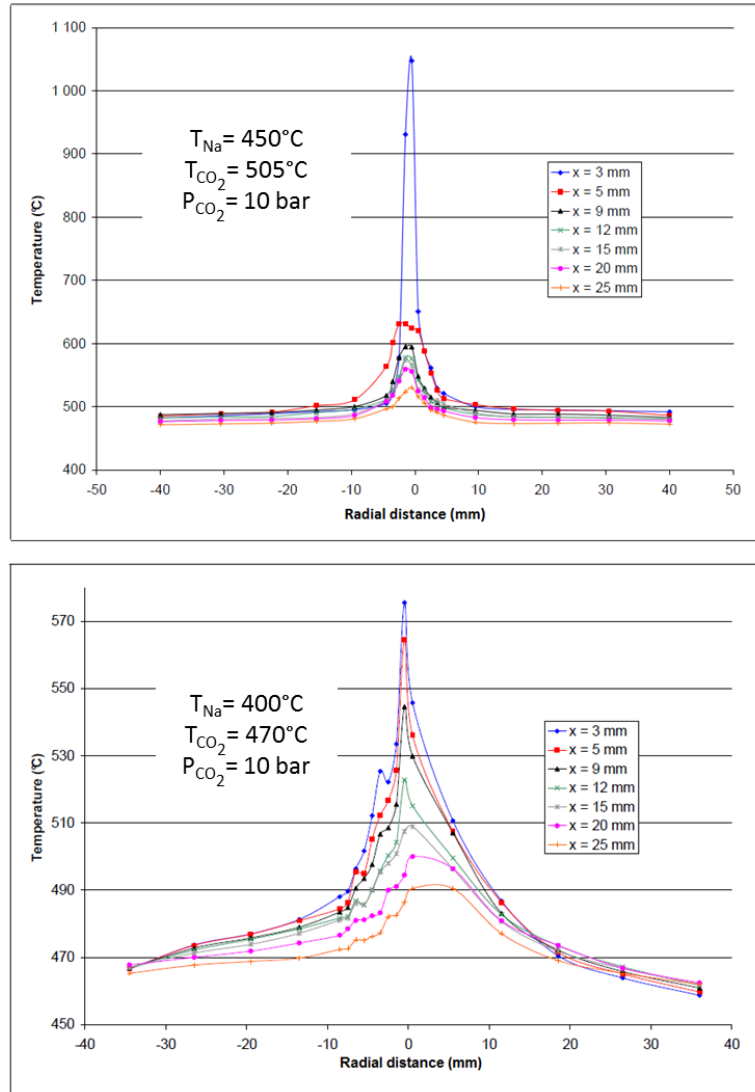


Figure 2.13: Radial temperature distribution inside a CO_2 -into-sodium jet, as a function of the axial distance (x) from the nozzle, for different initial sodium and CO_2 temperatures[15].

Close to the nozzle, the contribution due to the enthalpy of reaction can be over-estimated, since a non-negligible contribution, in this region, is given by the kinetic energy of gas converted into heat, as it can be easily understood considering the following isentropic equation of a perfect gas:

$$T_{tot} = T_{static} + \frac{v^2}{2c_p} = T_{static} \left(1 + \frac{\gamma - 1}{2} M^2 \right) \quad (2.2)$$

2.1.2 Modeling studies

This paragraph will be dedicated to the description of the most significant numerical models of two-phase jets, available in literature. Most of them are found in the context of SFRs.

The detailed description of the numerical modeling approaches for multi-phase flows will be given in chapter 4.

In the context of the SWR scenario in SFRs, Takata et al. [24, 25] developed a detailed numerical model of a SWR scenario for a single-tube and a multi-tube geometries. The model is based on an two-fluid Euler-Euler approach, meaning that continuity, Navier-Stokes and energy equations are solved for each phase, as it will be detailed in paragraph 4.1. Laminar Navier-Stokes equations were employed. As it will be detailed in chapter 4, the crucial issue, when employing a two-fluid approach, is the estimation of interfacial area, in order to determine momentum and energy exchange between phases. Takata employed the Nigmatulin model [26, 27] for the calculation of the interfacial area. This model was originally employed inside the Sodium Version of the Two-Phase Three Dimensional Thermal Hydraulics Code THERMIT [26], a thermalhydraulics code written at the Massachusetts Institute of Technology (MIT) for the purpose of analyzing transients under Liquid Metal Fast Breeder Reactor (LMFBR) conditions. The Nigmatulin model is purely based on bubbly flow regime, and the interfacial area (a , unit m^{-1}) value is obtained through the following correlations:

$$a = \begin{cases} \alpha^{\frac{2}{3}} \left(\frac{4\pi N}{3}\right)^{\frac{1}{3}} & \alpha \leq 0.5 \\ (1 - \alpha)^{\frac{2}{3}} \left(\frac{4\pi N}{3}\right)^{\frac{1}{3}} & \alpha > 0.5 \end{cases} \quad (2.3)$$

In 2.3, α is the void fraction and N is the bubble density [bubbles/ m^3]: in the Nigmatulin model, N is considered as a constant value, equal to 10^7 .

The phase friction coefficient is estimated through the Autruffe correlation [26, 28], which was derived from single tube sodium boiling data. Through the Nigmatulin model and the Autruffe correlation, the calculation of the interfacial momentum transfer can be realized.

Concerning the SWR chemical reaction, the authors made the assumption of infinite fast reaction, meaning that the chemical reaction at a liquid sodium surface is sufficiently higher than the mass diffusion rate of water vapor toward the surface. Under this assumption, the surface reaction rate is controlled by the mass flow rate of water vapor and is given by:

$$r_{H_2O} = Sh \frac{\rho_g D_{H_2O}}{l} (Y_{H_2O} - Y_{H_2O,l=0}) a \quad (2.4)$$

In 2.4, r_{H_2O} is the surface reaction rate (in $kg \cdot (m^3s)^{-1}$), Sh is the Sherwood number, ρ_g the gas density, D is the effective binary coefficient in the gas, Y_{H_2O} is the mass fraction of water vapor at bulk, $Y_{H_2O,l=0}$ is the water vapor mass fraction at the sodium surface, l is the characteristic length. Using the

definitions of Sherwood, Lewis and Nusselt numbers, Takata et al. rewrote equation 2.4 as follows:

$$r_{H_2O} = -Le^{b-1} a \frac{h}{c_{p,g}} Y_{H_2O} \quad (2.5)$$

Where h is the heat transfer coefficient between sodium and gas. b is the exponential coefficient of the Schmidt number in the expression of the Sherwood number: Takata et. al avoided to determine this coefficient by making the assumption of Lewis number equal to one.

Takata et al. tested their model for single-tube and 43-tubes cases. The simulation domain represents a shell of 400 mm square and 1800 mm height; tubes are placed perpendicularly to the upward direction (direction J in figure 2.14). The failed tube is located 300 mm high from the bottom of the shell. A square leakage of $3.3 \times 3.3 \text{ mm}^2$ is supposed. Water vapor blows upward through the leakage, with an injection pressure fixed to 17 MPa. Results are reported in terms of volume fraction, temperature, pressure and velocity. As an example, figure 2.14 shows the results obtained for the 3D 43-tubes case. The heat of reaction is allocated to the gas phase, leading to an increase of its temperature. The authors report that water vapor velocity obtained at the leakage outlet is around 90 m/s for all the investigated cases, and then gas velocity decreases downstream the nozzle. This value is significantly lower than real sonic conditions that should be obtained: this could be due to poor mesh refinement.

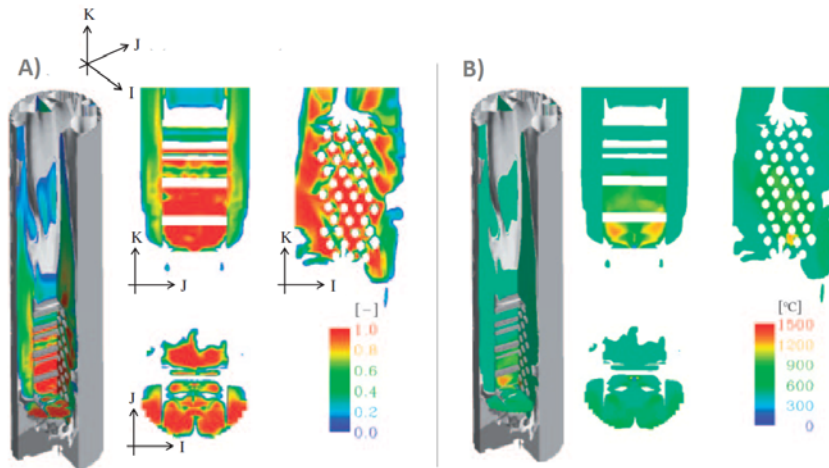


Figure 2.14: Results obtained by Takata et al. [25] after a 600 ms transient: A) void fraction and B) gas temperature.

The model developed by Takata et al. allows to obtain detailed numerical results about SWR, such as void fraction, temperatures, velocities as a function of time and space. The main critical aspect of Takata's modeling approach, is the hypothesis taken concerning the interfacial friction calculation, which is purely based on bubbly flow, with data obtained for bubbly flow of boiling

sodium inside SFR rod bundles. The applicability of this approach for a different geometry and, above all, different flow regimes, must be verified, since velocities and pressures in a gas-into-liquid jet are significantly higher than those occurring in typical bubbly flow in a rod bundle.

Uchibori et al. [29] carried on Takata et al.'s studies on steam-into-sodium jets. The mathematical model employed is the same as Takata et al., but Uchibori et al. developed a new interfacial momentum exchange approach, based on the "high mixing flow regime" defined by the RELAP5-3D [30] system code: droplet flow and bubbly flow are assumed for high void fractions and low void fractions, respectively, with a transition regime between them. The reaction model employed is the same as in Takata et al. Uchibori et al. fixed the gas injection pressure to 0.6 MPa. Mesh refinement is higher than in Takata et al.'s study. The numerical results of Uchibori et al. well represent the underexpansion at the nozzle outlet, with gas velocity increasing to supersonic values.

Besides the work realized by Takata et al. and Uchibori et al., other attempts of modeling SWR exist in literature. As an example, Kim et al. [31] realized a model for studying a steam generator tube failure scenario on a 2D domain: a tube sheet is considered, with one tube leaking. The authors employed a two-phase Euler-Euler approach. Concerning interfacial momentum transfer, the authors state that, since in their model there is no effect of a dispersed phase like particles and bubbles, and the objective of their research is not an understanding of the physical behaviors of the interaction between the phases, only the dominant drag force is considered in their research. No details are given regarding the definition of the drag law. RANS approach was employed, with a standard $k - \varepsilon$ model adopted to close the Reynolds stress. The turbulence model is applied to the two-phase mixture, so that it consists of two equations. The SWR was taken into account through the utilization of an eddy dissipation model: this approach is based on the assumption that chemical reaction is fast enough, relative to the transport process in the flow, that the reaction rate is directly related to the time required to mix the reactants at a molecular level. It follows that, since in turbulent flow the mixing time is dominated by the eddy properties, the reaction rate is inversely proportional to a mixing time defined by the turbulent kinetic energy and dissipation rate of the turbulent kinetic energy. No detail is given about the leakage dimension considered for the study and about the water vapor injection pressure. The authors only report the mass flow rate used as boundary inlet condition for the calculation. For a simulated transient of 0.1 seconds, Kim reports results concerning volume fraction and species distributions and velocity. Temperature increases due to the exothermic reaction considered. Maximum steam velocity inside the domain does not exceed 40 m/s, which is inconsistent with real steam generator conditions, for which gas features sonic speed at the leakage outlet. The information given in the published results by Kim et al. are not sufficient in order to comprehend all the assumption made and the model employed by the authors, such as the way of calculating interfacial friction and heat transfer, rather than consistency of gas conditions at the leakage outlet.

Outside the context of SWR, Gulawani et al. [32] investigated gas-into-liquid jets, for different reactive gas-liquid combinations. Two phase Euler-Lagrange description was employed by the authors, with RANS approach. Gas phase is

supposed to be in bubbly flow regime, assuming a constant bubble diameter of 0.5 mm for the calculation of the drag force. No detail is reported concerning the way this value was estimated. Assuming the reaction instantaneous, eddy dissipation model was employed by the authors in order to estimate the reaction rate. The gas injection velocity was fixed to a maximum value of 203.4 m/s, no detail of injection pressure is provided by the authors.

2.1.3 Assessment of the studies on underexpanded gas-into-liquid jets

In the previous paragraphs, an overview of the available experimental and numerical results on underexpanded gas-into-liquid jets has been given.

Concerning the experimental studies, relevant results have been obtained by Loth and Faeth, who confirm the presence of one or more shock waves at the outlet of the nozzle, due to gas underexpansion. The first study on the two-phase flow structure of such a flow was realized by Epstein et al., who investigated the mean size of liquid droplets entrained inside an underexpanded N₂-into-water jet. Epstein et al. performed their studies in the frame of SWR accidental scenario for SFRs: they stated that the data concerning droplet size distribution are a crucial parameter for use in a model of a reactive steam jet submerged in liquid sodium. In the same context and with the same goal, Kudoh et al. performed experimental studies of high velocity argon injection into liquid sodium: Kudoh's results, obtained with liquid sodium, validated Epstein's results, which were obtained in water. With the aim of developing a numerical model of a CO₂-into-sodium reactive jet, the knowledge of the entrained sodium droplet size in the near-field reaction zone is a fundamental aspect.

Interesting results on temperature distribution inside underexpanded gas-into-liquid-sodium reactive jets have been obtained by Sekkouti, for the case of SWR, and by Gicquel, for the case of SCR. These results provide knowledge about the temperature profiles that must be expected in this type of reactive two-phase flows.

Concerning numerical studies on underexpanded gas-into-liquid jets, a few models have been developed in literature. From what has been discussed in paragraph 2.1.2, the difficulty of developing a consistent numerical approach lies in the fact that poor knowledge exists on the two-phase structure of this type of two-phase flow. For these reasons, most of the numerical models described in paragraph 2.1.2 were developed adopting critical hypothesis regarding, for instance, the calculation of drag force between phases. Another difficulty is represented by the very high velocities of this two-phase flow, which is a critical aspect to deal with from the numerical point of view. From this point of view, the approach developed by Uchibori et al. can be considered as the most consistent with the available experimental knowledge, since it is the only model, among the ones presented in paragraph 2.1.2, that considers different flow regimes and that is capable of properly representing the jet underexpansion with sonic and supersonic gas velocities.

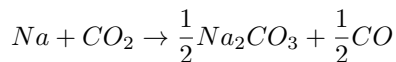
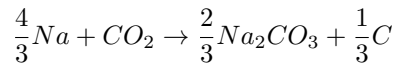
2.2 Bibliography study on sodium-CO₂ reaction

2.2.1 Studies by the Japan Atomic Energy Agency (JAEA)

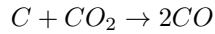
The JAEA has set up various experimental devices to study sodium-CO₂ reactions. Their description and the obtained results are reported by Miyahara et al. [33]. The first type of device was used to create surface contact, with no agitation, between a CO₂ flow and a sodium pool: CO₂ flows over liquid sodium, thus creating a gas space above the liquid sodium free surface. The gas is injected via two different lines: the maximum temperature of the injected gas is 260°C via the main line and 610°C for the secondary line. Sodium can be heated up to 650°C. The results obtained demonstrate three different reaction behaviours, according to the initial temperature of the sodium. For sodium temperatures lower 570°C and CO₂ temperatures no specified, the reaction occurs on the surface of the sodium pool. An aerosol is released during the first few seconds of the reaction. The sodium temperature does not change during the first few seconds. A small amount of CO was detected in the vented gases. At a sodium temperature of 600°C and a CO₂ temperature of 600°C (secondary line) and 260°C (main line), a combustion reaction occurs with an orange flame and a high production of aerosol for the first 100 seconds. The maximum temperature recorded in the gas phase above the sodium surface is 822°C. Some CO was detected in the vented gases, with a concentration that increased as the reaction progressed. For a sodium temperature of 580°C and CO₂ temperatures of 580°C (secondary line) and 240°C (main line), the reaction during the first few seconds takes place on the surface of the sodium pool. However, the flame reaction and production of aerosol started after around 158 seconds. Miyahara et al. explain that the cause of this reaction can be the emission of sodium droplets released via the surface by a few small explosions. The maximum temperature recorded in the gas phase above the sodium surface is 959°C. An aerosol was released during the first few seconds of the reaction. CO was detected in the vented gases, with a concentration that increased as the reaction progressed.

After the tests, the solid reaction products were analyzed by X-ray diffraction (XRD), energy dispersion X-ray (EDX), total organic carbon (TOC) analysis, and chemical analyzes. The elements present in the largest amounts in the reaction products are Na₂CO₃ and amorphous C. After a quantitative measurement of a sample of reaction products, the results give a mass fraction of 63% of Na₂CO₃, 0.1% of C, with the remainder being Na. No Na₂O or Na₂C₂O₄ was detected during the measurements of the reaction products.

Miyahara et al. proposed the following reaction pathway:



and, for a continuous reaction with flame, they added the reaction:



The second experimental device developed by JAEA to study the sodium-CO₂ reaction allows to inject CO₂ upwards in a vertical jet into a sodium pool, whose dimensions are 130 mm height and 55 mm inner diameter. The mass of sodium employed was about 200 g, which was equivalent to a sodium pool depth of about 100 mm. A sonic injector is used (maximum pressure 1.5 bar), with a diameter of 0.3 or 0.5 mm. The gas flow rate is 5×10^{-4} Nm³/min, constant for all the various tests carried out. The sodium can be heated to 550°C. The authors do not give any information on the possibility of heating the injected CO₂. Thermocouples are placed in the pool, with a minimum distance of 5 mm from the injector. For an initial sodium temperature of 250°C, no change in temperature was measured by the thermocouples and therefore no reaction was detected. With an initial sodium temperature of 300°C, a 25°C temperature rise was measured in the sodium. The authors assume that the cause of this reaction at a low temperature is due to the gas jet, which gives a renewed reaction surface. A final test was performed with sodium heated to 500°C. The thermocouples measure a temperature rise of only 20°C in the sodium bath. However, the temperature rises to 168°C in the gas covering the sodium surface. This means that the reaction occurs mainly in this area, between the CO₂ and the sodium droplets. Measurements performed on the reaction products show the presence of Na₂CO₃ and amorphous C. A visual test showed that these products must have accumulated along the CO₂ flow.

2.2.2 Studies by the Korea Atomic Agency Research Institute (KAERI)

The KAERI developed an experimental device to study sodium-CO₂ reaction. The results obtained are reported by Eoh et al. [34]. The main test section was a rectangular shape with an outer size measuring 180 mm in length, 60 mm in width, and 50 mm in height. The sodium tray was installed at the bottom center of the test section, and its size was 30 x 30 mm with a 15-mm depth. CO₂ gas flowed in a rectangular duct channel (40 x 20 mm), which is formed above the free surface of sodium inside the sodium tray. Thermocouples were placed on the sodium free surface, in the bulk sodium, and in the gas inlet and outlet of the CO₂ flow channels. The sodium mass at the beginning of the tests was about 20 g. Sodium and CO₂ could both be heated up to 600°C. All reaction behaviors were observed through a quartz window. The emitted gas, CO/CO₂ mixture, was continuously sampled into the gas analyzer and the concentration data were recorded during the test. In a first stage, sodium-CO₂ interaction tests were carried out for temperature range below the sodium temperature of 550°C. At the sodium temperature of 400°C, many dark traces with a thin solid layer covered the entire reacting surface. This is because the solid reaction products were formed on the reacting surface due to the reaction. But the unreacted part just below the thin solid layer remained clean, which indicates that the reaction was also limited to the reacting surface, and most reaction products were emitted back into the gas space. On the other hand, the sodium surface became very dirty above the sodium temperature of 450°C. In these

cases, more vigorous chemical reaction took place, and large amounts of reaction products were formed and covered the entire reacting surface. The covered crust became very thick and hard as the sodium temperature increased. This occurred because the vigorous interaction between sodium and CO_2 produced large amounts of sodium carbonate, carbon, sodium oxide, etc. Very little CO production occurred below the sodium temperature of 450°C . In contrast, the total amount of CO generation markedly increased as the reacting temperature rose above 450°C .

In most test cases with an initial sodium temperature lower than 550°C , no significant variations were observed in sodium temperature and system pressure during the reaction. This is because the chemical reaction took place on the free surface, and the reaction heat was primarily allocated to the gas space and continuously dumped into the atmosphere with the gas flow. Eoh et al. state that this feature is helpful to quantify the reaction rate, since uniform thermodynamic conditions could be achieved without condition change during the reaction.

When the initial sodium temperature was around 600°C , sodium ignition was observed with an orange-colored flame. This seemed to be an auto-combustion phenomenon. Unlike in the test at temperatures lower than 550°C , the temperatures of sodium and the vent gas significantly changed during the reaction. The maximum temperatures momentarily reached 900°C , measured by the thermocouples closest to the reacting surface.

The rate of the chemical reaction between liquid sodium and CO_2 gas was obtained by analyzing the concentrations of CO and CO_2 species in the vent gas. Two kinds of linear trends were created from the results, which are divided into temperature regions above and below 460°C , which, therefore, represents the threshold between the low and high reaction rate temperature ranges. To model the rate of the chemical reaction, the Arrhenius formula was proposed. It was found that the Arrhenius model well represents the interaction for the specified conditions in each region (temperature lower or higher than 460°C). The activation energies for different reaction temperature ranges can be obtained from the slope of the graphs, and the pre-exponential factors were determined in accordance with the separated activation energies. As a result, a two-zone reaction model with the threshold temperature of 460°C was obtained by reflecting the features of the rate-determining process. It was also found that the activation energies for each temperature zone are not sensitive to the CO_2 flow rate. For a sodium temperature range of $300\text{--}460^\circ\text{C}$, estimated activation energy was $27.34 \text{ kJ} \cdot \text{mol}^{-1}$ and the pre-exponential factor was $1.32 \cdot 10^{-4} \text{ kg} \cdot \text{m}^{-2} \cdot \text{s}^{-1}$. For a sodium temperature range of $460\text{--}550^\circ\text{C}$, estimated activation energy was $162.07 \text{ kJ} \cdot \text{mol}^{-1}$ and the pre-exponential factor was $580 \cdot 10^5 \text{ kg} \cdot \text{m}^{-2} \cdot \text{s}^{-1}$.

For all sodium temperatures, the major component of the solid reaction products was found to be sodium carbonate, and the quantity of formation steadily increased in proportion to the increase in sodium temperature.

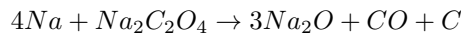
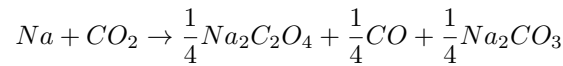
A second experimental facility was built by the KAERI for realizing CO_2 injection directly inside sodium. This involves a capsule 100 mm high which can contain 30 g of sodium. The sodium can be heated to 600°C . The gas is injected via a 1 mm nozzle. Tests were carried out with initial sodium temperatures of 200, 300, 400 and 600°C . For the test at 200°C , a maximum temperature rise of 18°C was measured in the sodium bath. The behaviour of the system

during the tests at 300 and 400°C was more or less the same, with temperature peaks of 1100°C for the tests at 300°C, and 923°C for the tests at 400°C. A considerable temperature rise was detected immediately after the injection of CO₂ into the sodium bath heated to an initial temperature 600°C. A temperature of 1130°C was measured in the sodium up to 4.4 min after the start of the injection. The reaction products include CO, which is always present in the gas, and its concentration increases for higher sodium temperatures. Na₂O and Na₂CO₃ were detected by XRD. Na₂CO₃ is a reaction product which is present during all the tests that were performed. Amorphous C was detected by Electron Probe Micro-Analysis and was found to be a reaction product for all the tests that were performed.

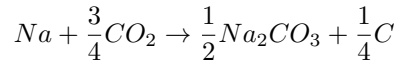
2.2.3 Studies by the CEA

Na-CO₂ reactions have been studied at the CEA by Gicquel [3]. The laboratory studies using calorimetry techniques seem to lead to a reaction pathway which differs according to the temperature.

For temperatures below 500°C, the following reaction was proposed by Gicquel:



Whereas, for temperatures above 500°C:



The reaction is highly dependent on the mode of contact between the sodium and the CO₂. The proposed reaction pathway considers contact conditions with agitation. An experimental facility was built in order to create CO₂ jets in liquid sodium. During the experimental tests, the temperature of the jet was measured using an assembly of twenty thermocouples moving in the sodium bath: it starts at the top position and moves downwards until it is at 1 mm from the gas nozzle. The time it takes to move down depends on the planned duration of the test. The total height of the test cell is 400 mm, diameter 100 mm, and it can contain up to 1.8 kg of sodium. The sodium can be heated to 600°C and the gas to 700°C (theoretical temperature achievable upstream the injector). Gas injectors with a diameter of 0.7 mm was used. The detailed description of the facility will be given in chapter 3.

Tests were carried out with different initial temperatures for the sodium and the CO₂. For initial temperatures of 400°C for both the sodium and the CO₂ (upstream of the injector), the maximum temperature measured by the thermocouples is 575°C, at a distance of 3 mm from the injector. For initial temperatures of 450°C for the sodium and 505°C for the CO₂ (upstream of the injector), the maximum temperature measured by the thermocouples is 1050°C, at a distance of 3 mm from the injector.

2.2.4 Assessment of the experimental studies on sodium – CO₂ reactions

The experimental results obtained by Eoh et al. and Gicquel for a surface contact (with or without agitation) between sodium and CO₂ clearly show the presence of a threshold temperature that separates low reaction rates from high reaction rates. From the results, this threshold can be assumed to lie between 460°C and 500°C.

Concerning CO₂-into-sodium jets, it is interesting to analyze the maximum temperatures in the sodium after injection of the CO₂. If the maximum temperatures inside the sodium after injection of the CO₂ are analyzed, the results obtained by JAEA are very different from those obtained by KAERI and by the CEA. The measurements do not show a large temperature rise during the tests carried out by JAEA (25°C), while temperatures of up to 1050°C and 1130°C were detected by the CEA and KAERI, respectively. The temperature peaks measured by KAERI, for an initial sodium temperature below 400°C, appear during the tests after induction periods in relation to the start of gas injection. On the other hand, for the test with an initial sodium temperature of 600°C, the temperature rise is immediate and the reaction is classed as continuous. The tests carried out by the CEA give more stationary temperature profiles than KAERI tests: the shape of the temperature profile is fairly regular during the different tests, with no temperature peaks measured after an induction periods. The 1050°C peak (measured by the CEA) was detected for an initial sodium temperature of 450°C, which corresponds to the highest temperature test performed by the CEA. For initial sodium temperatures below 450°C, the temperature measured does not exceed around 600°C. It can therefore be observed that there are no identical experimental results concerning the temperature variation determined by the sodium-CO₂ reaction. The temperature rises measured by KAERI contradict the temperature profiles measured by JAEA. A temperature rise comparable with that obtained by KAERI was found by the CEA, but only for tests with an initial sodium temperature above 450°C.

Figures 2.15 and 2.16 summarize the operative conditions and the results of all the experimental tests performed, both in a surface contact and jet configurations.

| Test | Type of Na-CO ₂ contact | Na temp. [°C] T _{Na} | CO ₂ temp. T _{CO₂} | CO ₂ flow rate | Type of reaction | Max temp. | CO concentration per unit area | Solid products (wt%) | | | Kinetics parameters | Reaction path deduced |
|---------|------------------------------------|----------------------------------|--|----------------------------|---|--------------------------------|--------------------------------|---------------------------------|---|-------------------------------|---|--|
| | | | | | | | | Na ₂ CO ₃ | Na (plus Na ₂ O and Na ₂ O ₂) | C plus others | | |
| JAEA-1 | surface | 600 | 600 | unknown (ambient pressure) | continuous reaction, with flame | 822 | - | 72 | 18.8 | 9.2 | - | |
| JAEA-2 | surface | 580 | 580 | unknown (ambient pressure) | delayed continuous reaction, with flame | 959 | - | 67.8 | 13.4 | 18.8 | - | aNa+bCO ₂ → xNa ₂ CO ₃ +yC+z CO |
| JAEA-3 | surface | <570 | 70 - 570 | unknown (ambient pressure) | surface reaction | no significant temp. variation | - | - | - | - | - | |
| KAERI-1 | surface | 300<T<460 | T _{Na} +/- 10 | 1 - 5 SLPM | rare, surface reaction | no significant temp. variation | 2.3 - 15.7 | 21.7 - 40.7 | 47.2 - 61.1 | 2.3 - 26 | E _a =27.34 kJ·mol ⁻¹ k ₀ =1.32·10 ⁻⁴ kg(m ⁻² ·s ⁻¹) | - |
| KAERI-2 | surface | 460<T<550 | T _{Na} +/- 20 | 1 - 5 SLPM | vigorous | no significant temp. variation | 7.0 - 299.4 | 16.4 - 25.9 | 47.2 - 61.1 | 16.6 - 34 | E _a =162.07 kJ·mol ⁻¹ k ₀ =5.80·10 ⁵ kg(m ⁻² ·s ⁻¹) | - |
| KAERI-3 | surface | >590 | - | 1 - 5 SLPM | auto-combustion (self-ignition) | 900 | - | - | - | 11 - 13 (of only amorphous C) | - | - |
| CEA-1 | surface | up to 700 | - | - | - | - | - | - | - | - | - | Na+CO ₂ → 1/4Na ₂ C ₂ O ₄ +1/4 CO+1/4Na ₂ CO ₃ for T<500°C Na+3/4CO ₂ → 1/2Na ₂ CO ₃ +1/4 C for T>500°C |

Figure 2.15: Operating conditions and results for the Na-CO₂ surface reaction tests.

| Test | Type of Na-CO ₂ contact | Na temp. [°C] T_{Na} | CO ₂ temp. T_{CO_2} | CO ₂ flow rate | Max temp. | CO concentration per unit area | Solid products (wt%) | | | Kinetics parameters | Reaction path deduced |
|---------|------------------------------------|---------------------------|-------------------------------------|--|---|--------------------------------|---------------------------------|---|---------------|---------------------|-----------------------|
| | | | | | | | Na ₂ CO ₃ | Na (plus Na ₂ O and Na ₂ O ₂) | C plus others | | |
| JAEA-4 | jet | 500 | - | $5 \cdot 10^{-4}$ Nm ³ /min (nozzle 0.3 mm) | 520°C inside Na; 668°C inside the gas phase above the sodium free surface | - | - | - | - | - | - |
| KAERI-4 | jet | 300; 400; 600 | - | $0.25-1.00 \cdot 10^{-4}$ Nm ³ /min (nozzle 1.0 mm) | 1100°C for $T_{Na} < 400$ 1130°C for $T_{Na} = 600$ | - | - | - | - | - | - |
| CEA-2 | jet | 400 | 400 | $7.3 \cdot 10^{-4}$ Nm ³ /min (nozzle 0.7 mm) | 575°C inside the two-phase jet | - | - | - | - | - | - |
| CEA-3 | jet | 450 | 505 | $7.3 \cdot 10^{-4}$ Nm ³ /min (nozzle 0.7 mm) | 1050°C inside the two-phase jet | - | - | - | - | - | - |

Figure 2.16: Operating conditions and results for the CO₂-into-Na tests.

Chapter 3

The experimental facilities

3.1 Experimental study on CO₂-into-sodium jets

3.1.1 Facility

The experimental device developed by the CEA for the study of CO₂-Na interactions has been described in Gicquel's PhD thesis. This facility, installed at CEA Cadarache, has been realized in 2009 with the purpose of studying CO₂-Na reactions, trying to reproduce a CO₂-into-Na jet occurring in the accidental heat exchanger leakage scenario. Figure 3.1 and 3.2 show the layout and a picture of this experimental device, called DISCO2 (from the French *Détermination des Interactions Sodium-CO₂*). The sodium pool (the "test cell" in figure 3.1), showed in figure 3.3, is placed inside a containment vessel. In this way, two walls separate sodium from external atmosphere. The cylindrical pool is 100 mm wide and 400 mm high and can be filled with maximum 1.8 kg of sodium. A resistance heating system placed on the pool wall allows to heat it up to 600°C, in order to bring liquid sodium to realistic operating temperatures inside the heat exchanger. The gas injection nozzle is placed in the center of the bottom of the pool. Carbon dioxide pressure can be regulated from 1 to 30 bars, and a heating system, placed just upstream the nozzle, allows heating the gas up to 600°C. Several thermocouples are properly placed in order to check the pool and the gas temperatures. Gas nozzles employed are classical sonic-nozzle type, with a convergent section and a sonic throat: an example is shown in figure 3.4.

Inside the sodium pool, temperature measurements can be performed thanks to a moveable thermocouple-comb: twenty thermocouples are placed along the comb, as shown in figure 3.5. The distance between two thermocouples depends on their placement: central thermocouples are closer to each other than the ones in the outer zone. Thermocouples are K-type class 1, with a diameter of 0.5 mm and a response time of 0.03 seconds ("response time" is defined as the time required to reach 63.2% of an instantaneous temperature change). The comb is guided by a 1-mm-step-by-step engine that allows to place it at the desired height inside the pool: in this way, axial and radial temperature profiles can be obtained during CO₂-into-Na injections. The acquisition frequency of thermocouples is 1Hz (one measurement per second). During the gas injection, the sodium pool pressure is kept constant since two gas outlets are placed at

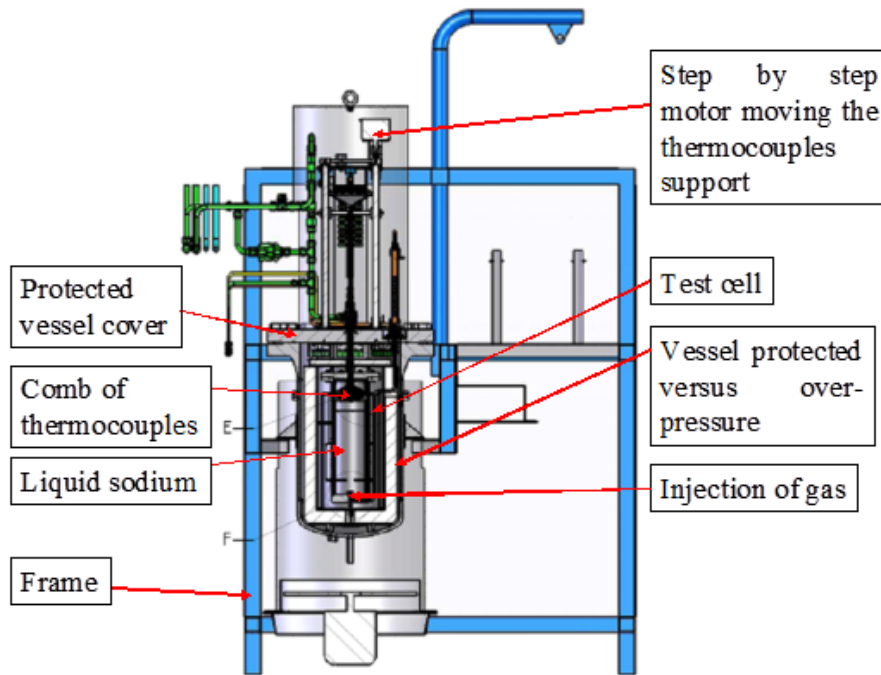


Figure 3.1: The DISCO2 experimental facility: layout.

the top of the pool. These outlets are directly connected to a cold-filter trap, aiming at preventing sodium aerosol to be vented outside.

Instrumentation is placed in the more important parts of the device: thermocouples and pressure transmitters are placed on the sodium pool, the containment vessel and inside all gas piping, and flow rate sensors allow checking gas flow rate inside the main ducts.

3.1.2 Experimental conditions and test procedures

The test cell is filled with solid sodium in an inert Argon atmosphere. Solid sodium is, then, liquified in order to obtain an homogeneous level of sodium inside the cell. Before transferring the cell inside the DISCO2 facility, sodium is let solidify. Once installed inside DISCO2, the cell air-tightness is checked and an inert argon cycle is performed over the entire facility. A minimum argon flow is constantly supplied during the entire test, in order to guarantee that no oxygen is present inside the cell. Argon is constantly supplied also to the nozzle, in order to prevent liquid sodium to enter inside it. At this point, the cell heating can start: during these procedures, cell temperatures at different positions can always be checked from the control room. The desired temperature to be achieved inside the sodium pool is given to the software at the beginning of the test, and once reached, it is automatically kept constant by the software. Before beginning the CO_2 injection, the comb of thermocouples, that until this point is kept in the upper position inside the cell (in order to be kept outside the sodium), is placed at the desired height inside the cell.



Figure 3.2: The DISCO2 experimental facility: picture.

Since sonic conditions are achieved inside the injection nozzle, the CO_2 mass flow rate is controlled by the pressure fixed upstream the nozzle, which is manually regulated before the beginning of the test. The system automatically switches from argon to CO_2 injection. The duration of the CO_2 injection is established at the beginning of the test. Once the CO_2 injection is stopped, sodium is let cooling down, with argon continuing to flow inside the cell.

Figure 3.6 shows the state of the comb of thermocouples after a CO_2 injection test: a layer of solid sodium, oxidated sodium and products of reaction covers it.



Figure 3.3: The test cell filled with sodium. Inside the cell the rails for the movement of the comb of thermocouples can be seen.

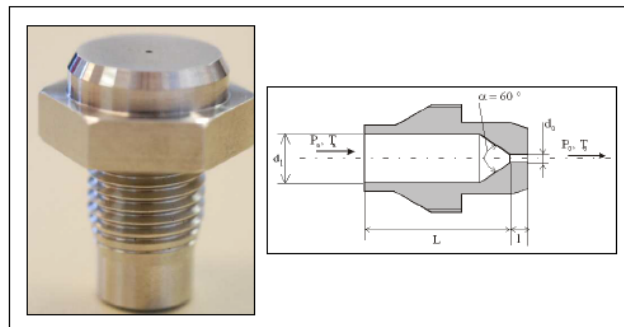


Figure 3.4: The sonic nozzle employed for gas injection into the liquid sodium.



Figure 3.6: A picture of the comb of thermocouples after an experimental test.

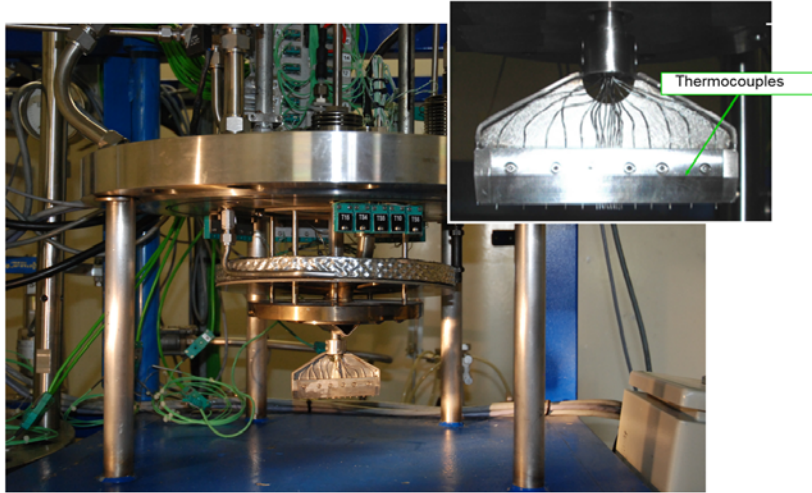


Figure 3.5: The comb of thermocouples: the test cell filled with sodium has been removed in the picture .

3.2 Experimental study on underexpanded gas-into-water jets

Besides the sodium facility DISCO2, an experimental apparatus has been built during this thesis work, in order to study underexpanded gas-into-water jets. According to the final goal of developing a model for the reactive CO_2 -into-sodium jet studied experimentally, the same geometry of the liquid sodium pool used in the DISCO2 facility has been chosen for realizing non-reactive gas-into-water jets. The exact geometry of the test facility is shown in figure 3.7A. Gas is injected into the cylindrical pool filled with water, through a 1 mm diameter nozzle placed in the center at the bottom of the pool. The gas injection pressure is regulated through a pressure regulator valve placed at the bottle outlet. The pool wall is made of transparent plexiglass, allowing to perform visual observations. The top of the pool is entirely opened, in order to allow instrumentation accommodation. An optical probe has been employed for local void fraction measurement, at different positions inside the pool. Measurements have been realized through a single-tip probe, fabricated by the French industry “RBI-instrumentation”.

Considering the high gas velocity near the nozzle outlet, sapphire was chosen as probe material, mechanically stronger than the glass fiber option. The diameter of the sapphire tip is in the range of 10–50 μm . The scheme of the apparatus is shown in figure 3.7B, whereas a picture of it is shown in figure 3.8. The optical probe, inserted inside the pool from the top open surface, was fixed to a mechanical arm controlled by a 3-axis moving system which allows placing the probe at different axial and radial positions.

The step-by-step electric motor features 300 steps per millimeter in both axial and radial directions. However, since an axial and radial reference zero has to be fixed in order to calculate the position of the probe during the tests, the effective accuracy of the probe positioning system is affected by the accuracy of

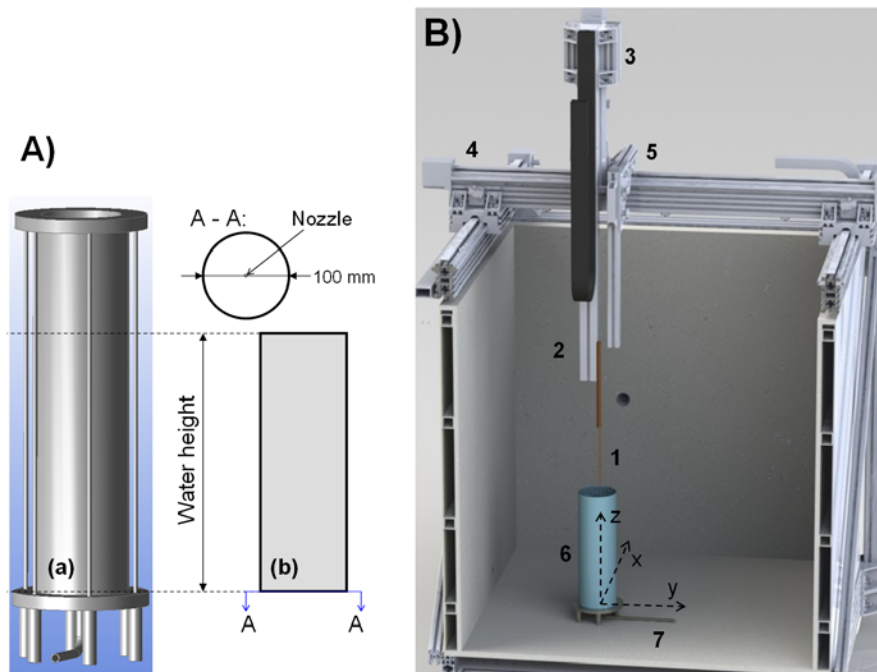


Figure 3.7: (A) Illustration of the apparatus employed for the gas-into-water injection: entire representation (a) and frontal view of the effective domain filled by water (b). (B) Representation of the complete experimental system developed for performing optical probe measurements: (1) optical probe, (2) mechanical arm for probe location, (3) step-by-step axial-direction engine, (4) and (5) step-by-step radial-direction engines, (6) apparatus described in A), (7) connection to gas-bottle.

defining the reference zero. The axial and radial zero was placed at the center of the nozzle exit, with a precision of ± 1 mm. The optical probe is connected to an opto-electronic device also provided by RBI-instrumentation. The conversion of the optical signal (quantity of light reflected) into an electrical signal is ensured by a photo-sensitive element. This analogical signal is then amplified, thresholded and converted into a binary signal, which is the time function indicating when the tip is alternatively in contact with liquid and gas. This TTL signal is provided to an acquisition board. Its operating frequency is 20 MHz, which guarantees a very high time resolution directly affecting the accuracy of void fraction measurement. Once acquired and stored, the binary signals are processed by a dedicated software in order to obtain the local values of void fraction. Once the gas injection has begun, optical probe measurements are realized in different positions. For each position, a number of 2000 liquid-gas fluctuations (corresponding to 2000 transitions in the binary signal) was fixed as the minimum value to be achieved in order to obtain a statistically converged average value of gas void fraction. Initially, a water height of 300 mm was used: however, a certain quantity of water was pushed to exit from the top of the pool, due to high pressure gas injection from the bottom, leading

to a variable water height during the tests. For this reason, for void fraction measurements, water height was fixed at 200 mm, the maximum operable water height in order not to have water loss during the gas injection (considering the gas injection total pressure of 0.7 MPa, as it will be described in Section 5). In order to avoid mechanical problems on the optical sapphire tip caused by extremely high gas velocities, measurements were performed starting from an axial position of 30 mm downstream the nozzle.

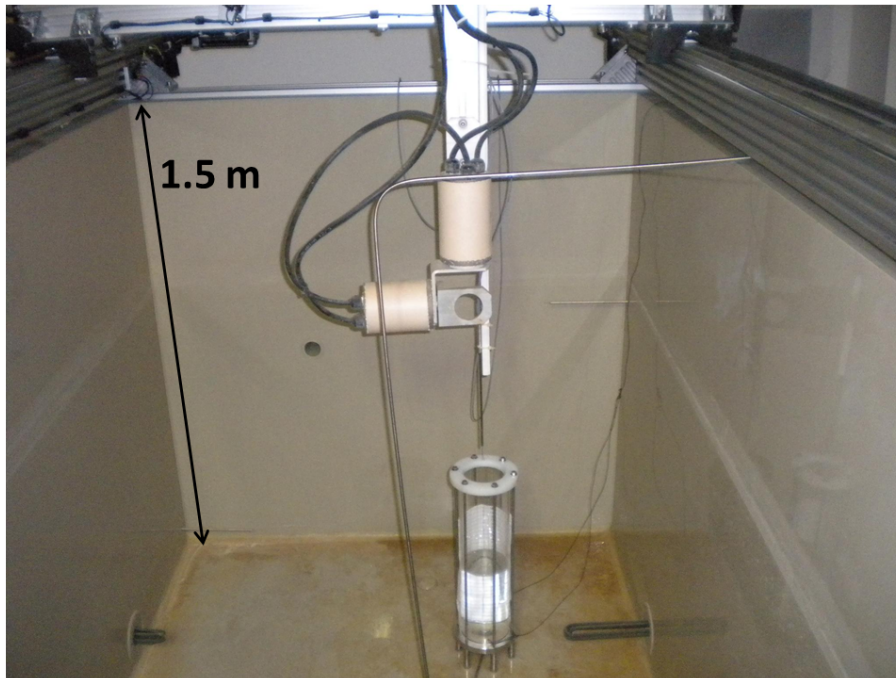


Figure 3.8: A picture of experimental system showing the mechanical arm, the optic probe, the water pool.

The different axial and radial positions where the measurements are desired are given to the software controlling the step-by-step engine. Once a measurement is completed in one position, the optic probe is automatically moved to the next programmed position where a new measurement starts.

Chapter 4

Non-reactive gas-into-liquid jet

Nomenclature:

- α : volume fraction [-]
- U : velocity [$m \cdot s^{-1}$]
- t : time [s]
- ρ : density [$kg \cdot m^{-3}$]
- P : pressure [Pa]
- μ : dynamic viscosity [$Pa \cdot s$]
- λ : thermal conductivity [$W \cdot (mK)^{-1}$]
- E : total energy [$kJ \cdot kg^{-1}$]
- g : gravitational acceleration [$m \cdot s^{-2}$]
- d : diameter [m]
- T : temperature [K]
- S : mass transfer source term due to heterogeneous reactions [$kg \cdot (m^3s)^{-1}$]
- S^U : momentum transfer due to heterogeneous reactions [$N \cdot m^{-3}$]
- F : interfacial force [$N \cdot m^{-3}$]
- h : enthalpy [$kJ \cdot kg^{-1}$]
- Q : interfacial heat transfer [$kJ \cdot (m^3s)^{-1}$]
- S^H : energy source term due to heterogeneous reactions [$kJ \cdot (m^3s)^{-1}$]
- F_D : drag force [N or $N \cdot m^{-3}$]
- C_D : drag coefficient [-]
- a : interfacial area [m^{-1}]

- F_L : lift force [N or $N \cdot m^{-3}$]
- F_{VM} : virtual mass force [N or $N \cdot m^{-3}$]
- σ : surface tension [$N \cdot m^{-1}$]
- h : heat transfer coefficient [$W \cdot (m^2 K)^{-1}$]
- We : Weber number
- k : turbulent kinetic energy [$m^2 \cdot s^{-2}$]
- ε : turbulent kinetic energy dissipation rate [$m^2 \cdot s^{-3}$]

Subscripts:

- p : relative to the generic phase p
- q : relative to the generic phase q
- m : gas-liquid mixture
- pq : from phase p to phase q
- d : droplet
- b : bubble

4.1 Modeling approach

4.1.1 Preliminary considerations

In considering two-phase flows, a crucial aspect is the definition of the specific two-phase regime (or pattern). The classical example regards two-phase flows in pipes.

In horizontal pipe, flow patterns for fully developed flow have been reported in numerous studies. Transitions between flow patterns are gradual, and subjective owing to the visual interpretation of individual investigators. Bubbly flow is prevalent at high ratios of liquid to gas flow rates: the gas is dispersed as bubbles which move at velocity similar to the liquid and tend to concentrate near the top of the pipe at lower liquid velocities. Plug flow describes a pattern in which alternate plugs of gas and liquid move along the upper part of the pipe. In stratified flow, the liquid flows along the bottom of the pipe and the gas flows over a smooth liquid/gas interface. Similar to stratified flow, wavy flow occurs at greater gas velocities and has waves moving in the flow direction. When wave crests are sufficiently high to bridge the pipe, they form frothy slugs which move at much greater than the average liquid velocity. In annular flow, liquid flows as a thin film along the pipe wall and gas flows in the core. Some liquid is entrained as droplets in the gas core. At very high gas velocities, nearly all the liquid is entrained as small droplets. This pattern is called spray, dispersed, or mist flow.

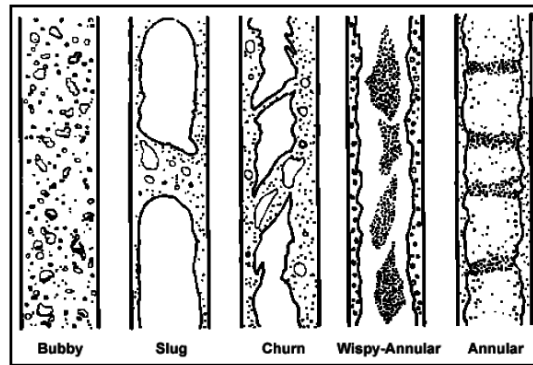


Figure 4.1: different flow patterns in a vertical upward pipe.

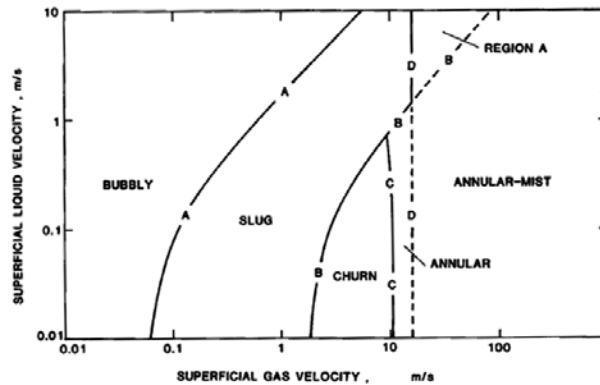


Figure 4.2: two-phase flow map of Ishii[35].

A variety of flow pattern can be individuated also for fully developed co-current upflow of gases and liquids in vertical pipes, as shown in figure 4.1. Bubbly flow with dispersed gas bubbles in continuous liquid, slug flow where the gas forms large Taylor bubbles of diameter nearly equal to the pipe diameter. Churn flow is characterized by strong intermittency and intense mixing, with neither phase easily described as continuous or dispersed. Ripple flow has an upward-moving wavy layer of liquid on the pipe wall: it may be thought of as a transition region to annular, annular mist, or film flow, in which gas flows in the core of the pipe while an annulus of liquid flows up the pipe wall. Some of the liquid is entrained as droplets in the gas core. Mist flow occurs when all the liquid is carried as fine drops in the gas phase: this pattern occurs at high gas velocities. Approximate prediction of flow pattern may be quickly done using flow pattern maps, an example of which is shown in figure 4.2 and figure 4.3: the first considers gas and liquid superficial velocities as the parameters employed to determine the two-phase pattern, the latter considers the mass flux (in $kg/(m^2s)$).

The bubbly to slug flow transition is presumed to occur when the maximum packing of small bubbles is reached. The slug to churn flow transition is assumed to occur when the void fraction in the liquid slug was equal to the void

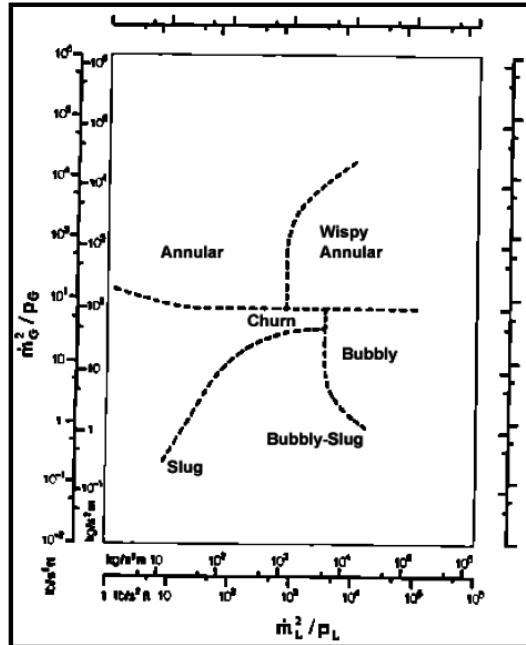


Figure 4.3: two-phase flow pattern map of Hewitt and Roberts [36].

fraction in the Taylor bubble section. For the transition to annular flow, two transition mechanisms are identified. The first is flow reversal in the liquid film that exists in churn flow. The second is droplet entrainment. From figures 4.2 and 4.3, one can see that for low gas velocities and low void fractions (volume of gas to total volume ratio), gas tends to represent the dispersed phase (bubbly, slug flows); whereas for high gas velocities and gas void fractions, gas acts as continuous phase, with liquid representing the dispersed phase.

When highly pressurized gas is injected through a small nozzle into a liquid bath at atmospheric pressure, choked conditions and consequent gas speed of sound are reached at the nozzle throat. If pressure at choked conditions is still higher than downstream liquid pressure, underexpansion occurs downstream the nozzle, leading to local supersonic gas velocities in the liquid. As a consequence, slip velocity between gas and liquid phases at the nozzle outlet is very high. This is the case of a CO_2 leakage inside the CO_2 -sodium heat exchanger of an SFR. In the region close to the nozzle, the gas-liquid interface is continuously broken due to the instabilities caused by the high friction velocities, and liquid entrainment occurs inside the core gas phase: this mechanism leads to the presence of a mist flow, and this assumption is confirmed by the flow maps, which consider mist flow for high gas velocities and void fractions.

All the two-phase flow patterns and regime maps detailed so far, have been found to be valid for two-phase flows in pipes. The two-phase jet flow considered in this work does not represent a pipe flow. Therefore, more detailed evaluations must be performed before considering applicable, for the present study, the flow maps available in literature. The experimental facility described in paragraph 3.2 was utilized to perform gas-into-water underexpanded jets, in

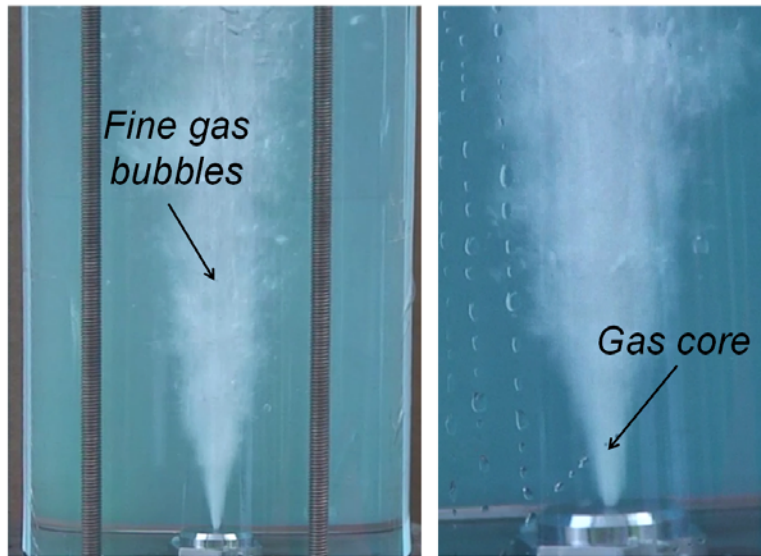


Figure 4.4: 1.0 MPa CO_2 injected into water: visible flow patterns.

order to gain knowledge about the characteristic two-phase patterns of such a flow. Figure 4.4 shows CO_2 injected into water: gas is injected at a stagnation pressure of 1.0 MPa, through a 1.0 mm nozzle. Visual observations allow to discern a gas core in the area very close to the nozzle, where gas expansion is enclosed: liquid entrainment can occur in this region, due to high interfacial velocities leading to instability and breaking of the gas-liquid interface. Droplet visual detection could not be possible with the experimental facility used. However, several studies are available in literature, which confirm liquid entrainment in gas-into-liquid jets. Bell et al. [37], in 1972, studied liquid entrainment through experimental tests with submerged impinging gas jet: they found that liquid entrainment occurred and they also developed correlations for the estimation of the size of the entrained droplets, depending on local flow conditions. Recently, as already discussed in paragraph 2.1, further studies have been realized by Epstein et al. [21], Someya et al. [38] and Kudoh et al. [22], which confirm the mechanism of liquid entrainment and droplet formation following high pressure and high velocity gas-into-liquid injection.

Looking at figure 4.4, one can observe a second region, further downstream the nozzle, where jet cross-section is wider and gas packing conditions decrease. In this zone, gas atomization seems to occur, with fine gas bubbles rising in continuous liquid. Besides some isolated bigger bubbles along the border region of the jet, the homogeneous gas plume observed suggests that bubbles in this region are very small with a relative constant size. Bubble coalescence seems to appear starting from a certain axial distance downstream the nozzle: besides classical bubble coalescence mechanism, it must be taken into account the fact that, at the top air-water free surface, the upward jet tends to push some water outside the free surface and to entrain some air inside the water, which increases the local void fraction and contributes to bubble coalescence. This phenomenon is clearly visible in figure 4.5. Therefore, it seems that, for the



Figure 4.5: a) Water height before gas injection; b) gas coalescence induced by the open surface.

initial water height employed for the visual tests (300 mm), bubble coalescence plays a minor role in the region not influenced by the free surface. One must consider that no open free surface is present in real heat-exchanger geometries.

4.1.2 Two-phase flow modeling approach

Several numerical modeling approaches are employable for describing two-phase flows. Two main families can be distinguished: homogeneous models and multi-fluid models. In the following, the discussion will be limited to the case of two-phase gas-liquid flows; nevertheless, the same theoretical approaches are extendable to any kind of multi-phase flow.

When adopting a homogeneous approach, the two-phase flow is treated as a single phase gas-liquid mixture flow: the flow-dynamic constitutive equations are solved for the mixture, and physical properties and variables refer to the mixture. Moreover, in the present formulation of the constitutive equations, the following assumptions are retained:

- the two phases share the same pressure;
- the diffusion stress is equal to zero;
- slip velocities are small;

- turbulence is not considered (i.e. the Reynolds stress is taken equal to zero).

In the standard homogeneous approach for compressible flows, governing equations are solved for the conservation of mass (eq. 4.1), momentum (eq. 4.2) and energy (eq. 4.3) for the mixture, together with an equation for the conservation of the volume fraction of one phase (eq. 4.6).

$$\frac{\partial \rho_m}{\partial t} + \nabla \cdot (\rho_m \vec{U}_m) = 0 \quad (4.1)$$

$$\begin{aligned} \frac{\partial}{\partial t} (\rho_m \vec{U}_m) + \nabla \cdot (\rho_m \vec{U}_m \vec{U}_m) = & -\nabla P + \\ \nabla \cdot \left[\mu_m \left(\nabla \vec{U}_m + (\nabla \vec{U}_m)^T \right) \right] + \rho_m \vec{g} \end{aligned} \quad (4.2)$$

$$\frac{\partial}{\partial t} (\rho_m E_m) + \nabla \cdot (\vec{U}_m (\rho_m E_m + P)) = \nabla \cdot (\lambda_m \nabla T_m) \quad (4.3)$$

Where U_m is the mixture velocity, P the pressure of the mixture, \vec{g} the gravity acceleration and E_m the total specific energy of the mixture. The mixture density ρ_m and the mixture dynamic viscosity μ_m are evaluated through a volume-average on the phases p :

$$\rho_m = \sum_p \alpha_p \rho_p \quad (4.4)$$

$$\mu_m = \sum_p \alpha_p \mu_p \quad (4.5)$$

Through the continuity equation of phase q , it is possible to calculate the volume fraction transport of this phase:

$$\frac{\partial (\alpha_q \rho_q)}{\partial t} + \nabla \cdot (\alpha_q \rho_q \vec{U}_m) = (m_{pq} - m_{qp}) + S_q \quad (4.6)$$

In 4.6, m_{pq} and m_{qp} represent the source terms taking into account mass transfer from phase p to phase q and viceversa, respectively, due to condensation or evaporation. S_q is a source term taking into account mass creation of phase q due, for example, to chemical reactions.

The standard homogeneous model described assumes continuous interpenetrating phases. Approaches have been developed for non-interpenetrating (for example, free surface flows) phases. As an example, the Volume Of Fluid (VOF) approach can be cited, which employes a scheme to locate the surface and an algorithm to track the surface as a sharp interface moving through a computational grid.

A more rigorous approach to treat two-phase flows is obtained employing a two-fluid model, in which governing equations are solved separately for each phase, with source terms taking into account the interphase interactions. The Eulerian-Lagrangian approach can be considered as a two-fluid model, even if the Navier-Stokes equations are solved only for the continuous phase, while the trajectories of the individual dispersed phase are tracked in a Lagrangian frame of reference. This approach can provide a detailed description of individual bubble (or droplet) motion, such as interactions with neighboring bubbles (or droplets), and it is typically employed for droplet combustion in fuel-air systems. However, other physical phenomena such as regime transition are not possible to be represented. Moreover, this approach requires an intensive computational load especially when the dispersed phase is not sufficiently dilute.

The two-fluid approach that solves the Navier-Stokes equations for each phase is the Euler-Euler model. The two-fluid Euler-Euler model was first proposed back in the late 1960s and early 1970s by Ishii [39]. The basic approach of the two-fluid model is to formulate the conservation equations of mass, momentum and energy for a fixed control volume where both phases co-exist with the assumption of interpenetrating continua or fluids. This balance must be satisfied at any point in space and at any time, and thus requires local instantaneous governing equations for each phase and local instantaneous jump conditions, i.e., the interactions between the phases at the interface. Each phase is governed by its conservation equation of mass, momentum, and energy. In addition, the probability of occurrence of an individual phase at one spacial location is specified by the instantaneous volume fraction of that phase at that point. For high dispersed phase fractions, the computational load does not increase, in contrast with the Eulerian-Lagrangian approach. The Euler-Euler approach is more suitable for two-phase regime transition cases where the dispersed phase changes from one fluid to the other along the computational domain: this cannot be achieved with the Eulerian-Lagrangian approach, where the dispersed and continuous phases must be strictly always the same along the computational domain, as they are described by the dispersed particle motion equation and Navier-Stokes equation, respectively.

The following assumptions are retained for the present formulation of the constitutive equations of the Euler-Euler approach:

- the two phases share the same pressure;
- turbulence is not considered (i.e. the Reynolds stress is taken equal to zero).

In the Euler-Euler approach, the mass conservation equation is solved for each phase:

$$\frac{\partial(\alpha_p \rho_p)}{\partial t} + \nabla \cdot (\alpha_p \rho_p \vec{U}_p) = (m_{pq} - m_{qp}) + S_p \quad (4.7)$$

Where ρ_p , α_p and \vec{U}_p are density, volume fraction and velocity of the generic phase p , respectively. m_{pq} , m_{qp} and S_p have the same meaning as in equation 4.6.

Navier-Stokes momentum equations are solved for each phase:

$$\begin{aligned} \frac{\partial}{\partial t} (\alpha_p \rho_p \vec{U}_p) + \nabla \cdot (\alpha_p \rho_p \vec{U}_p \vec{U}_p) = & -\alpha_p \nabla P + \\ & \nabla \cdot \left(\alpha_p \mu_p \left(\nabla \vec{U}_p + (\nabla \vec{U}_p)^T \right) \right) + \\ & \alpha_p \rho_p \vec{g} + S_p^{\vec{U}} + \vec{F}_{pq} \end{aligned} \quad (4.8)$$

Where μ_p is the dynamic viscosity of phase p . Eq. 4.8 has the same form of eq. 4.2, with the addition of two terms: $S_p^{\vec{U}}$, representing the momentum transfer caused by heterogeneous reactions, and \vec{F}_{pq} , which represents the interfacial force source term.

As one can notice from eq. 4.8 and as already stated in the initial assumptions, the two phases share the same pressure P ($P_p = P_q = P$). In fact, if one considered two pressure fields, the five unknowns \vec{U}_p , \vec{U}_q , α , P_p , P_q would have to be calculated with four equations (two continuity and two momentum equations). This is the reason why all the validated two-fluid models existing today are based on one pressure field shared by all phases. Nevertheless, research is currently in progress on two-pressure two-fluid models.

If compressibility and/or heat transfer enter into the formulation, energy equation must be solved for each phase:

$$\begin{aligned} \frac{\partial}{\partial t} (\alpha_p \rho_p h_p) + \nabla \cdot (\alpha_p \rho_p \vec{U}_p h_p) = & -\alpha_p \frac{\partial P}{\partial t} + \\ & \nabla \cdot (\alpha_p \lambda_p \nabla T_p) + Q_{pq} + S_p^H \end{aligned} \quad (4.9)$$

Where h_p and λ_p are the enthalpy and the thermal conductivity of phase p , respectively, Q_{pq} is the interfacial heat transfer flux and S_p^H is the source term taking into account, for example, heat due to exothermic or endothermic chemical reaction.

From the considerations detailed in paragraph 4.1.1, the following aspects must be taken into account in order to properly choose the numerical approach for the modeling of an underexpanded gas-into-liquid jet:

1. Important compressibility effects must be considered in the gas phase at the leakage outlet, meaning sharp change in gas density, temperature and velocity;
2. Very high gas and slip velocities characterize the leakage outlet and the first downstream region: from sonic conditions inside the leakage throat, underexpansion leads to gas supersonic velocities;
3. Following visual observations, a flow-regime transition occurs, since mist flow characterizes the region near the nozzle (leakage), and bubbly flow the region further downstream.

Point 1 suggests that gas phase density plays a crucial role and it should be properly described: in a homogeneous approach, density is treated as a phase volume averaged density (eq. 4.4), meaning that, for the present case, highly

variable gas density would be averaged with constant liquid density. From point 2, it follows that, as already stated, high slip velocities exist between gas and liquid: with a homogeneous approach, only one velocity field (the mixture field) can be calculated, whereas in a two-fluid approach two separated gas and liquid velocity fields are calculated. In a homogeneous model, dispersed phase dimensions and flow patterns do not enter in the calculation, since dispersed and continuous phases are merged into a mixture single-phase. Therefore, point 3 becomes a limiting aspect only in the case of the adoption of a two-fluid model. As already discussed, the Eulerian-Lagrangian approach is not suitable for representing a two-phase regime transition.

As a result of all these considerations, a two-fluid Euler-Euler approach has been adopted in the present work: constitutive equations for the gas phase allow to properly take into account gas phase flow dynamics, gas and liquid velocities are calculated separately, and two-phase regime transitions can be taken into account.

4.1.3 Euler-Euler interfacial momentum closure laws

The crucial aspect when dealing with a two-fluid approach, is the definition of the interfacial transfer. The source terms m_{pq} and m_{qp} , F_{pq} and Q_{pq} in equations 4.7, 4.8 and 4.9, respectively, take into account the mass, momentum and energy transfer from one phase to the other at their interface. If phase p receives a certain momentum quantity F_{pq} from phase q , at the same time phase q must lose the same quantity F_{qp} : therefore, the equation $F_{pq} = -F_{qp}$ (and, of course, $|F_{pq}| = |F_{qp}|$) must be always verified. The same is true for the interfacial energy transfer and for evaporation/condensation mass transfer.

The term F_{pq} , often called interfacial friction, takes into account momentum transfer caused by different forces, such as drag force, lift force, virtual mass force, turbulence interactions.

Drag force, F_D , is a force exerted by the surrounding fluid to the moving particle: its direction is parallel to the particle trajectory and its verse is opposite to the particle trajectory. A particle that moves relative to a liquid accelerates part of the liquid around it and is, in turn, slowed down by the surrounding liquid. This drag force is the dominant contribution to the interaction force and often it is the only one considered. Drag force on one particle can be derived through equation 4.10:

$$F_D = \frac{1}{2} C_D \rho U_r^2 S \quad (4.10)$$

Where C_D is the drag coefficient, U_r the relative velocity, ρ the density of the surrounding fluid and S the projected sectional area of the particle. For a sphere, the projected sectional area is $\pi \frac{d^2}{4}$, d being the diameter of the sphere. Several definitions of dispersed phase diameter exist. When dealing with a large number of particles, it may not be possible to measure or simulate each particle, such that average particle characteristic dimension can be useful for describing a group of particles. For multiphase flows with a large variation in particle diameter, an average diameter can be employed to represent the dynamics or coupling of the particles, as it is computationally convenient. For a

polydisperse diameter distribution, one can define several “average” diameters based on a measured or interpolated distribution function. In addition, “effective” diameters for certain fluid dynamic phenomena can be determined based on such averages and identification of the controlling physics.

Measurements of the size distribution are obtained in a series of bins representing discrete ranges of particle diameter. The resulting size distribution is commonly referred to as a size probability distribution function (PDF). The number-based probability distribution function, $P_N(d)$, is then the number of particle in each bin normalized by the total amount of particles measured. Since $P_N(d)$ represents the fraction of particles per bin diameter increment (Δd) it has units of one over length. Thus, $P_N(d)$ represents the probability of a particle’s diameter being within $\pm\Delta d$ of the bin diameter. The sum of these discrete probabilities should be unity:

$$\sum_{i=1}^M P_N(d) \Delta d = 1$$

where M is the number of bins and Δd is the bin width. The integral of the continuous representation of the PDF over all possible particle diameters is also unity:

$$\int_0^{\infty} P_N(d) dd = 1$$

Three simple diameter averages are the number-averaged diameter (d_{10}), the area-averaged diameter (d_{20}) and the volume-averaged (d_{30}) which are defined as:

$$d_{10} = \int_0^{\infty} P_N(d) d dd$$

$$d_{20} = \left[\int_0^{\infty} P_N(d) d^2 dd \right]^{\frac{1}{2}}$$

$$d_{30} = \left[\int_0^{\infty} P_N(d) d^3 dd \right]^{\frac{1}{3}}$$

A common average diameter used in engineering systems is the Sauter mean diameter (SMD) defined as:

$$d_{32} = \frac{\int_0^{\infty} P_N(d) d^3 dd}{\int_0^{\infty} P_N(d) d^2 dd} = \frac{d_{30}^3}{d_{20}^2}$$

Physically, the Sauter mean diameter represents a particle whose surface area to volume ratio is the same as that of the whole mixture (that is, total surface

area of the particles versus the total volume of the particles). The area-to-volume ratio for a particle having a Sauter mean diameter is:

$$\left| \frac{A_{32}}{V_{32}} \right|_{particle} = \frac{4\pi \left(\frac{d_{32}}{2}\right)^2}{\frac{4}{3}\pi \left(\frac{d_{32}}{2}\right)^3} = \frac{6}{d_{32}}$$

In order to estimate the interfacial area per unit volume, one can write:

$$a = \frac{A_{interfacial}}{unit\ volume} = \frac{A_{interfacial}}{\frac{V_{particle}}{\alpha}}$$

But:

$$\left| \frac{A_{32}}{V_{32}} \right| = \frac{A_{interfacial}}{V_{particle}}$$

Then, the interfacial area per unit volume is:

$$a = \frac{6\alpha}{d_{32}} \quad (4.11)$$

Equation 4.11 is the one employed for the estimation of the interfacial area in two-phase flows, when using the SMD definition for the dispersed phase dimension. Following equation 4.10, the drag exerted by a single particle p on the continuous phase c is:

$$\vec{F}_{D_{p \rightarrow c}} = \frac{1}{2} C_D \rho_c \pi \frac{d^2}{4} \left| \vec{U}_p - \vec{U}_c \right| \left(\vec{U}_p - \vec{U}_c \right) \quad (4.12)$$

The number of particles per unit volume, N_p , is given by:

$$N_p = \frac{\alpha}{V_{particle}} = \frac{6\alpha}{\pi d^3}$$

Hence the total drag exerted by the dispersed phase dp per unit volume on the continuous phase is:

$$\vec{F}_{D_{dp \rightarrow c}} = \frac{3}{4} \frac{C_D}{d} \alpha \rho_c \left| \vec{U}_p - \vec{U}_c \right| \left(\vec{U}_p - \vec{U}_c \right) = \frac{1}{8} C_D a \rho_c \left| \vec{U}_p - \vec{U}_c \right| \left(\vec{U}_p - \vec{U}_c \right) \quad (4.13)$$

Lift force, F_L , is a force exerted by the surrounding fluid to the moving particle: its direction is orthogonal to the particle trajectory. Auton [40, 41] showed that the lift force on a clean spherical bubble in steady inviscid flow is proportional to the cross product of the vorticity of the continuous phase and the relative

velocity between the two phases. Hence, he proposed the following equation of the lift force for a single spherical particle of volume V_p in an infinite medium:

$$\vec{F}_L = C_L \rho_c V_p \left| \vec{U}_r \times (\nabla \times \vec{U}_c) \right| \quad (4.14)$$

C_L is the lift coefficient. Therefore, the total drift force exerted on the dispersed phase per unit volume is:

$$\vec{F}_L = C_L \rho_c \alpha \left| \vec{U}_r \times (\nabla \times \vec{U}_c) \right| \quad (4.15)$$

Virtual mass effect occurs when a secondary phase accelerates relative to the primary phase. When a particle flows through a quiescent continuous phase, some of the continuous phase mass is carried by the particle due to kinetic energy transfer. This mass portion is supposed to attain the same particle velocity, resulting in a virtual increase in the particle mass. It is a common agreement that the virtual mass force is equal to the mass of continuous phase carried by the particle times a suitable defined relative acceleration (A_{rel}) between phases, as:

$$F_{VM} = C_{VM} \rho_c V_p A_{rel} \quad (4.16)$$

C_{VM} is the virtual mass coefficient, which corresponds to the volume fraction of liquid which is accelerated with the bubble. For a generic void fraction and writing the actual relative acceleration, equation 4.16 becomes:

$$\vec{F}_{VM} = C_{VM} \rho_c \alpha \left(\frac{D\vec{U}_{dp}}{Dt} - \frac{D\vec{U}_c}{Dt} \right) \quad (4.17)$$

The turbulence transfer from dispersed to continuous phase have been investigated in literature, and nowadays different models exist which allow to estimate turbulence transfer from, for example, bubbles to the continuous liquid phase. However, they have been validated for specific two-phase flows. In the present work, no more detail will be given on interfacial turbulence transfer since, as it will be detailed in paragraph 4.1.4, a mixture turbulence model is employed for the two-phase flow studied.

4.1.4 Interfacial friction and heat transfer for underexpanded gas-into-liquid jets

Following considerations in paragraph 4.1.1, droplet and bubbly flows coexist in the two-phase flow considered. In the following equations and considerations, the volume fraction α will always refer to the gas phase volume fraction (or void fraction). The approach used in the SIMMER-III [42][43] computational code has been adopted in the present work: droplet flow is assumed for void fractions higher than a defined value α_d , bubbly flow is assumed for void fractions lower

than a defined value α_b and a transition flow is defined by combining the two regions. For the simulation of stratified vapor-liquid flow and free-surface flows, the limits $\alpha_d = 0.7$ and $\alpha_b = 0.3$ have demonstrated good results [44, 45]. Visual observations described in paragraph 4.1.1 showed that, in the two-phase jet flow considered, gas atomization occurs for volume fractions certainly higher than 30%. Moreover, well defined continuous gas phase can be observed only in the very high volume fraction region near the gas injection nozzle. Thus, a translation of α_d and α_b towards higher values is suggested. Good results have been obtained by Uchibori et al. [29] for the numerical simulation of supersonic gas-into-liquid jets, using the regime flow limits $\alpha_d = 0.95$ and $\alpha_b = 0.50$.

For the present study, results for several combinations of α_d and α_b have been investigated. Their proper calibration is then realized through the comparison of numerical with experimental results, obtained with the experimental device detailed in chapter 3.2. The best agreement with experimental results has been obtained for $\alpha_d = 0.80$ and $\alpha_b = 0.50$. 0.50 may appear as a too high limit value for bubbly flow: nevertheless, besides the high packing conditions of gas atomization visible in picture 4.4, high void fraction bubbly flow have been obtained in literature, for example by Garnier et al. [46], who investigated bubbly flow for void fractions up to 0.40. Furthermore, two-phase regime maps assuming high void fraction bubbly flow exist and are used, for example, in system codes. In the RELAP5-3D[®] [30], bubbly-to-slug transition void fraction varies from 0.25 to 0.5 depending on the mass flux, based on the work of Taitel et al. [47], who argued that the void fraction for bubbly flow could be at most 0.52, where adjacent bubbles in a cubic lattice would just touch. They then postulated that 0.52 represents the maximum attainable void fraction for bubbly flow, assuming the presence of vigorous turbulent diffusion.

In order to employ the SIMMER approach and representing mist flow, bubbly flow and regime transition, two separated drag force equations have been written depending on which flow regime characterizes the computational cell considered:

$$\vec{F}_{D,l} = -\vec{F}_{D,g} = \begin{cases} \frac{3}{4} \frac{(1-\alpha)}{d_d} C_{D,d} \rho_g |\vec{U}_g - \vec{U}_l| (\vec{U}_g - \vec{U}_l) & \text{if } \alpha \geq \alpha_d : \\ \frac{3}{4} \frac{\alpha}{d_b} C_{D,b} \rho_l |\vec{U}_g - \vec{U}_l| (\vec{U}_g - \vec{U}_l) & \text{if } \alpha \leq \alpha_b : \end{cases} \quad (4.18)$$

In equations (4.18), subscript g and l stand for gas and liquid phase, respectively. In the transition flow regime between α_b and α_d , the drag law is continuously interpolated between droplet and bubble drag laws, using a logarithmic weighted average, in order to obtain the transition drag force $F_{D,t}$. Equations 4.19 to 4.23 are used to calculate $F_{D,t}$.

$$\alpha^* = \max[\alpha_b, \min(\alpha, \alpha_d)] \quad (4.19)$$

$$x_b = \frac{\alpha_d - \alpha^*}{\alpha_d - \alpha_b}; \quad x_d = \frac{\alpha^* - \alpha_b}{\alpha_d - \alpha_b} \quad (4.20)$$

$$\vec{f}_{D,b} = \frac{3}{4} \frac{\alpha_b}{d_b} C_{D,b} \rho_l \left| \vec{U}_g - \vec{U}_l \right| \left(\vec{U}_g - \vec{U}_l \right) \quad (4.21)$$

$$\vec{f}_{D,d} = \frac{3}{4} \frac{(1 - \alpha_d)}{d_d} C_{D,d} \rho_g \left| \vec{U}_g - \vec{U}_l \right| \left(\vec{U}_g - \vec{U}_l \right) \quad (4.22)$$

$$\vec{F}_{D,t} = \exp \left[x_b \cdot \log \left(\vec{f}_{D,b} \right) + x_d \cdot \log \left(\vec{f}_{D,d} \right) \right] \quad (4.23)$$

Therefore, $F_{D,t}$ is the drag force exerted by the gas to the liquid phase.

For the determination of droplet diameter, the useful literature results obtained by M. Epstein [21] and Kudoh [22] have been employed. As already detailed in paragraph 2.1, Epstein established a correlation for the determination of the droplet SMD d_d for the liquid entrainment caused by N₂-into-water underexpanded jets. The results are a function of gas injection pressure and nozzle injection diameter: for gas injection pressure ranging between 0.2 and 1.5 MPa and a nozzle diameter ranging from 1.0 to 2.0 mm, entrained droplet SMD was found to range between 10 and 50 μm . Kudoh investigated Argon-into-liquid-sodium jets and validated Epstein's correlation for entrained sodium droplet diameter. Epstein's correlation is the following:

$$SMD = 0.39 \cdot d_0 \left[\frac{\sigma}{u_0^2 \rho_\infty d_0} \right]^{0.4} \quad (4.24)$$

Where d_0 is the nozzle diameter, u_0 is the depressurized jet velocity (meaning the gas velocity at the end of the underexpansion), σ is the surface tension and ρ_∞ is the density of the depressurized gas jet. The velocity u_0 to be used in (4.24) is obtained through conservation of momentum flux between the choke conditions at nozzle exit and underexpanded conditions:

$$u_0 = \frac{G}{\rho^*} + \frac{P^* - P_\infty}{G}$$

Where the superscript * stands for choke condition, G is the orifice mass flux and P_∞ is downstream ambient pressure.

Droplet drag coefficient $C_{D,d}$ has been estimated following the results obtained by Walsh [48], who investigated particle drag coefficient in high speed gas flow: $C_{D,d}$ is a function of droplet Reynolds number and gas Mach number. The following correlation has been obtained by Walsh:

$$C_{D,d} = C_{D,C} + (C_{D,FM} - C_{D,C}) \exp \left[-A \cdot (Re_d)^N \right] \quad (4.25)$$

The constants $C_{D,C}$, $C_{D,FM}$, A and N are function of gas Mach number. In the present work, the values of constants for a Mach equal to one have been

employed for the estimation of the droplet drag coefficient. Re_d is the droplet Reynolds number, calculated with the droplet velocity relative to continuous gas phase:

$$Re_d = \frac{\rho_g \cdot \Delta \vec{U}_{dg} \cdot d_d}{\mu_g} \quad (4.26)$$

Where μ_g is the gas dynamic viscosity and ΔU_{dg} is the absolute droplet-to-gas relative velocity.

No available data regarding bubble dimension for high velocity gas-into-liquid jets has been found in literature. Therefore, bubble SMD d_b has been estimated following critical Weber number parameter: the Weber number (We) is the ratio between the inertial force and the surface tension force for a particle:

$$We = \frac{\rho_c \cdot \Delta \vec{U}^2 \cdot d}{\sigma} \quad (4.27)$$

In the case of a bubble, d in equation (4.27) corresponds to the bubble diameter d_b . When the Weber number reaches a certain high value, inertial force becomes too important compared to surface tension force, and particle break-up occurs. The Weber number at which break-up occurs is called critical Weber number (We_c): this parameter is often employed to estimate particle average dimension in a specific two-phase flow, meaning the maximum possible particle dimension before break-up. In RELAP5-3D[®], $We_c = 10$ is employed for estimating bubble diameter in bubbly flow.

Bubbles, in the considered bubbly flow, are of small dimensions (around $4 \cdot 10^{-4}$ m, as it will be detailed in paragraph 4.2): therefore, they will be considered spherical. Bubble drag coefficient $C_{D,b}$ has been estimated from Schiller and Naumann correlation [49]. However, a correction to this single bubble flow correlation must be applied, since several studies [50, 51] showed how drag coefficient increases in case of bubble swarms, compared to single bubble flow. In the present work, the correlation obtained by Rogair [51] has been adopted:

$$\frac{C_D}{C_{D,\infty}} = (1 + 8.372\alpha)(1 - \alpha) \quad (4.28)$$

Equation 4.28 has been obtained for a bubble Eotvos number ($Eo = \frac{\Delta \rho \cdot g \cdot d_b^2}{\sigma}$) of 2.15: as a first estimation, it is assumed that this correlation could be valid also for Eotvos numbers typical of the bubbly flow considered in this work, which result to be lower than 2.15. $C_{D,\infty}$ stands for the drag coefficient for a single bubble.

In several two-phase modeling studies through two-fluid approach, lift and virtual mass forces are neglected. For example, in none of the two-fluid models for two-phase jets described in paragraph 2.1, lift and virtual mass forces have been included. On the one hand, every phase interaction phenomenon added to the model leads to higher computation effort and numerical complication.

On the other hand, interfacial forces must be properly estimated in order to obtain consistent results.

Virtual mass force for a single particle, equation 4.16, is normally replaced by the following equation, valid from a general bubble void fraction α in bubbly flows:

$$\vec{F}_{VM,l} = -\vec{F}_{VM,g} = C_{VM} \cdot \alpha \cdot \rho_l \left(\frac{D\vec{U}_l}{Dt} - \frac{D\vec{U}_g}{Dt} \right) \quad (4.29)$$

Besides the complicate task of determining a consistent value of the virtual mass coefficient, one can see that this equation is not directly applicable for the two-fluid model approach employed in this work: since droplet and bubbly flow coexist in an underexpanded gas-into-liquid jet, virtual mass should be applied either to droplets or to bubbles, depending on which two-phase regime is present in actual cell of the computational domain. This would require to implement an approach similar to the one employed for the drag force calculation (equations 4.18).

Regarding lift force, the same statements discussed for the virtual mass force can be repeated: the difficulty lies in the determination of the lift coefficient and in the fact that equation 4.15 should be differently written depending on the regime flow considered.

One further complication, concerning the use of lift and virtual mass force in a two-fluid model, is the numerical instabilities that these terms add to the solving method, which is widely reported in literature.

Following these considerations, lift and virtual mass forces are not taken into account in the present work, in order not to introduce further complications inside the two-fluid model, which is already numerically critical. In fact, several challenging aspects have to be taken into account when dealing with underexpanded gas-into-liquid flows and their numerical modeling. As previously discussed, gas velocities are much higher than typical gas rising velocity present in others two-phase flow regimes obtained, for example, in bubble columns or in ducts, broadly studied in the past. Therefore, besides the critical issue of finding proper closure laws for the interfacial exchanges, the important compressibility effects and the high Mach numbers in the gas phase are critical for the numerical stability of pressure-velocity coupling algorithms for a two-fluid approach, and poor literature can be found dealing with this kind of two-phase flows properly treated numerically, as one can see from paragraph 2.1.2. For the specific present case of a reactive jet, an additional complication is represented by the presence of an heterogeneous chemical reaction, which takes places at the gas-liquid interface, leading to the continuous consumption of one phase and creation of the other, following the reaction stoichiometry.

Before ending the discussion on the interfacial exchange, the interfacial heat transfer coefficient must be considered. As for drag force calculation, also heat transfer coefficient has been estimated differently depending on regime flows. Nusselt number has been calculated following Ranz and Marshall correlation [52]:

$$Nu = \begin{cases} = \frac{hd_d}{\lambda_g} = 2 + 0.6Re_d^{0.5}Pr_d^{0.33} & \text{if } \alpha \geq \alpha_d \\ = \frac{hd_b}{\lambda_l} = 2 + 0.6Re_b^{0.5}Pr_b^{0.33} & \text{if } \alpha \leq \alpha_b \end{cases} \quad (4.30)$$

Where Re_d , Re_b , Pr_d , Pr_b are Reynolds and Prandtl number of droplet and bubble, respectively, λ_g and λ_l are the thermal conductivity of gas and liquid, respectively, and h is the heat transfer coefficient. The interfacial heat transfer flux per unit volume is calculated with equation (4.31):

$$Q_{gl} = -Q_{lg} = a \cdot h \cdot \Delta T_{gl} \quad (4.31)$$

The product $a \cdot h$ in equation (4.31) has been evaluated assuming droplet flow for $\alpha \geq \alpha_d$, bubbly flow for $\alpha \leq \alpha_b$, and using a weighted logarithmic average for the transition flow.

4.1.5 Turbulence modeling

Navier-Stokes equations written in (4.2) or (4.8) are valid for laminar flows. In a turbulent regime, the flow behavior becomes random and chaotic, with velocity and all other flow properties varying in random and chaotic way. The random nature of a turbulent flow precludes computations based on a complete description of the motion of all fluid particles. Instead, the velocity and pressure can be decomposed into a steady mean value and a fluctuating component:

$$u(t) = U + u'(t) \quad (4.32)$$

$$p(t) = P + p'(t) \quad (4.33)$$

Equations for the mean flow in a turbulent regime can be obtained by replacing equations 4.32 and 4.33 into the instantaneous continuity and Navier-Stokes equations, and then applying a time average. We consider the Navier-Stokes equation 4.8 of the phase p in an Euler-Euler approach. By applying equations 4.32 and 4.33 and time averaging, one obtains the following equation:

$$\begin{aligned} \frac{\partial}{\partial t} \left(\alpha_p \rho_p \vec{U}_p \right) + \nabla \cdot \left(\alpha_p \rho_p \vec{U}_p \vec{U}_p \right) &= -\alpha_p \nabla P + \\ \nabla \cdot \left(\alpha_p \mu_p \left(\nabla \vec{U}_p + \left(\nabla \vec{U}_p \right)^T \right) \right) - \nabla \cdot \left(\overline{\rho \vec{u}'_p \vec{u}'_p} \right) + & \quad (4.34) \\ \alpha_p \rho_p \vec{g} + S_p^{\vec{U}} + \vec{F}_{pq} & \end{aligned}$$

Equation 4.34 is the same as 4.8, with the addition of the *RHS* term $\nabla \cdot \left(\overline{\rho \vec{u}'_p \vec{u}'_p} \right)$. This term involves products of fluctuating velocities and constitutive convective momentum transfer due to the velocity fluctuations. These extra stresses are the turbulent stresses, also referred as Reynolds stresses.

For deriving the instantaneous laminar Navier-Stokes equations, the assumption of Newtonian fluid is taken: for a Newtonian fluid, the viscous stresses are proportional to the rates of deformation. Following this assumption, the viscous stress tensor $\bar{\bar{\tau}}$ is calculated as:

$$\bar{\bar{\tau}} = \mu (\nabla \vec{u} + \nabla \vec{u}^T) \quad (4.35)$$

In order to evaluate the Reynolds stresses, the presumption is made that there exists an analogy between the action of viscous and Reynolds stresses. In 1877, Boussinesq proposed that Reynolds stresses could be linked to the mean rates of deformation. In the Boussinesq hypothesis, the Reynolds stress tensor $\bar{\bar{\tau}}_R$ is calculated as:

$$\bar{\bar{\tau}}_R = -\rho \overline{u'_p u'_p} = \mu_t (\nabla \vec{U} + \nabla \vec{U}^T) \quad (4.36)$$

Where the turbulent viscosity μ_t appears. Adopting this definition of Reynolds stresses, the turbulent time-averaged Navier-Stokes equation for the phase p can be re-written in the following form:

$$\begin{aligned} \frac{\partial}{\partial t} (\alpha_p \rho_p \vec{U}_p) + \nabla \cdot (\alpha_p \rho_p \vec{U}_p \vec{U}_p) = & -\alpha_p \nabla P + \\ \nabla \cdot (\alpha_p (\mu + \mu_t) (\nabla \vec{U}_p + (\nabla \vec{U}_p)^T)) + & \\ \alpha_p \rho_p \vec{g} + S_p^{\vec{U}} + \vec{F}_{pq} & \end{aligned} \quad (4.37)$$

Equation 4.37 is referred to as the *Reynolds Averaged Navier Stokes* equation, usually called simply RANS equation. In order to solve RANS equations, a model must be adopted which calculates the value of the turbulent viscosity. Several turbulence models have been developed for this scope. Their detailed description is not the aim of the present work. The two-equations turbulence models are by far the more frequently adopted, and this approach will be employed also in the present study: in this approach, one transport equation is solved for the turbulent kinetic energy k , and another transport equation is solved for the dissipation rate of turbulent kinetic energy ε (or for the specific dissipation rate $\omega = \frac{\varepsilon}{k}$, depending on the specific two-equations turbulence model). The turbulent kinetic energy and its dissipation rate, whose dimensions are, respectively, m^2/s^2 and m^2/s^3 , are defined as:

$$k = \frac{1}{2} (\overline{u'^2})$$

$$\varepsilon = \frac{1}{2} \frac{\mu}{\rho} [(\nabla \vec{u}' + \nabla \vec{u}'^T)^2]$$

The turbulent viscosity μ_t , whose dimensions are $kg/(m \cdot s)$, can be expressed as the product of a turbulent velocity scale θ and a turbulent length scale l :

$\mu_t = C\rho\theta l$, where C is a dimensionless constant of proportionality. Using k and ε to define the turbulent velocity and length scales, one obtains: $\theta = k^{\frac{1}{2}}$ and $l = \frac{k^{\frac{3}{2}}}{\varepsilon}$. Therefore, the turbulent viscosity is defined as:

$$\mu_t = C\rho\frac{k^2}{\varepsilon}$$

When a turbulence model is added to an Euler-Euler approach for a two-phase flow, turbulence can be solved separately for each phase or considering the turbulence of the global gas-liquid mixture: in the first case, two dedicated sets of k and ε equations are solved for each phase leading to a total of four equations (actually, turbulence can also be considered only in one phase, as it is often assumed for bubbly flows, where gas is considered laminar and liquid turbulent [53, 54]: in this case, only two equations for k and ε are solved); in the second case, a single set of k and ε equations is solved for the gas-liquid mixture, leading to a total of two equations. When a phase-dedicated turbulence model is adopted, closure laws must be known in order to determine the interfacial turbulent momentum transfer. Most of models for interfacial turbulence transfer existing in literature have been developed for bubble induced turbulence to the liquid phase, for bubbly flow with low void fractions [53, 54]. Applying a phase-dedicated turbulence model for a gas-into-liquid jet flow is a complicated task, due to the necessity of determination of proper interfacial turbulence and turbulent momentum transfer. In recent studies in bubbly flow [46], it was found that for void fraction higher than a value around 10%, the ratio between liquid and gas rms velocity fluctuations is close to one. This implies that both phases tend to fluctuate as one entity at relatively high gas fraction and suggests that the use of one set of equation for the turbulent energy and the turbulent energy dissipation rate for the mixture of the continuous and the dispersed phases is appropriated: since the present studied two-phase flow is characterized by high void fractions and even packing conditions, a standard k - ε mixture turbulence model has been adopted for the closure of Reynolds stress tensor. The two equations solved by the model are the following:

$$\frac{\partial}{\partial t}(\rho_m k) + \nabla \cdot (\rho_m k \vec{U}_m) = \nabla \cdot \left(\frac{\mu_t}{\sigma_k} \nabla k \right) + 2\mu_t S_{ij} S_{ij} - \rho_m \varepsilon - Y_C \quad (4.38)$$

$$\begin{aligned} \frac{\partial}{\partial t}(\rho_m \varepsilon) + \nabla \cdot (\rho_m \varepsilon \vec{U}_m) = \\ \nabla \cdot \left(\frac{\mu_t}{\sigma_\varepsilon} \nabla \varepsilon \right) + \frac{\varepsilon}{k} (C_{1,\varepsilon} \cdot 2\mu_t S_{ij} S_{ij} - C_{2,\varepsilon} \rho_m \varepsilon) \end{aligned} \quad (4.39)$$

Where the mixture density and mixture velocity are, respectively:

$$\rho_m = \sum_p \alpha_p \rho_p \quad (4.40)$$

$$\vec{U}_m = \frac{\sum_p \alpha_p \rho_p \vec{U}_p}{\sum_p \alpha_p \rho_p} \quad (4.41)$$

In equations (4.38) and (4.39), S_{ij} is the mean rate of strain tensor:

$$S_{ij} = \frac{1}{2} \left(\frac{\partial U_{m,i}}{\partial x_j} + \frac{\partial U_{m,j}}{\partial x_i} \right) \quad (4.42)$$

Turbulent viscosity μ_t is calculated through equation (4.43):

$$\mu_t = \rho_m C_\mu \frac{k^2}{\varepsilon} \quad (4.43)$$

The model constants $C_{1,\varepsilon}$, $C_{2,\varepsilon}$, C_μ , σ_k and σ_ε have the same value as in the standard $k - \varepsilon$ model [55].

Current turbulence models have been designed for low-speed, isothermal flows. Future research should strive to develop a new model that is general for all types of flows. However, at this time, the practical approach is to modify existing models for more complicated flows. The compressibility correction is devised to deal with additional effects seen for higher Mach number flows, specifically, the effects of compressibility on the dissipation rate of the turbulence kinetic energy. For free shear flows, this is exhibited as the decrease in growth rate in the mixing layer with increasing Mach number [56]. Standard turbulence models do not account for this Mach number dependence, and thus a compressibility correction is used. For compressible flows, two extra terms, known as the dilatation-dissipation and the pressure-dilatation, occur in the turbulence kinetic energy equation. The pressure-dilatation term is usually neglected because its contributions have been shown to be small [57]. The dilatation dissipation term is included in addition to the incompressible dissipation. Sarkar [58] modeled the ratio of the dilatation dissipation to the incompressible dissipation as a function of the turbulence Mach number, M_t , defined as:

$$M_t = \frac{\sqrt{k}}{a} \quad (4.44)$$

Where a is the speed of sound. The dissipation term proposed by Sarkar, to be added to the turbulent energy transport equation, is:

$$Y_C = 2\rho\varepsilon M_t^2 \quad (4.45)$$

In the present two-phase mixture $k - \varepsilon$ model, equation 4.45 becomes:

$$Y_C = 2\rho_m \varepsilon M_t^2 \quad (4.46)$$

The influence of turbulence in the Navier-Stokes equations is represented by a new viscosity, μ_t . Since transport of momentum and heat is due to the same mechanism, a turbulent conductivity, λ_t , is defined:

$$\lambda_t = \frac{c_p \mu_t}{Pr_t}$$

Where Pr_t is the turbulent Prandtl number, which is commonly taken equal to 0.85. It follows that energy equation 4.9, for a turbulent flow, must be rewritten as:

$$\begin{aligned} \frac{\partial}{\partial t} (\alpha_p \rho_p h_p) + \nabla \cdot (\alpha_p \rho_p \vec{U}_p h_p) = -\alpha_p \frac{\partial P}{\partial t} + \\ \nabla \cdot (\alpha_p (\lambda + \lambda_t) \nabla T_p) + Q_{pq} + S_p^H \end{aligned} \quad (4.47)$$

4.2 Results and validation

The commercial CFD package Ansys Fluent 14 has been employed for the discretization and solution of the model equations inside the computational domain. For Eulerian multiphase calculations, Fluent uses the Phase Coupled SIMPLE (PC-SIMPLE) algorithm developed by Vasquez and Ivanov [59] for the pressure-velocity coupling. PC-SIMPLE is an extension of the SIMPLE algorithm developed by Patankar [60] to multiphase flow. The velocity solutions are coupled by phases, but in a segregated fashion. One difference of the PC-SIMPLE algorithm from the SIMPLE algorithm lies in the existence of interfacial coupling terms in the conservation equations. The coupled solver uses a block algebraic multigrid scheme to solve a vector equation formed by the velocity components of all phases simultaneously. Then, a pressure correction equation is built based on the conservation of the total volume. Pressures and velocities are then corrected to satisfy the continuity constraint. The pressure gradients are evaluated adopting a scheme analogous to the one proposed by Rhie and Chow [61], in order to avoid pressure checker-boarding when using a non-staggered grid (as it is the one adopted in Fluent).

The SIMPLE is a guess-and-correct procedure. To initiate the process, pressure and velocity fields are guessed. A correction p' as the difference between the correct pressure field p and the guessed pressure field p^* can be defined as $p = p^* + p'$. Similarly to the pressure, the velocity corrections can be also defined. At this point, using at the same time the momentum and continuity equations, the so-called pressure correction equation can be found: by solving this equation, the pressure correction field p' can be obtained. Once the pressure correction is known, the correct pressure field is obtained. Using the momentum equations and the definition of the corrected velocity fields ($u = u^* + u'$, $v = v^* + v'$, $w = w^* + w'$), the equations for the velocity corrections are obtained, which depend on the pressure correction field p' and corrected velocities can, therefore, be evaluated. The corrected pressure and velocity fields are used as starting values for a new iteration of the algorithm, and the iterative procedure stops when the desired convergence is achieved.

Considering interfacial momentum and energy transfer, only the most common drag force models are available in the as-built version of Fluent; moreover, no

two-phase regime transition models are provided. Nevertheless, the original code can be significantly customized through the utilization of the so called “User Defined Functions”, which are C language functions that can be compiled into the Fluent code in order to define customized laws for, for example, momentum, energy and mass transfer. Therefore, the approach for momentum and energy interfacial exchange described in 4.1.4 has been implemented into Ansys Fluent through User Defined Functions.

4.2.1 Computational geometry and numerical details

In order to validate the modeling approach described in paragraph 4.1, numerical simulations have been performed using a computational domain corresponding to the experimental device employed for investigating gas-into-water underexpanded jets, described in paragraph 3.2: a cylindrical pool of 100 mm diameter, and a height corresponding to the water level considered. In the center of the bottom face of the computational domain, a 1 mm diameter nozzle is placed; the nozzle length is 2 mm, corresponding to the sonic throat length of the nozzles employed in the experimental tests. The water height was fixed to 200 mm: with higher quantity of water inside the experimental pool, gas injection from the bottom pushed water to exit from the top open free surface, leading, in turn, to a variable water level during the experiments. 200 mm was observed as the maximum water height in order not to have water loss during gas injection, considering a gas pressure of 0.7 MPa, as it will be detailed further on.

The present geometry may suggest that a 2D-axisymmetrical geometry could have been adopted for the numerical modeling; however, considered the final goal of developing a numerical approach transposable to any relevant heat exchanger geometry, the choice of a complete 3D geometry was retained.

Some considerations must be discussed about the modeling approach to be employed for the nozzle. Its diameter, 1.0 mm, is very small compared to the size of the pool. The mesh minimum size cannot be dictated by the nozzle, since this would lead to a too fine mesh inside the pool, which would be critical for two reasons: first of all, in a Euler-Euler approach, the condition of cell size greater than the dispersed phase size must be guaranteed inside the entire the numerical domain; secondly, the computational time would increase significantly. For these reasons, wall functions for the boundary layer profile must be employed on the nozzle wall and the nozzle must be meshed consistently with this choice. It is known that typical wall functions for turbulent flows have been built for incompressible flows, i.e. generally for Mach lower than 0.30. Inside the nozzle here considered, gas flows at sonic conditions, meaning Mach equal to 1. The validity of a standard wall function for this highly compressible case must be verified. In order to do this, a detailed numerical study has been realized on a stand-alone model of the nozzle. The wall region was meshed with a first cell size corresponding to $y^+ = 0.20$, and radially growing with a rate of 1.2 towards the center of the nozzle. In this way, the boundary layer can be solved and the real velocity profile inside it can be obtained. The resulting mesh is shown in figure 4.7.

Ansys Fluent 14 has been employed for solving the continuity, RANS and energy equations inside the nozzle. A standard $k - \varepsilon$ turbulent model has

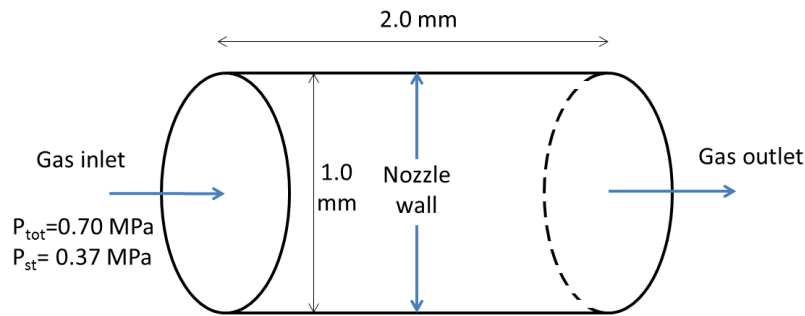


Figure 4.6: Representation of the nozzle and its boundary conditions.

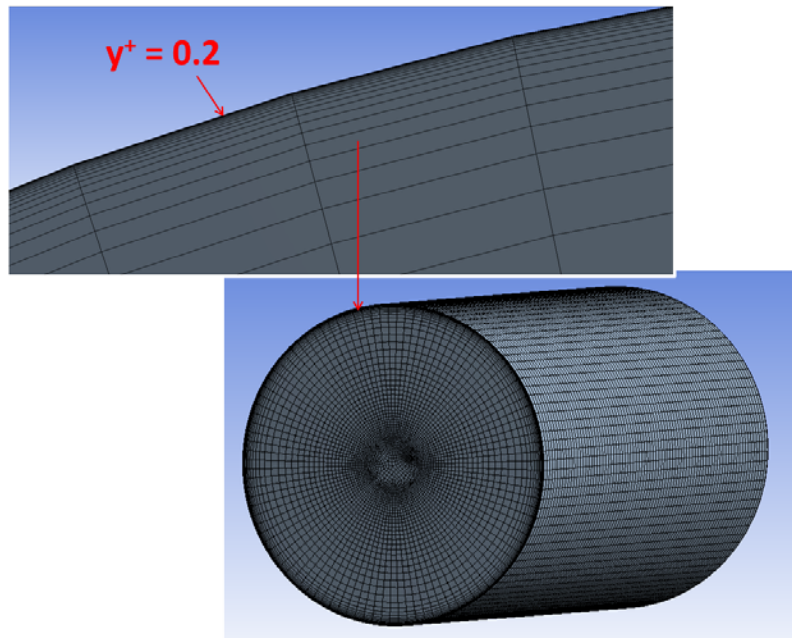


Figure 4.7: Mesh of the nozzle for boundary layer velocity profile study.

been adopted. Nitrogen gas at 0.70 MPa total pressure was employed in the simulation: at the nozzle inlet, static and total pressures, plus temperature, were fixed in order to obtain sonic conditions. At the nozzle outlet, no boundary conditions are imposed, since the pressure is extrapolated from the flow in the nozzle interior. The turbulence boundary conditions at the inlet have been evaluated as it will be described later on in this paragraph. Figure 4.6 shows a scheme of the nozzle, with the boundary conditions adopted for the numerical calculation.

A steady-state calculation has been realized. Second order upwind spatial discretization was employed for all equations. Velocity profile in the near-wall region is, normally, reported through the non-dimensional distance from the wall, y^+ , and the non-dimensional velocity, u^+ . These two variables are defined

in the following way:

$$y^+ = \frac{y \cdot \rho \cdot u^*}{\mu}$$

$$u^+ = \frac{u}{u^*}$$

Where y is the distance from the wall, u the velocity, and u^* is the friction velocity, defined as:

$$u^* = \sqrt{\frac{\rho_w}{\tau_w}}$$

Where ρ_w is the flow density on the wall and τ_w is the wall shear stress.

According to the universal law of the wall proposed by Launder and Spalding [62], for an incompressible flow, three different regions can be differentiate inside the boundary layer:

- The pure viscous sublayer, for $0 < y^+ < 5$, where $u^+ = y^+$;
- The fully turbulent region, for $y^+ > 60$, where $u^+ = \frac{1}{0.4187} \cdot \ln(y^+) + 5$;
- A buffer layer for $5 < y^+ < 60$.

Figures 4.8 and 4.9 show the calculated profile compared to the one resulting from the law of the wall. The comparison was realized at two different distances from the nozzle inlet: at the middle and at 3/4 of the length. It can be seen how the wall function reproduces quite well the calculated profile: the linear region is very well represented in the region $0 < y^+ < \sim 6$, as well as the logarithmic region, even if the calculate profile shows a logarithmic law starting from $y^+ \sim 35$, which is lower than the value suggested by the universal law of the wall. From the results found, it can be assumed that the universal law of the wall could be consistently employed also for the current case of compressible gas flow inside the nozzle. Therefore, in order to simplify the meshing and to improve numerical stability, it is chosen to place one single cell in the near wall region of the nozzle, where the universal law of the wall will be applied. In order to understand the size of the first cell near the wall, it is assumed that it should occupy the region where the condition $0 < u < 0.99 \cdot u_{free\ stream}$ is verified, where $u_{free\ stream}$ is the velocity at the center of the nozzle. From the calculated profile, it results that $u = 0.99 \cdot u_{free\ stream}$ at $y^+ \approx 230$. When employing the standard wall function, Fluent builds the velocity profile inside the boundary layer using the linear law until its intersection with the logarithmic law: starting from this point, the logarithmic law is assumed. The transition between them is not taken into account.

One further hypothesis, which is implicitly retained when employing the $k - \varepsilon$ turbulence model, is that the turbulence spectrum has achieved its equilibrium

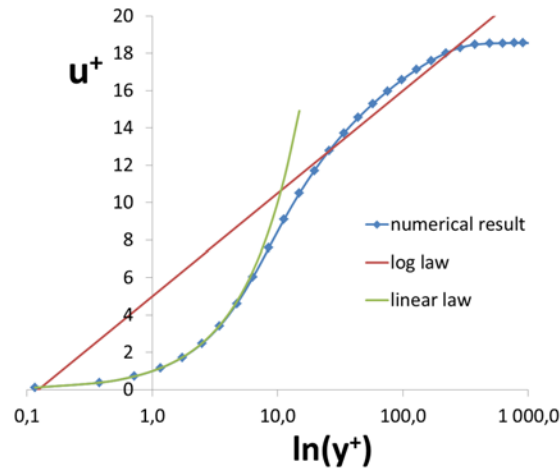


Figure 4.8: Calculated velocity profile inside the wall boundary layer compared to the universal law of the wall. Numerical results refer to an axial distance corresponding to the middle of the nozzle.

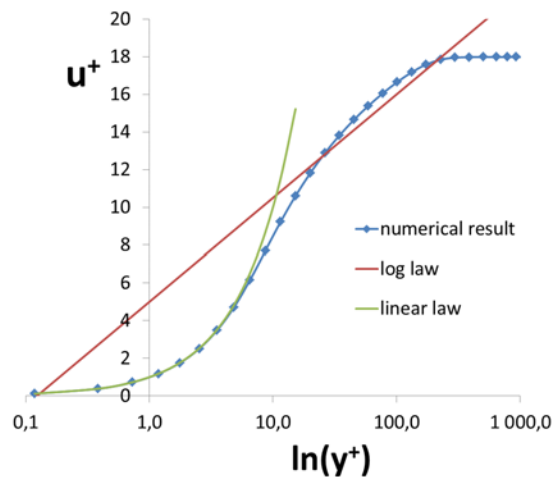


Figure 4.9: Calculated velocity profile inside the wall boundary layer compared to the universal law of the wall. Numerical results refer to an axial distance corresponding to 75% of the nozzle length from the gas inlet.

condition inside the whole nozzle. One recalls that, inside a tube, the fluid dynamic developed conditions are achieved after about 20 tube-diameter distance from the tube inlet. Considering the length of the nozzle here considered, it seems difficult to assume a developed flow at the nozzle outlet. Nevertheless, Birkby and Page [63] employed the $k - \varepsilon$ model for the CFD simulation of turbulent underexpanded gas jets, adopting turbulence boundary conditions for a developed flow, and found that the solution was relatively insensitive to the inflow turbulence conditions, with only a small reduction in potential core

length for increased turbulence intensity. In the following, an approach analogous to the one employed by Birkby and Page will be used for the definition of the turbulence inlet conditions.

Concerning the whole numerical domain comprehending the nozzle and the pool, the computational domain is filled with unstructured and tetrahedral mesh of 75,000 cells. One finer mesh will be considered later in this paragraph in order to check mesh convergence.

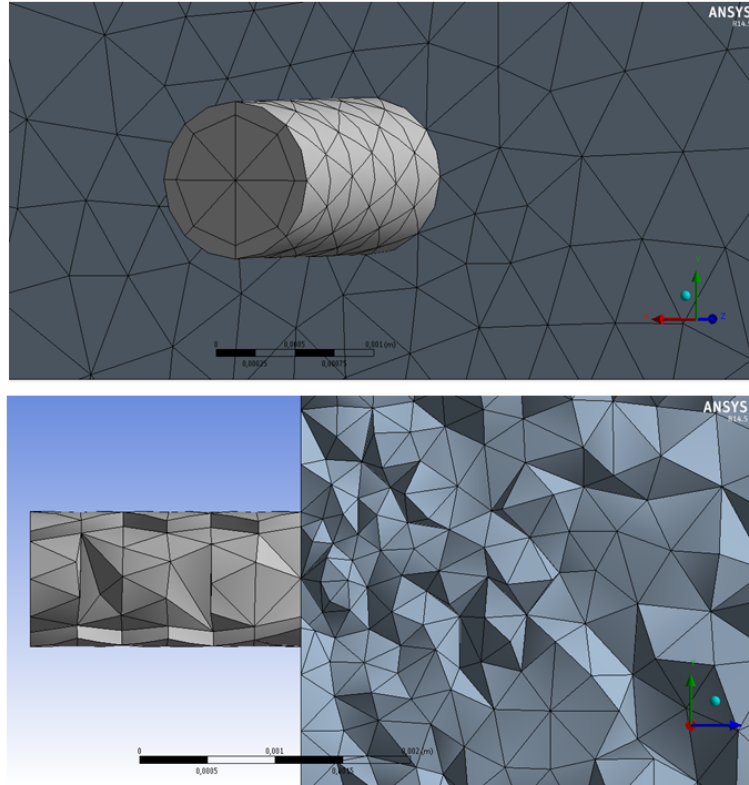


Figure 4.10: Meshing employed in the nozzle and in the region close to it.

Figure 4.10 provides some details regarding meshing inside the nozzle and in the region close to it. Implicit time discretization scheme is employed, therefore there is not stability criterion (typically, the Courant number condition) that needs to be met in determining the time-step size. Nevertheless, the precision is affected by the size of the time-step and, for the same level of precision, increasing the number of cells would lead to a decrease of time-step size. The numerical convergence of the Fluent solver has shown to be very sensitive to the meshing of the nozzle and the region of the pool very close to the nozzle. No convergence has been achieved, for example, employing hexagonal cells inside the whole numerical domain. Similarly, numerical stability has shown to decrease with the increasing of the number of cells inside the nozzle. Therefore, provided that the condition of $Mach=1$ is verified inside the nozzle (with the exception of the boundary layer region), the mesh characteristics inside it has

been chosen in order to guarantee the minimum necessary numerical stability of the solver.

At the nozzle inlet, gas mass flow rate has been fixed as boundary condition, which has been calculated using choked flow equations (4.48, 4.49, 4.50), in order to obtain sonic gas velocity at the nozzle inlet (since the nozzle acts as a sonic throat). Together with mass flow rate, temperature and pressure are required in order to evaluate the inlet velocity: therefore, in addition to the mass flow rate, Fluent requires the static pressure and the total temperature as inlet boundary conditions. Total temperature was fixed equal to 298K, whereas total pressure was fixed to 0.70 MPa. Since experimental and numerical calculations have been performed at sub-critical gas pressure values, ideal gas law (equation 4.51) was employed for the gas phase:

$$G = \rho^* \sqrt{\gamma RT^*} \quad (4.48)$$

$$P^* = P_{tot} \left(\frac{\gamma + 1}{2} \right)^{\frac{-\gamma}{\gamma - 1}} \quad (4.49)$$

$$T^* = T_{tot} \left(\frac{2}{\gamma + 1} \right) \quad (4.50)$$

$$\rho^* = P^* / RT^* \quad (4.51)$$

In equations (4.48)(4.51)(4.49)(4.50), the superscript * and *tot* stand for choked and stagnation (total) conditions, respectively, G is the mass flow flux, γ is the ratio between gas heat capacities (c_p/c_v) and R is the gas constant (divided by the gas molar mass). Water temperature and pressure were fixed to 298 K and 101325 Pa, respectively. Water was treated as incompressible, with constant density equal to 980 kg/m^3 .

The values of k and ε must be determined at the inlet, to be used as boundary conditions. The turbulent kinetic energy at the inlet is estimated through the following equation:

$$k_{in} = \frac{3}{2} (U_{mean} \cdot I)^2 \quad (4.52)$$

Where U_{mean} is the mean flow velocity at the inlet and I is the turbulence intensity at the inlet. The turbulence dissipation at the inlet is evaluated through the following equation:

$$\varepsilon_{in} = C_\mu^{\frac{3}{4}} \frac{k_{in}^{\frac{3}{2}}}{l} \quad (4.53)$$

Where l is the turbulence length scale. The turbulence intensity, which corresponds to the ratio between the velocity fluctuation and the mean velocity, and the turbulence length scale can be estimated using the following expressions, valid for fully-developed duct flow [64]:

$$I = \frac{u'}{U_{mean}} = 0.16 \cdot Re^{-\frac{1}{8}} \quad (4.54)$$

$$l = 0.07 \cdot D \quad (4.55)$$

In 4.55, the factor of 0.07 is based on the maximum value of the mixing length in fully-developed turbulent pipe flow, where D is the diameter of the pipe. The nozzle Reynolds number in the present work, for the thermodynamic conditions considered, is $9 \cdot 10^5$: using equations 4.54 and 4.55, the turbulence intensity results 4%. The values of I and l are consistent with the ones employed by Birkby and Page [63], for the numerical simulation of underexpanded gas jets, who, for Reynolds number ranging from $1 \cdot 10^6$ to $2.3 \cdot 10^6$, fixed $I = 5\%$ and l equal to 5 per cent the nozzle diameter.

All numerical simulations have been initially started using first order upwind scheme for the spatial discretization of all equations, more stable for achieving convergence during the initial unstable time steps of calculation: once the numerical calculation becomes more stable (after some time steps), the discretization scheme of equations is gradually switched from first to second order upwind for all equations but the k and ε equations, for which first order upwind was retained, since no improvement have been observed using the second order scheme. Implicit temporal scheme has been employed, with time step ranging from $1 \cdot 10^{-7}$ to $1 \cdot 10^{-6}$ seconds. The convergence criteria was fixed to a residual lower than 10^{-3} for each equation.

4.2.2 Velocity profiles

An important aspect to be taken into consideration regarding the velocity profile, is the behaviour of the gas velocity in the underexpansion region. Starting from sonic conditions, gas velocity is supposed to increase at the nozzle outlet due to underexpansion: this phenomenon is properly represented by the numerical model, as shown in figure 4.11, where supersonic gas velocity can be seen downstream the nozzle. Figure 4.11 shows that gas velocity exactly at the nozzle exit (axial distance equal to zero) is higher than the sonic value: this is due to the fact that underexpansion begins already inside the last part of the nozzle. This can be observed also in the following figure 4.14, reporting the pressure profile, which show how pressure starts to decrease already inside the nozzle.

Velocity profiles inside the two-phase jet in the pool are important in order to obtain information regarding slip velocity between phases, which is, in turn, needed to estimate the Sauter bubble diameter through the critical Weber number. A first attempt must be made in order to obtain a bubble size for a first simulation. Assuming critical Weber number of 10, as suggested by the

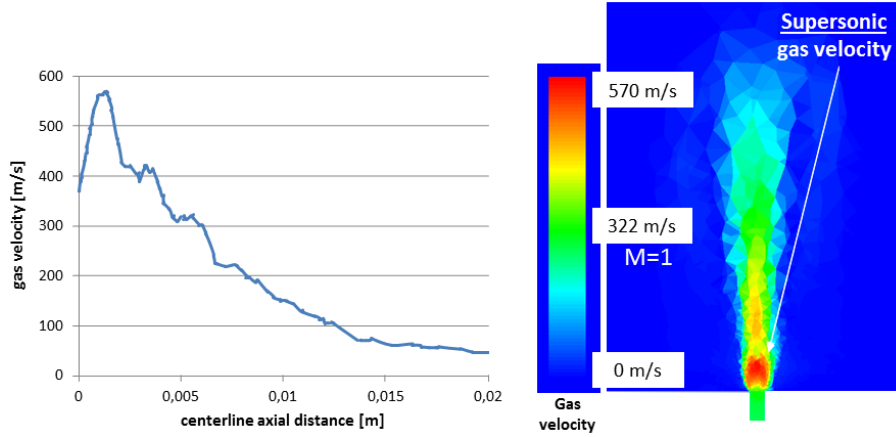


Figure 4.11: Gas velocity profile in region close to the nozzle.

RELAP5-3D code [30], and a slip velocity of 1 m/sec, bubble diameter would result being 0.2 mm. Droplet diameter is estimated through equation 4.24 which does not require slip velocity, depending only on injection pressure: for 0.7 MPa, estimated droplet diameter is 20 μm .

Results shown in figure 4.12 have been obtained with $\alpha_d = 0.80$ and $\alpha_b = 0.50$: one can see that, after around 25 mm, slip velocity decreases below 1 m/sec. Since, as it will be shown in paragraph 4.2.4 (figure 4.16), void fraction is still much higher than α_b in this zone, this means that bubble diameter should be estimated using a slip velocity lower than 1 m/sec. Looking at figure 4.16, gas void fraction starts to significantly decrease at an axial distance of around 100 mm. The region where gas core breaks up and bubbles are formed should lie in this zone: slip velocity calculated numerically at 100 mm from the nozzle is around 0.05 m/sec. Using this velocity to estimate bubble diameter, assuming a critical Weber number of 10, would result to a very large bubble diameter, clearly unrealistic when compared to the visual observation shown in figure 4.4, which show how gas atomization is formed by very small bubbles. Even using the critical Weber number of 1.2 obtained by Hinze [65], the resulting bubble diameter would be larger than 3 cm, which is still unrealistic considering experimental results. In order to have a maximum stable bubble diameter of some millimeters, which seems to be the order of magnitude of bubble diameters observed in the experimental tests, absolute slip velocity should lie between 0.15 and 0.2 m/s, corresponding to 3.8 and 2.1 mm diameter, respectively. These results suggest that the Weber number, as defined in equation 4.27, is not the proper parameter to be employed.

Kolmogorov [66] and Hinze [65] developed a theory for bubble or drop breakup in turbulent flows: they suggested that a bubble breaks as a result of interactions with turbulent eddies that are of approximately the same size as the bubble. If the turbulent field is assumed to be homogeneous and isotropic (which is an implicit assumption when employing a $k - \varepsilon$ turbulence model), Hinze and Kolmogorov showed that the appropriate velocity term in equation 4.27 is the root mean square of the velocity difference over a distance equal to the particle diameter, and its value may be approximated by:

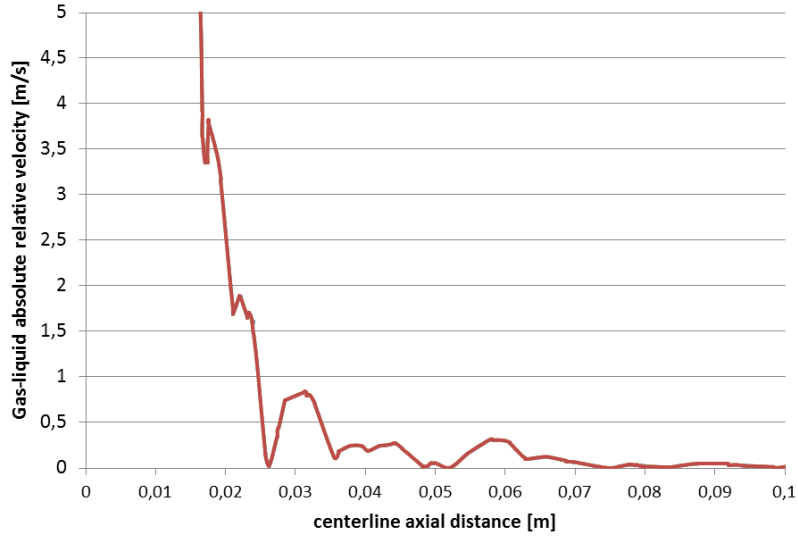


Figure 4.12: Profile of absolute gas-liquid relative velocity along the centerline.

$$\Delta U^2 = 2(\varepsilon \cdot d)^{2/3} \quad (4.56)$$

In fact, if the bubble is small compared to the length scale of the energy containing eddies (l_E) but large compared to the Kolmogorov length scale (l_K), the eddies responsible for breakup are isotropic and lie within the inertial subrange such that their kinetic energy is independent of viscosity and follows the Kolmogoroff energy distribution law. Therefore, equation 4.56 is valid as long as:

$$l_K < d < l_E$$

Substituting equation 4.56 in 4.27, one obtains the following equation for the maximum particle size:

$$d_{max} = \left(\frac{W e_c}{2} \right)^{3/5} \left(\frac{\sigma}{\rho_c} \right)^{3/5} \varepsilon^{-2/5} \quad (4.57)$$

Figure 4.13 shows the calculated turbulence dissipation rate along the jet axis, using the parameters detailed in the figure description: one can see that in the region where bubbly flow is supposed to generate, that is when the void fraction approaches 0.5 (around 120 mm downstream the nozzle, in this case), ε is about 100-150 $m^2 \cdot s^{-3}$. Using equations 4.57 and a critical Weber number of 1.2, as suggested by Hinze, the resulting maximum bubble diameter is around 0.4 mm. This value is certainly consistent with the observed experimental results.

Therefore, slip velocity is not the appropriate parameter in order to determine the maximum stable bubble diameter in the present work. In the present work, the dependence from the turbulent dissipation rate ε has been retained as the parameter influencing the bubble break-up and its maximum stable diameter: equation 4.57 is employed for the determination of the bubble diameter.

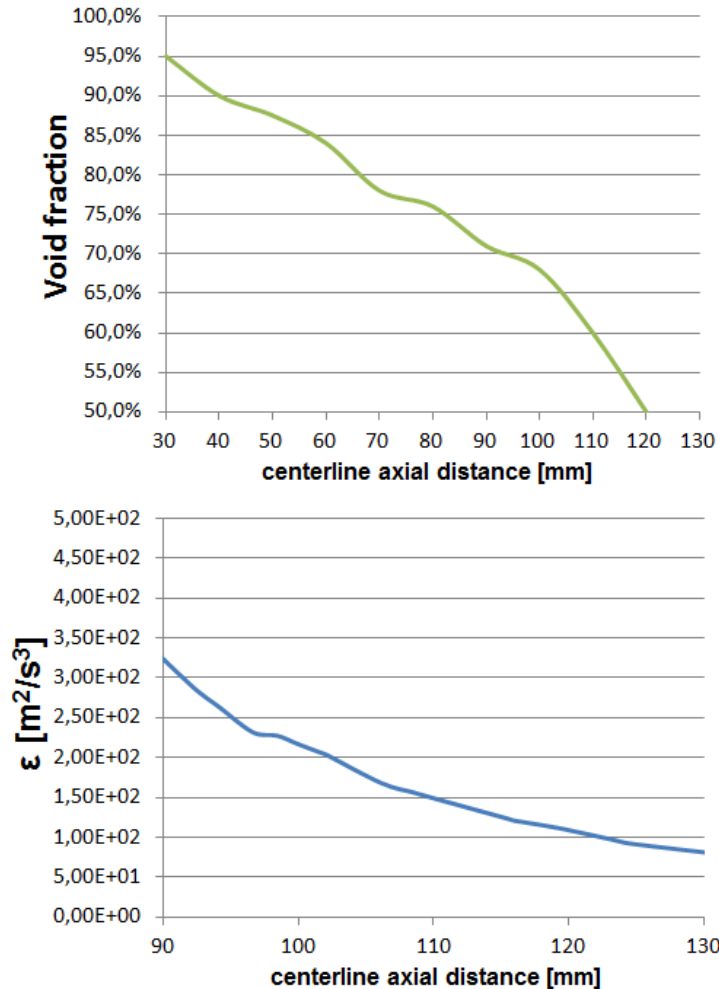


Figure 4.13: Void fraction and turbulent energy dissipation rate profiles, obtained for $\alpha_d = 0.80$, $\alpha_b = 0.50$, $d_d = 2 \cdot 10^{-5}m$, $d_b = 2 \cdot 10^{-4}m$.

4.2.3 Pressure profiles

Gas pressure profile at the nozzle outlet must be in agreement with the velocity profile shown in figure 4.11: gas pressure should decrease from the nozzle throat choked conditions due to underexpansion. Loth and Faeth measured gas pressure on the axis of an underexpanded gas-into-water jet and found a shock wave pressure behaviour. Figure 4.14 shows pressure profile on the jet

axis close to the nozzle obtained with the present model, and compared with the profile measured by Loth and Faeth [18]: even if the gas injection pressure is not exactly the same in the two studies, the calculated profile agrees with the measured one, showing a sort of expansion-compression behaviour typical of shock wave profiles. The pressure profile measured for the gas-into-gas case shows a continuous oscillation downstream the nozzle, suggesting that several shock waves occur before pressure adjusts to the ambient value. In the case of gas-into-water jet, only one significant shock wave pressure fluctuation is observed, both in the measured and the calculated profiles.

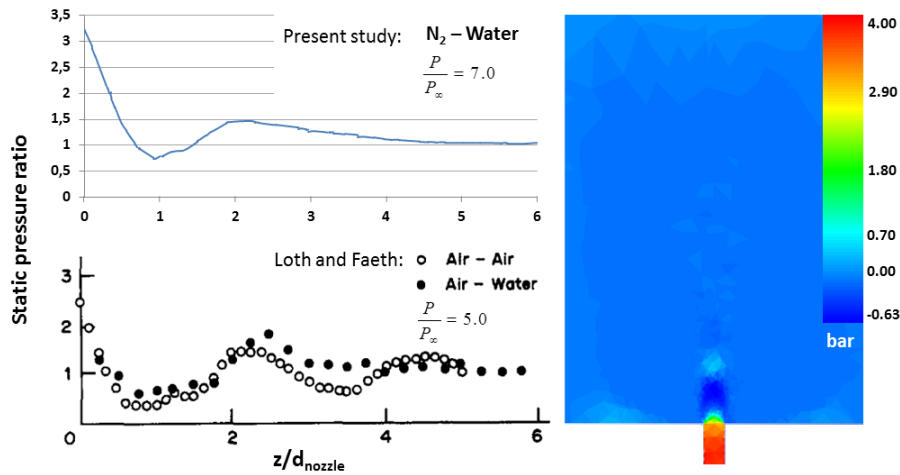


Figure 4.14: On the left: numerical and experimental results of static pressure ratio along the jet axis. On the right: contour of numerical static pressure (relative to the ambient pressure of 1.00 bar) in the region close to the nozzle.

4.2.4 Void fraction profiles

Both numerical and experimental results have been measured for conditions considered as steady state: in reality, strictly steady state conditions are never achieved, since both experimental and numerical results show that the jet is always unstable in the radial direction, featuring a sort of small swirling movement around the central axis. However, one can consider the steady state conditions achieved when the time-averaged volume fraction in different sequent time intervals does not change.

Some important considerations have to be discussed before detailing the experimental results obtained. Optical probe phase discrimination capability becomes more critical for lower contact time between the optic tip and the dispersed phase: when flow velocity increases and dispersed phase (droplet or bubble) dimension decreases, the success in discriminating the phase depends on the frequency with which the optical signal is captured by the acquisition board. Considering that the two-phase flow here investigated features very high velocities and small dispersed phase dimension, we are interested in checking the maximum phase-discrimination performances of the employed optical probe measurement system. In order to do that, the volume fraction measurements

performed on the centerline, 30 mm downstream the nozzle, is considered, since it is the most critical position investigated in terms of gas velocity: the binary signal obtained by the optical probe apparatus shows a dominant gas phase periodically interrupted by small liquid peaks; the length of these liquid peaks can be measured, and it is found that the shortest ones have a duration of $4.0 \mu\text{s}$. An example of these peaks is shown in figure 4.15.

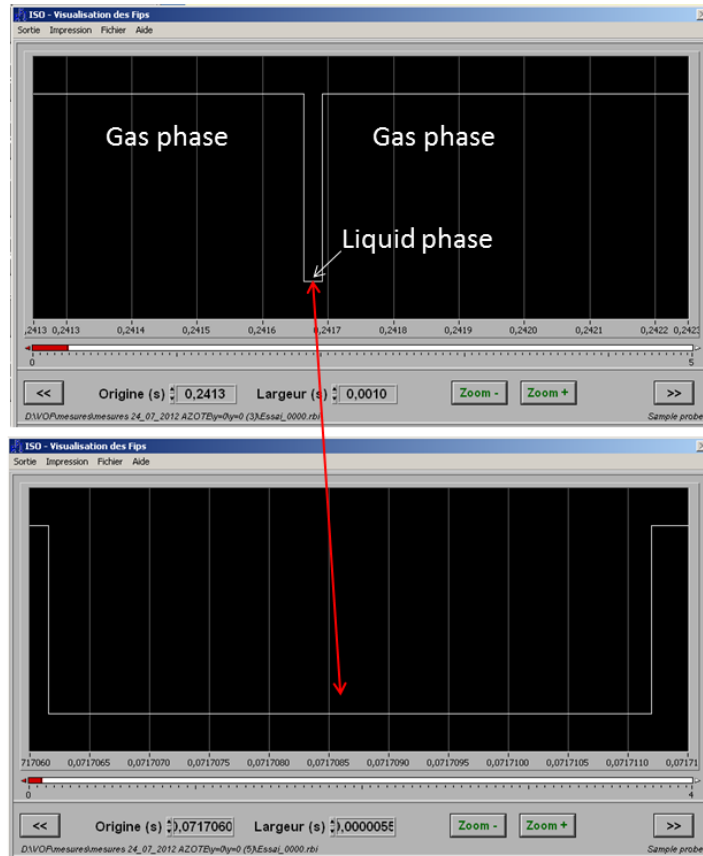


Figure 4.15: Typical TTL signal obtained during optic probe measurements at $z=30$ mm; the lower image corresponds to a zoom of the liquid phase peak shown in the upper image that, in this case, has a length of $5.5 \mu\text{s}$.

According to the numerical results, liquid velocity at 30 mm downstream the nozzle centerline is about 15 m/s, which leads to a corresponding measured particle diameter of $60 \mu\text{m}$: this must be considered as the minimum dispersed phase dimension that the apparatus is able to identify. The order of magnitude of this value is the same as the one estimated for the dispersed liquid droplet flow regime of the two-phase jet investigated: nevertheless, it has to be taken into account the fact that droplet with diameters lower than $60 \mu\text{m}$ (which are expected to exist as previously detailed in this chapter) cannot be identified by the experimental apparatus. Another aspect must be considered regarding optical probe and droplet interactions: since the optical tip diameter and the

smallest droplets dimension have the same order of magnitude, some of the latter could escape the tip instead of being pierced by it and, therefore, not be identified by the electronic device.

The void fraction profile obtained numerically is the key parameter to be checked in order to validate numerical with experimental results. The calculated void fraction depends on how the interfacial friction is determined. Following the approach detailed in paragraph 4.1.4, droplet drag coefficient and diameter, bubble drag coefficient and diameter, bubbly flow and droplet flow void fraction limits (α_d and α_b) are the variables acting on the numerical void fraction calculation. The correlation for droplet diameter in underexpanded gas-into-liquid jet has been obtained by Epstein (equation 2.1) and validated by Kudoh (figure 2.11): for this reason, droplet Sauter diameter is fixed and it is not subjected to sensitive analysis in the present work. Bubble diameter is estimated through critical Weber number, and the consistency of the value employed has been verified in paragraph 4.2.2. Droplet and bubble drag coefficients are calculated through correlations 4.25 and 4.28, obtained in flow conditions similar to the ones here considered and they are, therefore, assumed valid and no to be subjected to sensitive analysis. A sensitive analysis must be performed on bubbly flow and droplet flow void fraction transition limits, α_d and α_b .

Figure 4.16 shows axial void fraction calculated on the jet centerline, using droplet and bubble diameter of 20 μm and 0.4 mm, respectively, $\alpha_b = 0.50$ and different values of α_d , compared to the void fraction obtained experimentally. One can see how calculated void fraction, using $\alpha_d = 0.95$, decays significantly faster than the case with $\alpha_d = 0.80$, which results to be more in agreement with the experimental results. The experimental results shown are the averaged values obtained on five different experimental tests: the maximum void fraction standard deviation for the five tests is 2.8% (reported in figure 4.16): the reproducibility of the experimental measures is well verified. Numerical results are coherent with the experimental ones: the maximum difference between experimental and numerical (for $\alpha_d = 0.80$) void fraction is around 8 %. It is found that the highest experimental value of void fraction is measured at an axial distance of 40 mm and not 30 mm, as it would have been expected.

Calculating drag force using the equations 4.18, one can notice that, for the same slip velocity and a void fraction lying between α_d and α_b , bubbly flow drag force is significantly higher than the one of droplet flow. As an example, an estimation for $\alpha = 0.60$, employing the proper order of magnitude of densities and drag coefficients, leads to the following result:

$$\frac{F_{D,d} \left[\frac{N}{m^3} \right]}{F_{D,b} \left[\frac{N}{m^3} \right]} = \frac{\frac{3}{4} \frac{(1-\alpha)}{d_d} C_{D,d} \rho g}{\frac{3}{4} \frac{\alpha}{d_b} C_{D,b} \rho l} = \frac{\frac{(1-0.60)}{2 \cdot 10^{-5}} \cdot 4 \cdot 1}{\frac{0.60}{4 \cdot 10^{-4}} \cdot 1 \cdot 10^3} = 0.053$$

One can easily see that the difference between $F_{D,d}$ and $F_{D,b}$ is even higher for void fraction higher than 0.60. Remembering that drag force is parallel and opposite to the flow direction, this suggests that decreasing α_d from 0.95 to a lower value would allow the gas phase to easier penetrate into the liquid. The validity of this consideration is shown in figure 4.16: calculated void fraction

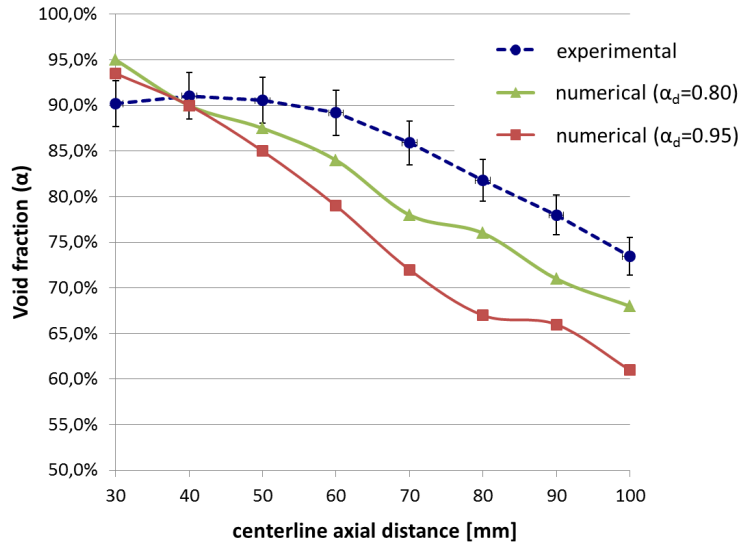


Figure 4.16: Void fraction along the jet axis for $d_d = 2 \cdot 10^{-5} m$, $d_b = 4 \cdot 10^{-4} m$, $\alpha_b = 0.5$ and two different values of α_d , as reported in figure.

for $\alpha_d = 0.80$ and $\alpha_b = 0.50$ is higher than the one obtained for $\alpha_d = 0.95$ and $\alpha_b = 0.50$.

A sensitivity analysis on the influence of bubble diameter on the void fraction profile has been also realized. Results adopting a bubble diameter of 0.2 and 0.8 mm (remembering that the retained value was 0.4 mm, as follows from consideration in 4.2.2) have been compared: no significant differences can be observed in the void fraction profiles, above all in the region within a 100 mm axial distance. We can conclude that, in the range of bubble diameters estimated in 4.2.2 ($0.2 < d_b < 0.8 mm$), void fraction profile is practically insensitive to the exact bubble diameter adopted (for the present computational domain investigated).

Looking at figure 4.16, it is interesting to verify the values of gas and liquid velocities in the region where droplet to bubbly-flow transition is supposed to occur. Considering $\alpha_d = 0.80$ and $\alpha_b = 0.50$, the transition is assumed to occur between these two limits. With reference to figure 4.16, transition would start at an axial distance of about 65 mm. Void fraction reaches 0.50 at about 120 mm from the nozzle. Figure 4.17 shows the gas and liquid absolute velocities at the centerline between 65 and 120 mm: gas and liquid velocities range between 8 and 5 m/s, with very low slip velocity. In this range of velocities, the flow map by Ishii (figure 4.2) confirms that the flow lies between the mist and the bubbly flow region.

After having looked with detail at the influence of the different main parameters of the present two-fluid approach on the calculated centerline axial void fraction profile, other spatial numerical and experimental void fraction have been investigated. Radial void fraction profiles calculated have been compared to the corresponding experimental results obtained as described in chapter 3.2.

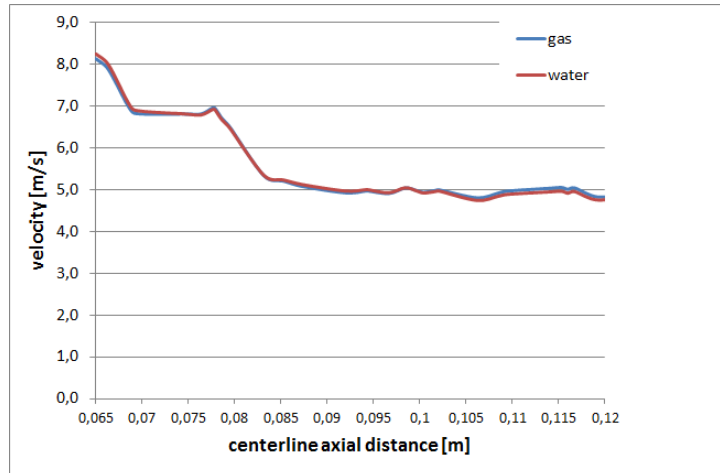


Figure 4.17: Gas and liquid absolute velocities at the axial distance where droplet to bubbly flow transition is assumed to occur ($\alpha_d = 0.80$, $\alpha_b = 0.50$, $d_d = 2 \cdot 10^{-5} m$, $d_b = 2 \cdot 10^{-4} m$).

Figure 4.18 shows numerical and experimental results obtained. For different axial positions (30, 50 and 100 mm), experimental measurements were performed varying the radial position of the optical probe from +20 to -20 mm, with sequent steps of 2 mm. The numerical model gives satisfying results: the jet width, calculated as the distance from the centerline to the point where void fraction approaches zero, is very well reproduced by the numerical model. Also the void fraction radial profile across the jet width is well reproduced by the numerical model. The radial profile at the axial distance of 100 mm is not as symmetric (both for experimental and numerical results) as for 30 and 50 mm: this could be due to the jet instability, which causes a movement around the centerline. It has to be considered that experimental radial measurement have been performed only twice for the 100 mm axial distance. Concerning the numerical results, it has to be considered that cell size is minimum closed to the nozzle and increases along the axial direction: this could lead to difficulty in representing a rigorous symmetric profile starting from a certain axial distance. Figure 4.18 also show results for a finer mesh, made of 98,000 cells, called “mesh 2”, in order to be distinguished from “mesh 1”, which represents the coarser 75,000 cell mesh: numerical results show that mesh refinement has reached convergence.

Results reported in figure 4.18 can be represented in a single plot, in order to check the self-similarity of the void fraction profiles at different axial distances. In order to that, the radial distance is normalized with respect to the axial distance, and the local void fraction is normalized with respect to the maximum void fraction at that axial distance. Figure 4.19 shows the self-similarity obtained, using the “mesh 2”. As expected, the self-similarity is lower for the radial profiles close to the nozzle, since in this region the jet is not completely developed.

Figure 4.20 shows the void fraction profile at different injection transient times.

It can be seen that, at the beginning of gas injection, a gas recirculation zone formed in the highest part of the jet is well visible both in the experimental and numerical results. Figure 4.21 shows the explanation of the presence of this gas cap: while pushing the water upward, the highest zone of the gas undergoes an inversion in flow direction, leading to tangential and counter-current velocity directions. Figure 4.20c shows a more developed transient time, with the typical expansion angle of the jet. It is interesting to check the behaviour of liquid: as shown in figure 4.21, the gas recirculation causes a liquid recirculation, which contributes to the liquid entrainment in the gas core closed to the nozzle. The transient time reported in figure 4.20 refers exclusively to the numerical results, since the experimental apparatus did not allow to evaluate the transient time of the images taken and shown in figure 4.20.

4.2.5 Final remarks

In this chapter, a numerical approach for the modeling of an underexpanded gas-into-liquid jet has been developed. The model is based on a two-fluid approach, in the frame of an Eulerian description of each phase. The type of two-phase flow found in an underexpanded gas-into-liquid jet is significantly different from the typical two-phase flow experimentally and numerically investigated in the past (such as bubbly flow or droplet flow). For this reason, a dedicated study has been performed in order to determine consistent closure laws for the interfacial friction and heat transfer. The results show consistency with the initial hypothesis retained, in terms of dispersed phase dimensions and void fraction limits for flow regime transition. Sensitivity analysis have been performed on the main parameters, in order to comprehend their influence on the final result.

In the present model, only drag force has been considered in the interfacial friction calculation. Some tests have been performed adding virtual mass effect in the interfacial friction calculation. Virtual mass has shown to cause a significant increase of computational time and an important decrease of numerical stability. Besides this, the as-built virtual mass equation employed in Fluent (equation 4.16) is taken into account only for void fractions higher than 0.40, which is consistent with the initial assumption that equation 4.16 is to be applied to bubbly flow; for higher values of void fraction, virtual mass force is set to zero. As it can be seen from equation 4.16, virtual mass applied to droplet flow would have a significantly lower importance compared to bubbly flow, since gas density is three order of magnitude lower than liquid density. Looking at the high void fraction characterizing most of the numerical domain considered, virtual mass influence may be assumed not to have a significant influence. Concerning the lift force, convergence has never been achieved, since the solver crashed as soon as the lift force was added to the calculation.

Numerical results obtained with the two-fluid model developed have been compared to the experimental ones obtained with optical probe and show that the numerical model can be used for the description of a leakage in the CO₂-sodium heat exchanger of an SFR coupled with a SCCBC. In order to account for the exothermic chemical reaction between CO₂ and sodium, a heterogeneous reaction model must be implemented and added to the present one. Therefore, the next step will concern the development of CO₂-Na chemical reaction model,

with the final goal of implementing it inside the two-fluid approach described in this chapter. The next chapter focuses on the studying on the specific reaction-diffusion phenomena, between CO_2 and sodium, occurring inside a corresponding underexpanded jet: a model will be developed, which estimates the sodium (or CO_2) reaction rate, as a function of the influencing parameters.

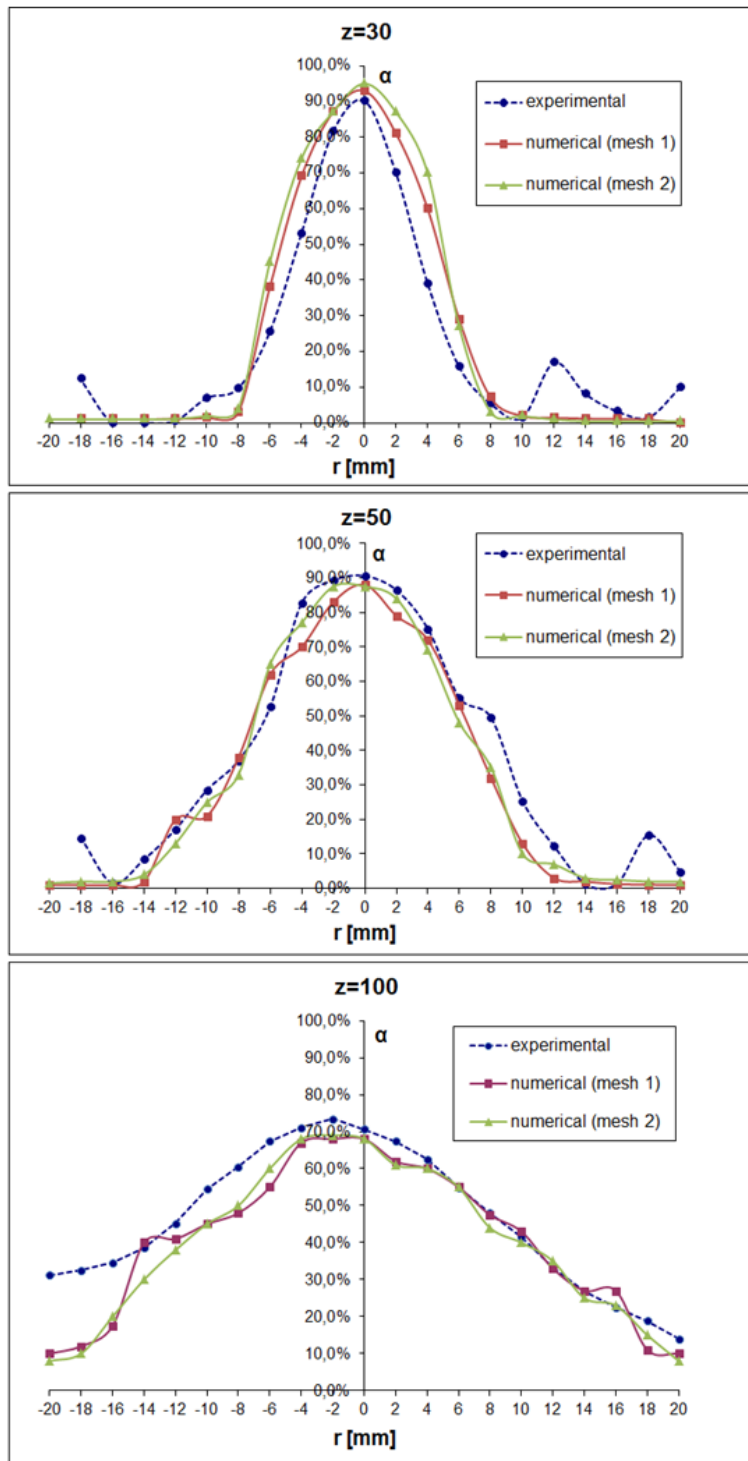


Figure 4.18: Numerical void fraction radial profiles ($\alpha_d = 0.80$, $\alpha_b = 0.50$, $d_d = 2 \cdot 10^{-5}m$, $d_b = 2 \cdot 10^{-4}m$), obtained with two different mesh sizes, compared to the experimental results.

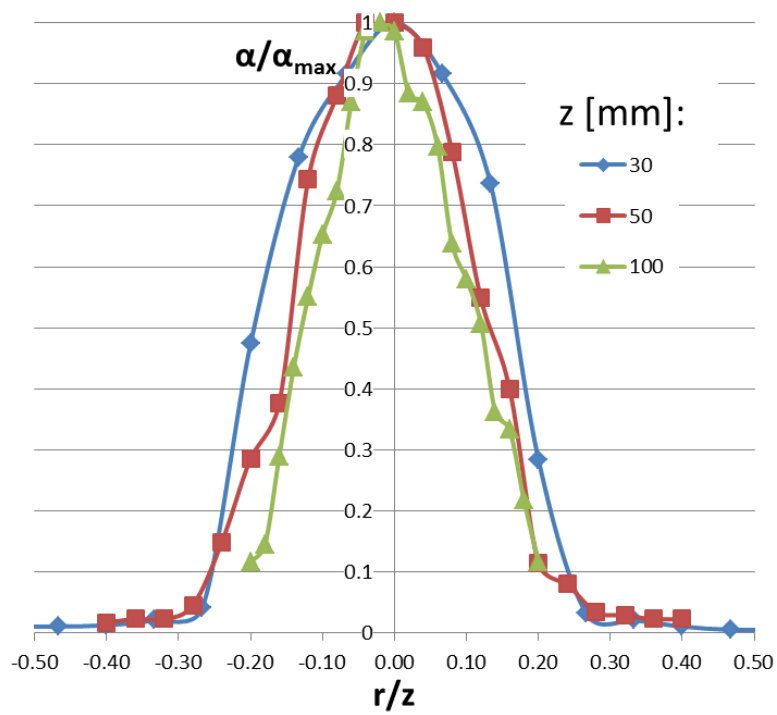


Figure 4.19: Radial void fraction profiles self-similarity.

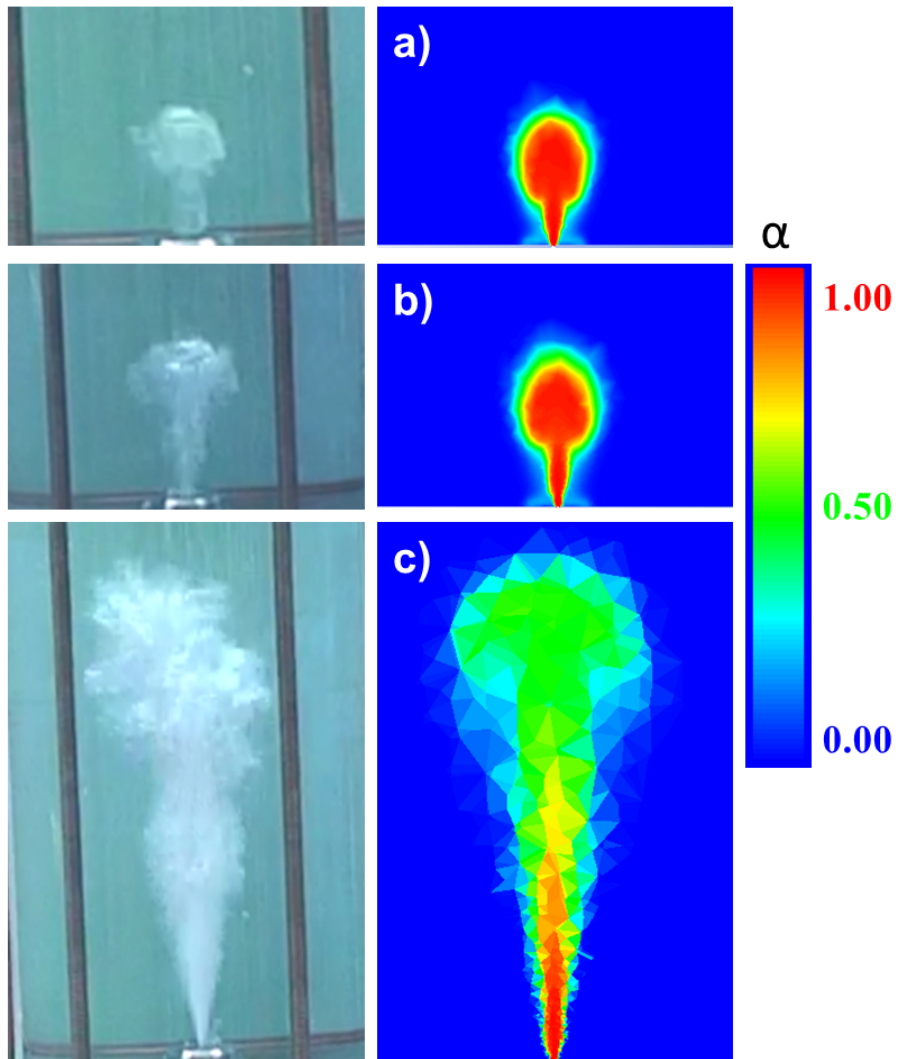


Figure 4.20: Void fraction during injection transient ($\alpha_d = 0.80$, $\alpha_b = 0.50$, $d_d = 2 \cdot 10^{-5}m$, $d_b = 2 \cdot 10^{-4}m$). Numerical results are shown for 25 ms (a), 30 ms (b) and 130 ms (c).

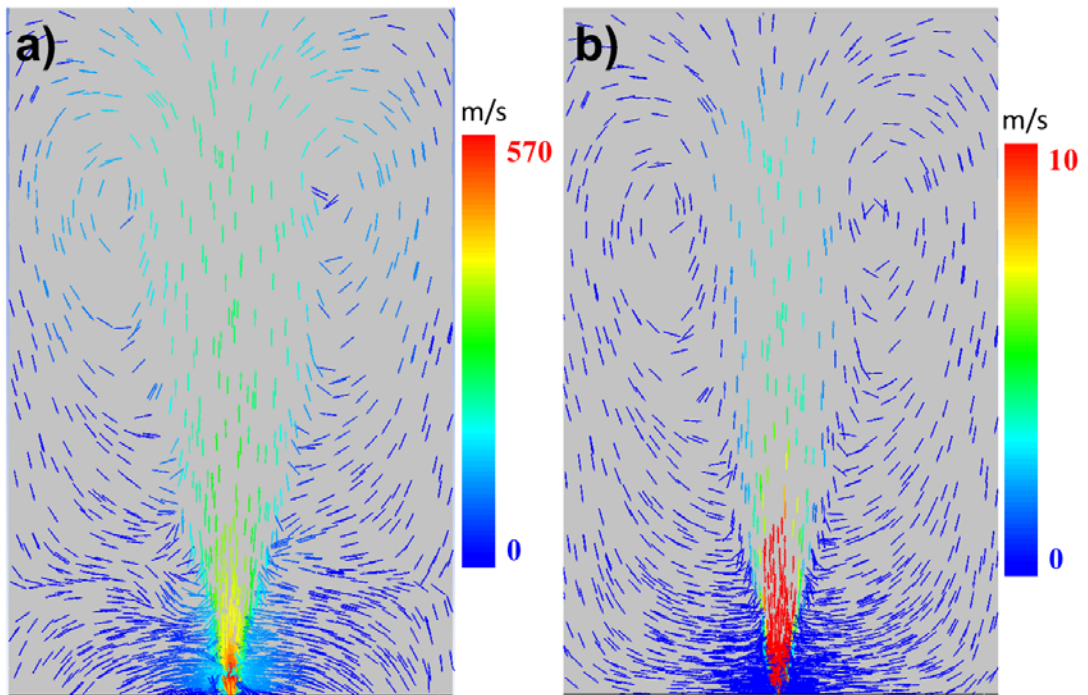


Figure 4.21: Velocity vectors of gas (a) and liquid (b) ($\alpha_d = 0.80$, $\alpha_b = 0.50$, $d_d = 2 \cdot 10^{-5}m$, $d_b = 2 \cdot 10^{-4}m$).

Chapter 5

Sodium-CO₂ chemical reaction model

Nomenclature:

- Y : mass fraction [$kg \cdot (kg_{tot})^{-1}$]
- M : molecular weight [$kg \cdot (kmol)^{-1}$]
- P : pressure [Pa]
- ρ : density [$kg \cdot m^{-3}$]
- k : molar kinetic constant [$m^3 \cdot (mol \cdot s)^{-1}$]
- D : mass diffusion coefficient [$m^2 \cdot s^{-1}$]
- r : radial distance [m]
- v : global velocity of mixture inside the boundary layer [$m \cdot s^{-1}$]
- s : stoichiometric coefficient of reaction 5.1
- ΔH : enthalpy of reaction of reaction 5.1, at 298K [$kJ \cdot (kmol)^{-1}$]
- λ : thermal conductivity [$W \cdot (mK)^{-1}$]
- R : droplet or bubble radius [m]
- R_g : gas constant [$kJ \cdot (kmol \cdot K)^{-1}$]
- T : temperature [K]

Subscripts:

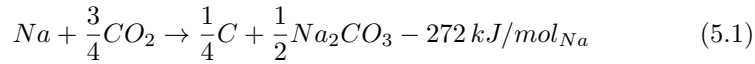
- 1: sodium vapor
- 2: carbon dioxide
- p : reaction products
- ∞ : bulk condition
- sat : saturated (equilibrium) condition

The heterogeneous reaction between liquid sodium and gaseous carbon dioxide must be considered at the Na-CO₂ interface. Since, as detailed in chapter 4, mist flow and bubbly flow are supposed to coexist in an underexpanded CO₂-into-liquid-sodium jet, two different situations must be considered: a sodium droplet with the surrounding CO₂ in the case of mist flow, and a CO₂ bubble with the surrounding sodium in the case of bubbly flow. In this chapter, the two models developed for these two different reaction mechanisms will be detailed.

The final goals of this study are:

- the estimation of the depletion time of a droplet and of a bubble;
- the determination of the reaction source term inside the species conservation equations.

The chemical reaction path considered in the present work is the following:



Following the results obtained by Gicquel [15], this is the main reaction found to take place at sodium temperatures equal or higher than 500°C. This threshold temperature was found to be 460°C by Eoh et al. [34]. Figure 5.1 shows the temperature-power plot of a typical Na-CO₂ heat exchanger: one can see that both sodium and CO₂ are hotter than 460°C in half the length of the heat exchanger, so the reaction path 5.1 should be considered.

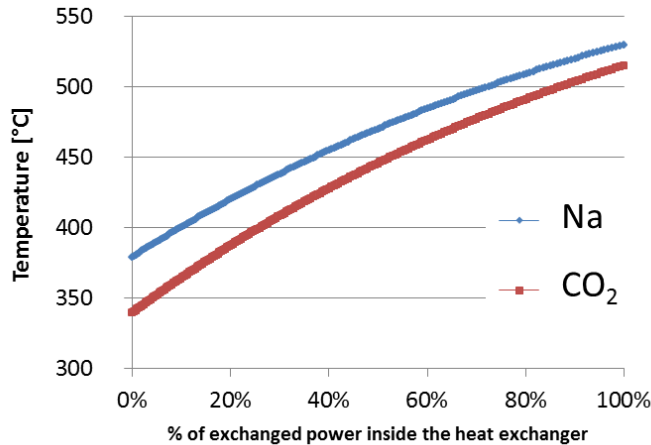


Figure 5.1: Temperature-power diagram of a typical Na-CO₂ heat exchanger.

Nevertheless, sodium and CO₂ temperatures are colder than 460°C in the other portion of the heat exchanger: a different reaction path should be investigated

for this case. In the present work, the reaction path 5.1 will be considered, assumed as the most critical due to its higher chemical reaction rate, compared to the lower temperature reaction pathways [34, 15]: however, the modeling approach of the reaction, described in this chapter, can be easily adapted to a different reaction path.

5.1 Sodium droplet reaction

The region of the jet close to the nozzle, characterized by high void fractions and high velocities, can be described by a mist flow, as discussed in chapter 4, where sodium droplets are entrained inside a continuous gas phase. In this region, the chemical reaction occurs between a sodium droplet and the surrounding CO₂ environment. In order to describe this reaction mechanism, we consider the system represented in figure 5.2.

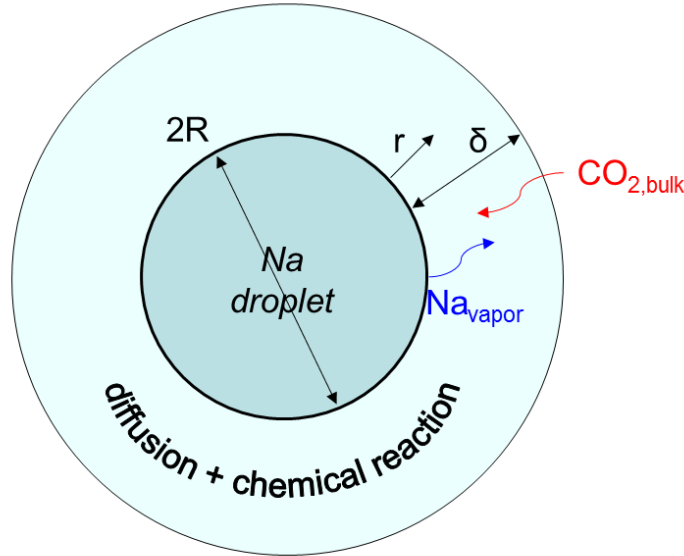


Figure 5.2: Sodium droplet reaction scheme: diffusion and reaction occur inside the droplet boundary layer δ .

The sodium droplet has a radius R , a temperature T and an absolute slip velocity ΔV . Depending on the droplet temperature, a sodium vapor pressure can be estimated which, in turn, allows to determine the sodium equilibrium vapor fraction present on the droplet surface. A diffusion boundary layer can be determined where sodium vapor can diffuse. If one only considers the diffusion of molar quantities through the boundary layer, then:

$$\frac{dn}{dt} = hS (C_{Na,sat} - C_{Na,\infty}) \quad (5.2)$$

Where $\frac{dn}{dt}$ is the sodium molar flux and S is the surface normal to the diffusion direction. If $C_{Na,sat}$ and $C_{Na,\infty}$ are the sodium vapor concentration at the droplet surface and at the limit of the diffusion boundary layer, respectively, the mass transfer coefficient h will be:

$$h = \frac{D}{\delta} \quad (5.3)$$

Where D is the diffusion coefficient and δ is the boundary layer thickness. The sodium droplet Sherwood number can be determined as follows [67]:

$$Sh_d = \frac{h \cdot 2R}{D} = 2 + 0.6Re_d^{0.5} Sc_d^{0.33} \quad (5.4)$$

Where Re_d and Sc_d are the droplet Reynolds and Schmidt number, respectively. By combining 5.3 and 5.4, one obtains the equation used to determine the boundary layer thickness:

$$\delta = \frac{2R}{2 + 0.6Re_d^{0.5} Sc_d^{0.33}} \quad (5.5)$$

This is the thickness of the boundary layer where diffusion and reaction processes between sodium vapor and CO₂ take place.

5.1.1 Model equations and boundary conditions

The dynamics of the droplet depletion is now studied, taking the droplet mass center as the origin of the system reference.

In order to develop the system of equations representing the reaction-diffusion problem, the assumption of steady-state problem, mono-dimensional representation, spherical symmetry and constant pressure inside the boundary layer are retained. Moreover, it is assumed a bimolecular reaction between Na and CO₂, with a reaction rate obeying kc_1c_2 (c_i corresponding to the molar concentration of the i species).

The radial convection term in the mass balance is due to the droplet depletion (caused by the liquid sodium consumption and the continuity by the gas and the liquid phases).

The equations to be solved, inside the boundary layer δ , are the mass conservation of the mixture (eq. 5.6), the species conservation of sodium vapor and carbon dioxide (eq. 5.7 and 5.8), and the energy equation of the mixture (eq. 5.9) [68]:

$$\frac{d}{dr} \rho v r^2 = 0 \quad (5.6)$$

$$\rho v \frac{dY_1}{dr} = M_1 \frac{k\rho^2 Y_1 Y_2}{M_1 M_2} (-s_1) + \frac{1}{r^2} \frac{d}{dr} \left(r^2 D \rho \frac{dY_1}{dr} \right) \quad (5.7)$$

$$\rho v \frac{dY_2}{dr} = M_2 \frac{k\rho^2 Y_1 Y_2}{M_1 M_2} (-s_2) + \frac{1}{r^2} \frac{d}{dr} \left(r^2 D \rho \frac{dY_2}{dr} \right) \quad (5.8)$$

$$\rho v c_p \frac{dT}{dr} = -\Delta H_r \frac{k Y_1 Y_2}{M_1 M_2} \rho^2 + \frac{1}{r^2} \frac{d}{dr} \left(r^2 \lambda \frac{dT}{dr} \right) \quad (5.9)$$

In 5.7 and 5.8, the stoichiometric coefficients s_1 and s_2 are positive. In addition to these equations, an equation of state must be added to solve the system. Inside the boundary layer, sodium vapor and CO₂ react to form solid products. The density of the gas-solid mixture is:

$$\rho = \left[\frac{RT}{P} \left(\frac{Y_1}{M_1} + \frac{Y_2}{M_2} \right) + \frac{1 - Y_1 - Y_2}{\rho_p} \right]^{-1} \quad (5.10)$$

Knowing that $Y_1 + Y_2 + Y_P = 1$.

The time rate of change of energy inside the droplet must also be taken into account. This is due to two contributions: the droplet vaporization, which causes a negative heat flux (thus, cooling the droplet), and the conductive heat flux at the droplet surface, which is positive since the temperature outside the droplet (inside the boundary layer) is higher than the droplet temperature. The following equation is obtained:

$$m_d c_{p,d} \frac{dT_d}{dt} = -S_d \lambda \left[\frac{dT}{dr} \right]_R + \rho_d S_d \frac{dR}{dt} \Delta h_{vap,d} \quad (5.11)$$

Where m_d , S_d , T_d and Δh_{vap} are the mass, the surface, the temperature and the enthalpy of vaporization of the droplet, respectively. The initial assumption that the conductive and vaporization contributions are of the same order of magnitude and, therefore, that the time rate of change of the droplet energy is equal to zero, is taken. This assumption must be verified with the obtained results. In the following paragraph 5.1.3, this assumption will be checked and its validity confirmed.

In order to solve the system of equations, boundary conditions must be defined for equations 5.6, 5.7, 5.8 and 5.9. For eq. 5.7, Y_1 on the droplet surface is the vapor equilibrium concentration ($Y_{1,sat}$) corresponding to the vapor pressure (P_{sat}). Assuming solid products contribution to pressure negligible, one can write:

$$\frac{P_{sat}}{P_\infty} = \frac{\frac{Y_{1,sat}}{M_1}}{\frac{Y_{1,sat}}{M_1} + \frac{Y_{2,R}}{M_2}} \quad (5.12)$$

At the outer limit of the boundary layer, the following Dirichlet boundary condition must be satisfied:

$$Y_{1,R+\delta} = 0 \quad (5.13)$$

Concerning eq. 5.8, CO₂ concentration at boundary layer outer limit is the bulk concentration ($Y_{2,\infty}$), then the corresponding Dirichlet boundary condition applies:

$$Y_{2,R+\delta} = Y_{2,bulk} = Y_{2,\infty} \quad (5.14)$$

At the droplet surface, CO₂ flux must be zero, therefore the following mixed boundary condition must be satisfied:

$$vY_2 - D \frac{\partial Y_2}{\partial r} = 0 \quad (5.15)$$

In order to evaluate boundary condition 5.12, a correlation for the sodium saturation pressure is needed. The one developed by the CEA is employed:

$$\log_{10} P_{sat} = 11.364 - \frac{5562}{T} - 0.5 \cdot \log_{10} T \quad (5.16)$$

Where pressure is in Pascal and temperature in degree Kelvin. However, this correlation is valid for a flat interface, whereas its validity for the considered droplet must be verified. The Kelvin equation for droplet vapor pressure is:

$$\frac{P'_{sat}}{P_{sat}} = \exp\left(\frac{2\sigma V_m}{R_g T \cdot R}\right)$$

Where V_m is the molar volume. Replacing with the actual values, one can find that $\frac{P'_{sat}}{P_{sat}} = 1.65 \cdot 10^{-4}$, which confirms that equation 5.16 can be employed also for the particle considered in the present study.

The sodium-vapor-CO₂ diffusion coefficient must be also evaluated. The Chapman-Enskog theory has been employed for this estimation: the diffusion coefficient D results being equal to $2 \cdot 10^{-5} \text{ m}^2 \cdot \text{s}^{-1}$, at 500°C.

The thermal conductivity of the sodium-vapor-CO₂ system (λ) has been taken equal to $5 \cdot 10^{-2} \text{ W} \cdot (\text{mK})^{-1}$, which is a typical order of magnitude of gas conductivity.

For eq. 5.9, temperature at $r = R + \delta$ will be the gas bulk temperature, whereas on droplet surface temperature will correspond to sodium liquid droplet temperature. The latter assumption is true only if the droplet temperature can be considered constant along the droplet radius. The governing parameter is the Biot number, which represents the ratio of the rate of external convection to internal conduction, and is defined as:

$$Bi = \frac{H \cdot R}{\lambda_d}$$

Where λ_d is the thermal conductivity of the droplet. H is the convective heat transfer which can be estimated through the Nusselt number. At low Biot

numbers, generally lower than 0.1, the lumped mass assumption is adequate. Using the Ranz Marshall correlation, for a conservative droplet Reynolds number of 1000 (which is a very high and non-realistic value for the present case, but conservative since it leads to higher heat transfer values and, thus, higher Biot number) and an estimated droplet Prandtl number of 1, Nusselt number is equal to 22.5. We can rewrite the Biot number:

$$Bi = \frac{H \cdot R}{\lambda} = \frac{Nu \cdot \lambda_{CO_2} \cdot R}{2R \cdot \lambda_{Na}} = \frac{Nu \cdot \lambda_{CO_2}}{2\lambda_{Na}}$$

Sodium thermal conductivity can be estimated using the following correlation obtained by CEA:

$$\lambda_{Na} \left[\frac{W}{cm^\circ C} \right] = 0.918 - 4.9 \cdot 10^{-4} T$$

For a temperature of 700°C, which, from Gicquel's results, is in the range of temperature reached following Na-CO₂ chemical reaction, $\lambda_{Na} = 57.5 \text{ W}/(\text{m}^\circ\text{C})$. The resulting Biot number is around $4 \cdot 10^{-2}$, which is significantly lower than 0.1, meaning that, also considering the conservative assumptions retained, the hypothesis of constant temperature inside the sodium droplet can be taken.

5.1.2 Solving method

The system of equations 5.6, 5.7, 5.8, 5.9 and 5.10 has to be solved inside δ . From equation 5.6, one can write:

$$\rho v r^2 = \text{constant} = K \quad (5.17)$$

the value of K can be determined considering boundary conditions on droplet surface, where $r = R$, $\rho = \rho_R$ and $v = \frac{dR}{dt}$ (representing the variation of droplet radius with time). One recalls that as usually accepted and shown, external mass transfer in a growth or dissolution process is considered as a quasi-steady phenomenon. It follows that the value of the constant K is:

$$K = \rho_R R^2 \frac{dR}{dt} \quad (5.18)$$

It can be noticed that equations 5.7 and 5.8 are non-linear and coupled. Therefore, it is chosen to isolate these two equations from the other equations of the system and to solve them employing the Newton-Raphson method. Once Y_1 and Y_2 are obtained as results of equations 5.7 and 5.8, equation 5.9 and 5.10 are solved in order to calculate T and ρ . The complete algorithm adopted for solving the complete system of equations is showed in figure 5.3.

Finite difference scheme has been employed in order to transform the differential equations 5.7, 5.8 and 5.9 into algebraical equations. First, equations 5.7 and 5.8 are considered. The following non-dimensional terms are defined:

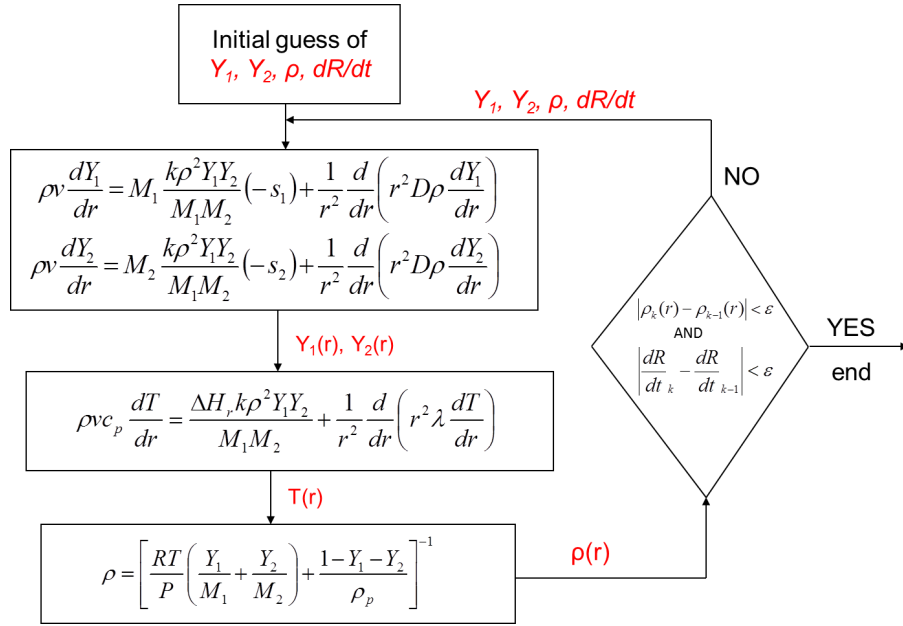


Figure 5.3: Solving algorithm of the system of equations 5.6, 5.7, 5.8 and 5.9.

$$r' = \frac{r - R}{\delta} \quad (5.19)$$

$$\rho' = \frac{\rho}{\rho_\infty} \quad (5.20)$$

Using 5.18, 5.19 and 5.20, equation 5.7 can be written as follows:

$$\frac{R^2 \rho_R \frac{dR}{dt}}{(R + r'\delta)^2 \delta} \frac{dY_1}{dr'} = k \rho'^2 \rho_\infty^2 \frac{Y_1 Y_2}{M_2} (-1) + \frac{1}{(R + r'\delta)^2 \delta} \frac{d}{dr'} \left[(R + r'\delta)^2 \frac{D \rho' \rho_\infty}{\delta} \frac{dY_1}{dr'} \right] \quad (5.21)$$

Defining:

$$A = \frac{R^2 \rho_R \frac{dR}{dt}}{\delta}$$

$$B = k \rho_\infty^2 \frac{(-1)}{M_2}$$

$$C = \frac{D \rho_\infty}{\delta^2}$$

Then equation 5.21 can be written as:

$$\frac{A}{(R+r'\delta)^2} \frac{dY_1}{dr'} = B\rho'^2 Y_1 Y_2 + \frac{C}{(R+r'\delta)^2} \left\{ \frac{d}{dr'} \left[\rho' (R+r'\delta)^2 \frac{dY_1}{dr'} \right] \right\} \quad (5.22)$$

In writing 5.22, the assumption of constant reaction rate k along δ is taken; k is calculated through an Arrhenius equation:

$$k = k_0 \cdot \exp \left(\frac{-E_a}{R_g \left(\frac{T_{r=R} + T_{r=R+\delta}}{2} \right)} \right) \quad (5.23)$$

The part inside the parenthesis of the second *RHS* term in 5.22 can be developed as:

$$\left\{ \frac{d}{dr'} \left[(R+r'\delta)^2 \frac{dY_1}{dr'} \right] \right\} = R^2 \frac{d^2 Y_1}{dr'^2} + 2R\delta \frac{d}{dr'} \left(r' \frac{dY_1}{dr'} \right) + \delta^2 \frac{d}{dr'} \left(r'^2 \frac{dY_1}{dr'} \right) \quad (5.24)$$

Supposing to divide the boundary layer thickness $N - 1$ elements, the corresponding N nodes will be identified by index i , with $i = [1, N]$. Using the central scheme of the finite difference method, the derivative in the first, second and third terms of the *RHS* of equation 5.24 can be approximated through the following algebraical equations:

$$R^2 \frac{d^2 Y_1}{dr'^2} = R^2 \frac{Y_{1,i+1} - 2Y_{1,i} + Y_{1,i-1}}{\Delta r'^2} \quad (5.25)$$

$$2R\delta \frac{d}{dr'} \left(r' \frac{dY_1}{dr'} \right) = 2R\delta \frac{r'_{i+1/2} \frac{Y_{1,i+1} - Y_{1,i}}{\Delta r'} - r'_{i-1/2} \frac{Y_{1,i} - Y_{1,i-1}}{\Delta r'}}{\Delta r'} \quad (5.26)$$

$$\delta^2 \frac{d}{dr'} \left(r'^2 \frac{dY_1}{dr'} \right) = \delta^2 \frac{r'_{i+1/2} \frac{2Y_{1,i+1} - Y_{1,i}}{\Delta r'} - r'_{i-1/2} \frac{2Y_{1,i} - Y_{1,i-1}}{\Delta r'}}{\Delta r'} \quad (5.27)$$

In the same way, the first derivative appearing in the *LHS* of 5.22 can be written as:

$$\frac{dY_1}{dr'} = \frac{Y_{1,i+1} - Y_{1,i-1}}{2\Delta r'} \quad (5.28)$$

Equation 5.22 can be now rewritten using equations 5.25, 5.26, 5.27 and 5.28. After substitution and rearrangement, the following algebraical equation can be obtained:

$$\begin{aligned}
& \left[\frac{A}{(R+r'_i\delta)^2 2\Delta r'} - \frac{C\rho'_i}{(R+r'_i\delta)^2 \Delta r'^2} \left(R^2 + 2R\delta r'_{i+1/2} + \delta^2 r'_{i+1/2}{}^2 \right) \right] Y_{1,i+1} + \\
& \left[-B\rho'_i{}^2 Y_{2,i} - \frac{C\rho'_i}{(R+r'_i\delta)^2 \Delta r'^2} \left(-2R^2 - 2R\delta r'_{i+1/2} - 2R\delta r'_{i-1/2} - \delta^2 r'_{i+1/2}{}^2 - \delta^2 r'_{i-1/2}{}^2 \right) \right] Y_{1,i} + \\
& \left[-\frac{A}{(R+r'_i\delta)^2 2\Delta r'} - \frac{C\rho'_i}{(R+r'_i\delta)^2 \Delta r'^2} \left(R^2 + 2R\delta r'_{i-1/2} + \delta^2 r'_{i-1/2}{}^2 \right) \right] Y_{1,i-1} = 0
\end{aligned} \tag{5.29}$$

The same form of equation 5.29, obtained for equation 5.7, can be derived also for equation 5.8, giving:

$$\begin{aligned}
& \left[\frac{A}{(R+r'_i\delta)^2 2\Delta r'} - \frac{C\rho'_i}{(R+r'_i\delta)^2 \Delta r'^2} \left(R^2 + 2R\delta r'_{i+1/2} + \delta^2 r'_{i+1/2}{}^2 \right) \right] Y_{2,i+1} + \\
& \left[-E\rho'_i{}^2 Y_{1,i} - \frac{C\rho'_i}{(R+r'_i\delta)^2 \Delta r'^2} \left(-2R^2 - 2R\delta r'_{i+1/2} - 2R\delta r'_{i-1/2} - \delta^2 r'_{i+1/2}{}^2 - \delta^2 r'_{i-1/2}{}^2 \right) \right] Y_{2,i} + \\
& \left[-\frac{A}{(R+r'_i\delta)^2 2\Delta r'} - \frac{C\rho'_i}{(R+r'_i\delta)^2 \Delta r'^2} \left(R^2 + 2R\delta r'_{i-1/2} + \delta^2 r'_{i-1/2}{}^2 \right) \right] Y_{2,i-1} = 0
\end{aligned} \tag{5.30}$$

With:

$$E = k\rho_\infty^2 \frac{(-0.75)}{M_1}$$

Equation 5.29 must be solved for all node i , except for $i = 1 = R$ and $i = N = R + \delta$, where Dirichlet boundary conditions are fixed. Equation 5.30 must be solved for every node i , except for $i = N = R + \delta$, where Dirichlet boundary condition is fixed. In node $i = 1$, the boundary condition 5.15 must be implemented. This mixed boundary condition can be solved introducing an artificial node “0”, in order to be able to estimate the derivative in R ($i = 1$). One can write the boundary condition 5.15 and solve for $Y_{2,0}$:

$$\frac{dR}{dt} Y_{2,1} - \frac{D}{\delta} \frac{(Y_{2,2} - Y_{2,0})}{2\Delta r'} = 0 \tag{5.31}$$

$$Y_{2,0} = Y_{2,2} - \frac{2\Delta r'\delta}{D} \frac{dR}{dt} Y_{2,1} \tag{5.32}$$

The value of $Y_{2,0}$ is introduced in 5.30 for $i = 1$.

Boundary conditions 5.12 and 5.15 can be used to calculate the sodium mass fraction in $r = R$, $Y_{1,sat}$, through the system 5.33:

$$\begin{cases} \frac{P_{sat}}{P_\infty} = \frac{\frac{Y_{1,sat}}{M_1}}{\frac{Y_{1,sat}}{M_1} + \frac{Y_{2,R}}{M_2}} \\ \frac{dR}{dt} Y_2 - D \frac{\partial Y_2}{\partial r} = 0 \end{cases} \tag{5.33}$$

The system of non-linear and coupled equations 5.29 and 5.30 is solved using the Newton-Raphson method. Considering a general non-linear system $f(Y) = 0$, starting from an approximated solution $Y^{(k)}$ (where k stands for the iteration number), this method allows to find a corrected value $Y^{(k+1)}$ using the following correction method:

$$Y^{(k+1)} = Y^{(k)} - J^{-1} f(Y^{(k)}) \quad (5.34)$$

Where J is the Jacobian matrix of the system. In the present case, with a system of two equations, Y and $f(Y)$ are two vectors of size $2 \cdot (N - 3)$, since equations 5.29 and 5.30 are solved in $(N - 2)$ and in $(N - 1)$ nodes, respectively. Calling $f(Y_1)$ and $f(Y_2)$ equations 5.29 and 5.30, respectively, one obtains:

$$Y = \begin{bmatrix} Y_{2,i=1} \\ Y_{1,i=2} \\ Y_{2,i=2} \\ \vdots \\ \vdots \\ Y_{1,i=N-1} \\ Y_{2,i=N-1} \end{bmatrix} \quad (5.35)$$

$$f(Y) = \begin{bmatrix} f(Y_2)_{i=1} \\ f(Y_1)_{i=2} \\ f(Y_2)_{i=2} \\ \vdots \\ \vdots \\ f(Y_1)_{i=N-1} \\ f(Y_2)_{i=N-1} \end{bmatrix} \quad (5.36)$$

The Jacobian is a $[2 \cdot (N - 3) \times 2 \cdot (N - 3)]$ matrix, evaluated as follows:

Starting from a guessed values of Y , the correction in 5.34 is applied until the desired convergence ε is achieved. If the obtained solution is correct, not only the condition $(Y^k - Y^{k-1}) \leq \varepsilon$ must be satisfied, but also the condition $f(Y) = 0$ must be verified.

With the same procedure implemented for equations 5.7 and 5.8, also equation 5.9 can be transformed in an algebraic form using finite differences. Once the solution for Y_1 and Y_2 has been found, these values are used to evaluate temperature on nodes $i = [2, N - 1]$, through the discretized form of equation 5.9:

$$\begin{aligned} & \left[\frac{A'}{(R+r'_i\delta)^2 2\Delta r'} - \frac{C'}{(R+r'_i\delta)^2 \Delta r'^2} \left(R^2 + 2R\delta r'_{i+1/2} + \delta^2 r'_{i+1/2}{}^2 \right) \right] T'_{i+1} + \\ & \left[\frac{-C'}{(R+r'_i\delta)^2 \Delta r'^2} \left(-2R^2 - 2R\delta r'_{i+1/2} - 2R\delta r'_{i-1/2} - \delta^2 r'_{i+1/2}{}^2 - \delta^2 r'_{i-1/2}{}^2 \right) \right] T_i + \\ & \left[-\frac{A'}{(R+r'_i\delta)^2 2\Delta r'} - \frac{C'}{(R+r'_i\delta)^2 \Delta r'^2} \left(R^2 + 2R\delta r'_{i-1/2} + \delta^2 r'_{i-1/2}{}^2 \right) \right] T_{i-1} = B' \rho_i'^2 Y_{1,i} Y_{2,i} \end{aligned} \quad (5.38)$$

Where:

$$T' = \frac{T - T_\infty}{T_m - T_\infty}$$

$$A' = \frac{R^2 \rho_R \rho_\infty c_p}{\delta} \frac{dR}{dt} (T_m - T_\infty)$$

$$B' = \frac{-\Delta H_r k \rho_\infty^2}{M_1 M_2}$$

$$C' = \frac{\lambda (T_m - T_\infty)}{\delta^2}$$

T_m is a defined maximum temperature, for example the adiabatic flame temperature. Equation 5.38 forms a linear system which can be solved to find T_i in $i = [2, N - 1]$. Once $Y_{1,i}$, $Y_{2,i}$ and T_i are obtained, the last step is to solve equation 5.10 for the density ρ_i on nodes $i = [1, N]$. As showed in the scheme 5.3, the updated values of density are introduced in 5.29 and 5.30, and new values of $Y_{1,i}$ and $Y_{2,i}$ are obtained; new values of temperature and density are calculated, and the process is repeated until convergence of the entire system is obtained.

5.1.3 Results

The system of equations and the numerical algorithm employed to solve it, described in the previous paragraph, have been implemented into the Scilab software, which allows to perform matrix operation.

As one can see from equations 5.29, 5.30 and 5.38, the term $\frac{dR}{dt}$ must be known in order to start the solving algorithm. Therefore, an initial guess is given to the algorithm, and the effective $\frac{dR}{dt}$ value is then recalculated and employed for a new calculation, until convergence is achieved. The sodium droplet depletion is caused by both convection and diffusion processes. The following mass flux conservation equation can be written in $r = R$:

$$\rho_{Na,l} \frac{dR}{dt} = -\rho_{1,R} \left[Y_{1,R} \frac{dR}{dt} - D \left(\frac{\partial Y_1}{\partial r} \right)_R \right] \quad (5.39)$$

Therefore, $\frac{dR}{dt}$ can be calculated through equation 5.39.

Once the Na and CO₂ mass fractions inside δ are calculated, the reaction rate must be determined. This can be done by integrating the chemical reaction source term inside the entire droplet boundary layer δ . Therefore, the sodium reaction rate \dot{m}_{Na} , measured in kilograms per second, is:

$$\dot{m}_{Na} = \int_{r=R}^{r=R+\delta} k Y_1 Y_2 \frac{\rho^2}{M_2} s_1 \cdot 4\pi r^2 dr \quad (5.40)$$

As the mass fraction of sodium is equal to zero at the end of the boundary layer, \dot{m}_{Na} represents also the droplet mass consumption.

Since the reaction rate depends on the droplet radius (different mass fraction profiles are obtained for different droplet radius), equation 5.39 is used to calculate droplet radius after a certain time dt , and a new reaction rate is calculated with equation 5.40 for the smaller droplet radius: in this way, a proper reaction rate is estimated for a number of droplet radius during droplet depletion time. For example, considering droplet initial diameter of 20 micron, five values of reaction rate have been calculated from the initial diameter to the final complete droplet depletion. The mean reaction rate during droplet depletion can be, then, evaluated.

Fixing the chemical reaction rate (that is the pre-exponential factor k_0 and the activation energy E_a) in the Arrhenius type reaction rate of equation 5.23, the parameters influencing the calculated consumption rate are:

- the sodium droplet temperatures (which defines the sodium vapor pressure and, in turn, the vapor sodium mass fraction in $r = R$);
- the CO₂ mass fraction at bulk $Y_{2,\infty}$ (once the reaction begins, reaction products are formed and $Y_{2,\infty}$ gradually decreases from 1 to 0);
- the droplet slip velocity (which defines the droplet boundary layer thickness δ).

In order to reduce the complexity and the number of sensitivity analysis to perform, a mean droplet slip velocity has been considered in the present study. Experimental results of underexpanded jets of CO₂-into-Na and H₂O_{vapor}-into-Na have been reported in paragraph 2.1, and they show how the chemical reactions seem to occur in the region very close to the nozzle outlet: Sekkouti

[23] found that, for a steam pressure of 10 bars, the maximum temperature is measured at an axial distance of about ten nozzle diameter, and the begin of significant cool-down is noticed to occur already within a twenty nozzle diameter distance. Following these results, the droplet slip velocity has been fixed to a mean value inside the axial distance range: calculated slip velocity for a gas pressure of 7 bars, calculated in paragraph 4.1, is around 50 m/s at a ten nozzle diameter axial distance and 2 m/s at a twenty nozzle diameter axial distance, with a mean value of 19 m/s. Figure 5.4 shows the boundary layer width estimated through equation 5.5, as a function of droplet slip velocity, for a droplet diameter of 20 μm , which is the value obtained applying the Epstein's correlation 2.1 for this value of pressures.

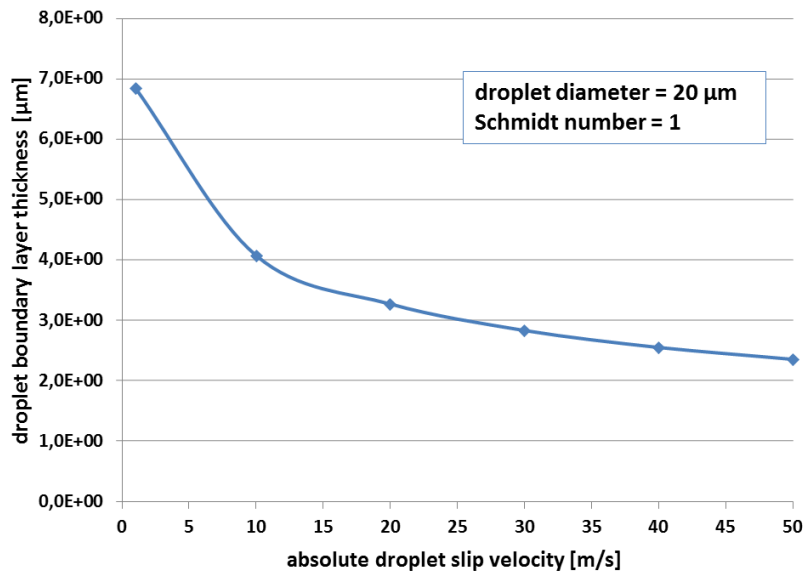


Figure 5.4: Droplet boundary layer thickness (δ) as a function of droplet slip velocity.

The Sherwood number corresponding to the droplet slip velocities shown in figure 5.4 ranges from 2.0 to 6.2. The thickness of δ has been taken equal to 3.3 μm , corresponding to a 19 m/s slip velocity, the mean value found in the region from ten to twenty nozzle-diameters. However, this represents the initial boundary layer thickness, since, during droplet depletion, droplet diameter decreases leading to a decreasing of boundary layer thickness. This aspect will be taken into account when calculating the reaction rate for a determined droplet diameter during its depletion.

The transport mechanism, inside the droplet boundary layer, is essentially due to the diffusion. The Kolmogorov scale, η_K , can be evaluated through $\eta_K = \left(\frac{\nu^3}{\epsilon}\right)^{1/4}$, where ν is the gas (CO₂) kinematic viscosity. Even if the turbulent dissipation rate, for the region ranging from ten to twenty nozzle-diameters, gets as higher as $10^4 \text{ m}^2/\text{s}^3$ (numerical result of the simulations detailed in chapter 4), the resulting Kolmogorov length scale keeps higher than

20 μm . Moreover, the hydro-dynamic droplet boundary layer can be evaluated through $\delta_{hydr.} = 4 \left(\frac{\nu \cdot d_d}{2 \cdot \Delta V} \right)^{1/2}$ [69], where ΔV is the droplet relative velocity: it results higher than 15 μm . This shows that the diffusion boundary layer is smaller than the Kolmogorov scale and the hydro-dynamic boundary layer, which confirms the consistency of employing a diffusion boundary layer.

In order to calculate the Arrhenius rate, the value of the activation energy is supposed known and equal to $4 \cdot 10^4 J \cdot mol^{-1}$, following the results obtained by Gicquel [15]. From this assumption, it follows that the pre-exponential factor is the variable which influences the resulting reaction rate. As an example, figure 5.5 shows the calculated Na and CO₂ mass fraction profiles along the droplet boundary layer, for different CO₂ bulk concentration, for a pre-exponential factor equal to $1 \cdot 10^9 m^3 \cdot (mol \cdot s)^{-1}$. Whereas figure 5.6 shows mass fraction profiles for the same CO₂ bulk concentration and different droplet temperatures, for a pre-exponential factor equal to $1 \cdot 10^9 m^3 \cdot (mol \cdot s)^{-1}$. Figure 5.7 shows the calculated sodium consumption rate of a single droplet, for a pre-exponential factor equal to $1 \cdot 10^9 m^3 \cdot (mol \cdot s)^{-1}$, as a function of sodium temperature and CO₂ mass fraction at bulk.

The sodium reaction rate is found to decrease with the decrease of the droplet radius, during the depletion process, as expected due to the decreasing of the boundary layer thickness. However, since the total volume of the droplet also decreases during the droplet depletion, a lower reaction rate could lead to the same depletion rate with time. Figure 5.8 shows the typical calculated droplet consumption as a function of time: one can observe how the droplet consumption is almost constant with time.

As discussed in the previous paragraph 5.1, the assumption was taken that the time rate of change of the droplet energy is equal to zero. Through the results obtained, this assumption can be checked. Using equation 5.11, one can consider that the time rate of change of the droplet energy is negligible if the positive conductive and the negative vaporization heat flux contributions are of the same order of magnitude, which is verified if:

$$\left| \lambda \left[\frac{dT}{dr} \right]_R \right| \approx \left| \rho_d \frac{dR}{dt} \Delta h_{vap} \right| \quad (5.41)$$

The calculated temperature profile inside the droplet boundary layer is shown in figure 5.9, for two different cases of pre-exponential factor ($1 \cdot 10^9 m^3 \cdot (mol \cdot s)^{-1}$ and $1 \cdot 10^{10} m^3 \cdot (mol \cdot s)^{-1}$) and for a droplet and gas-bulk temperature of 973K. The depletion rate $\frac{dR}{dt}$ is also a result of the calculation, whereas the sodium vaporization enthalpy is $97.4 kJ/mol$. Thus, it is possible to verify if the condition 5.41 is verified: figure 5.10 shows this calculation, and one can see that the order of magnitude of the two contributions is the same.

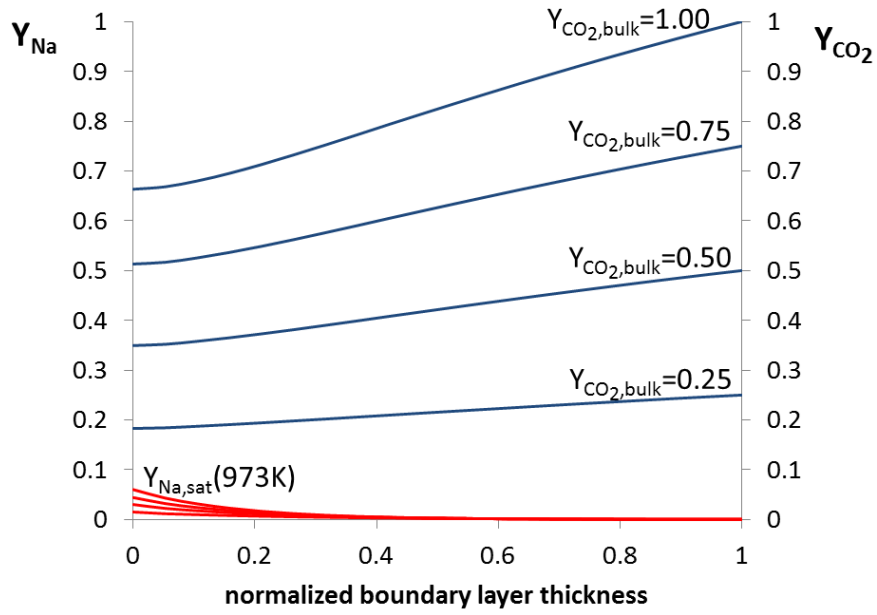


Figure 5.5: Mass fraction profiles of Na and CO₂, as a function of CO₂ bulk mass fraction, for a sodium temperature of 973K and a pre-exponential factor $k_0 = 1 \cdot 10^9 m^3 \cdot (mol \cdot s)^{-1}$.

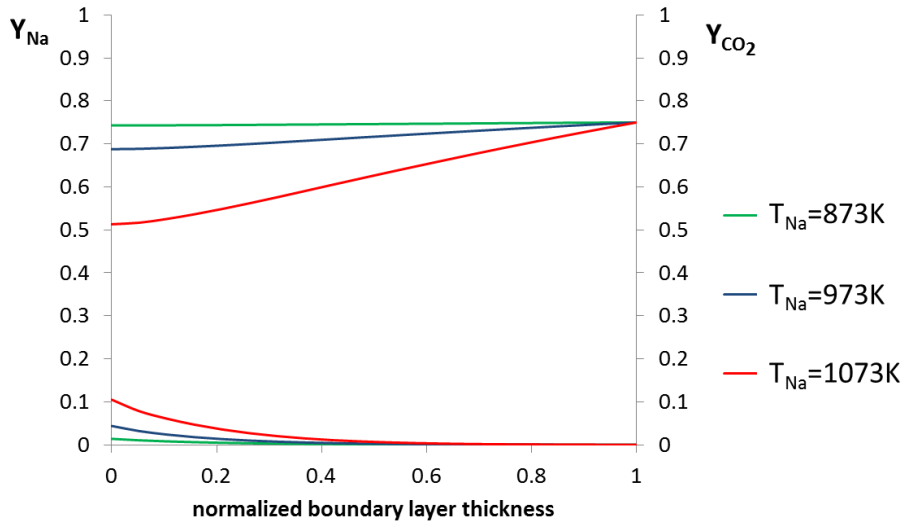


Figure 5.6: Mass fraction profiles of Na and CO₂, as a function of sodium temperature, for a CO₂ bulk mass fraction of 75% and a pre-exponential factor $k_0 = 1 \cdot 10^9 m^3 \cdot (mol \cdot s)^{-1}$.

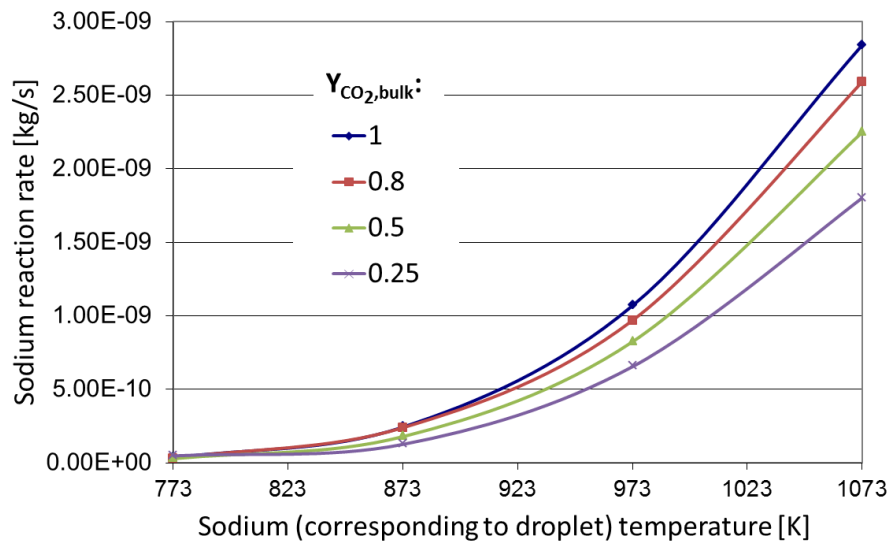


Figure 5.7: Sodium reaction rate for a single droplet, as a function of sodium temperature and CO₂ mass fraction at bulk, for $k_0 = 1 \cdot 10^9 \text{ m}^3 \cdot (\text{mol} \cdot \text{s})^{-1}$.

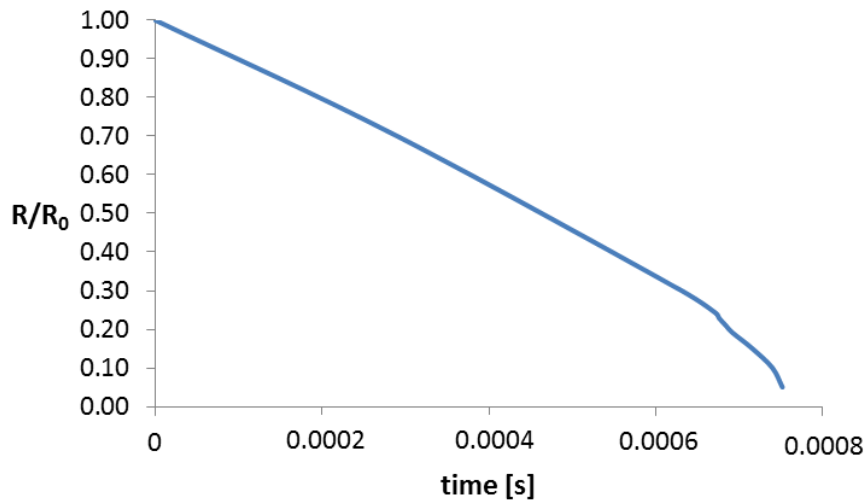


Figure 5.8: Droplet radius as a function of time, for a sodium temperature of 973K, $Y_{2,bulk} = 1$ and $k_0 = 1 \cdot 10^{10} \text{ m}^3 \cdot (\text{mol} \cdot \text{s})^{-1}$.

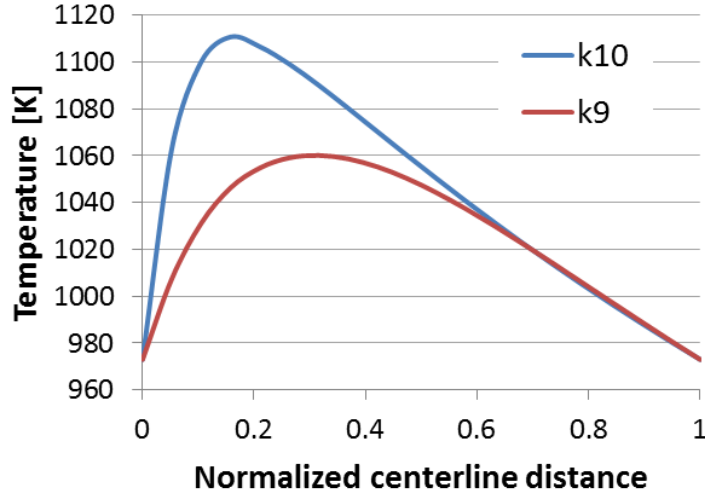


Figure 5.9: Calculated temperature profiles, for the case of $T_d = T_{CO_2,bulk} = 973$ and for a pre-exponential factor of $1 \cdot 10^9 \text{ m}^3 \cdot (\text{mol} \cdot \text{s})^{-1}$ (in figure, k_9), and $1 \cdot 10^{10} \text{ m}^3 \cdot (\text{mol} \cdot \text{s})^{-1}$ (in figure, k_{10}).

| k_0 [$\text{m}^3(\text{mol}\cdot\text{s})^{-1}$] | R [m] | T_d [K] | $\lambda \left[\frac{dT}{dr} \right]_R$ | $\rho_d \frac{dR}{dt} \Delta h_{\text{vap}}$ |
|---|-------------------|-----------|--|--|
| $1 \cdot 10^9$ | $1 \cdot 10^{-5}$ | 973 | $11.5 \cdot 10^6 \frac{W}{m^2}$ | $11.6 \cdot 10^6 \frac{W}{m^2}$ |
| $1 \cdot 10^{10}$ | $1 \cdot 10^{-5}$ | 973 | $27.2 \cdot 10^6 \frac{W}{m^2}$ | $18.0 \cdot 10^6 \frac{W}{m^2}$ |

Figure 5.10: Conductive and vaporization heat flux comparison.

5.2 CO₂ bubble reaction

Starting from a certain distance downstream the jet centerline, when slip velocity and void fraction decrease, the gas core of the jet breaks and bubbly flow is the two-phase pattern observed. In order to fully represent the heterogeneous CO₂-Na reaction, also a CO₂ bubble reaction with the surrounding liquid sodium must be taken into account.

The system shown in figure 5.11 is considered: the contact between the two reactants occurs inside the bubble, where vapor sodium diffuse from the interface to the bubble center. Together with steady-state approximation and spherical symmetry, the assumption that the reaction products are removed infinitely fast from inside the bubble and from the interface is taken, meaning that only CO₂ and Na are present inside the bubble. The pressure inside the bubble is almost equal to the pressure of liquid sodium during the bubble dynamics

(a small difference exists following Laplace equation). As CO₂ is consumed by reaction with sodium, the number of gas moles decreases and the bubble interface moves towards the bubble center. The role of the pressure is the most influencing parameter for the bubble depletion, compared to the case of droplet depletion.

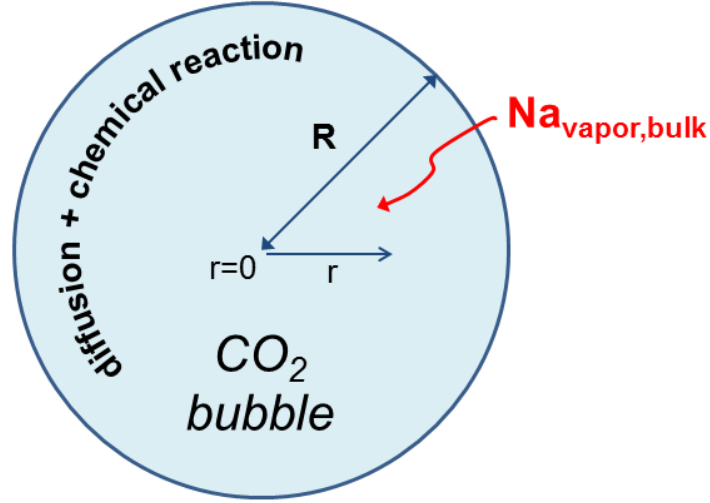


Figure 5.11: CO₂ bubble reaction scheme: diffusion and reaction occur inside the bubble ($0 < r < R$).

5.2.1 Model equations and boundary conditions

Since only CO₂ and Na are present inside the bubble, only one species equation needs to be solved: it is chosen to solve the sodium conservation equation, following that CO₂ mass fraction will be obtained by the relation:

$$Y_2 = 1 - Y_1 \quad (5.42)$$

The equations describing the diffusion-reaction problem inside the bubble are the mass conservation of the mixture, the specie conservation of sodium vapor, the energy equation of the mixture and the Laplace equation for pressure. Taking into account equation 5.42:

$$\frac{d}{dr} \rho v r^2 = 0 \quad (5.43)$$

$$\rho v \frac{dY_1}{dr} = M_1 \frac{k \rho^2 Y_1 (1 - Y_1)}{M_1 M_2} (-s_1) + \frac{1}{r^2} \frac{d}{dr} \left(r^2 D \rho \frac{dY_1}{dr} \right) \quad (5.44)$$

$$\rho v c_p \frac{dT}{dr} = -\Delta H_r \frac{k Y_1 (1 - Y_1)}{M_1 M_2} \rho^2 + \frac{1}{r^2} \frac{d}{dr} \left(r^2 \lambda \frac{dT}{dr} \right) \quad (5.45)$$

In addition to these equations, an equation of state for the gas mixture inside the bubble must be added to solve the system:

$$\rho = \left[\frac{RT}{P} \left(\frac{Y_1}{M_1} + \frac{Y_2}{M_2} \right) \right]^{-1} \quad (5.46)$$

In order to solve the system of equations, boundary conditions must be defined for eq. 5.43, 5.44 and 5.45. For eq. 5.44, Y_1 on the bubble surface is the concentration corresponding to the vapor pressure (P_{sat}):

$$\frac{P_{sat}}{P_\infty} = \frac{\frac{Y_{1,sat}}{M_1}}{\frac{Y_{1,sat}}{M_1} + \frac{Y_{2,R}}{M_2}} \quad (5.47)$$

At the same time, a zero CO₂ flux condition must be respected at the bubble surface, that is:

$$\frac{dR}{dt} Y_2 - D \frac{\partial Y_2}{\partial r} = 0 \quad (5.48)$$

At the center of the bubble, spherical symmetry leads that the following Neumann boundary condition must be respected:

$$\left(\frac{\partial Y_1}{\partial r} \right)_{r=0} = 0 \quad (5.49)$$

For equation 5.45, temperature at the bubble center will be the gas temperature, whereas at the bubble surface sodium bulk temperature is taken.

5.2.2 Solving method

The system of equations described in the previous paragraph has been implemented and solve into the Scilab software. Equations 5.43, 5.44 and 5.45 are treated in the same way as described in paragraph 5.1.2. Once algebraical equations have been obtained through finite difference method, the solving algorithm is significantly easier than the one employed in paragraph 5.1.2, since no coupled non-linear equations need to be solved. Therefore, equation 5.44 is solved using a non-linear system $[A(Y_1)] \cdot [Y_1] = [b_{Y_1}]$. Nevertheless, because of the non-linearity in equation 5.44 (Y_1^2), the solution for Y_1 cannot be obtained directly. This problem can be solved treating the non-linear system as a linear system, where the matrix $A(Y_1)$ contains terms which multiply Y_1 , obtained in the previous iteration: the system can be rewritten as $[A(Y_1^{k-1})] \cdot [Y_1] = [b_{Y_1}]$, and it must be solved until convergence is achieved, meaning that at iteration

k the condition $(Y_1^k - Y_1^{k-1}) < \varepsilon$ must be verified. The value of the bubble depletion rate $\frac{dR}{dt}$ is evaluated with equation 5.48.

Once the Y_1 profile is obtained, temperature and density are calculated and the solving process is repeated until the convergence of the global system of equations is achieved, in the same way as detailed in paragraph 5.1.2.

5.2.3 Results

Fixing the reaction rate (that is, the pre-exponential factor k_0 and the activation energy E_a) in the Arrhenius type reaction rate of equation 5.23, the Na and CO₂ mass fractions inside the bubble are calculated. The reaction rate is estimated similarly to the previous droplet reaction rate. In order to keep the same approach employed for the droplet, the reaction rate is evaluated for the sodium (the CO₂ reaction rate is easily determined from the sodium one):

$$\dot{m}_{Na} = \int_{r=0}^{r=R} kY_1Y_2 \frac{\rho^2}{M_2} s_1 \cdot 4\pi r^2 dr = \frac{s_1}{s_2} \frac{M_1}{M_2} \dot{m}_{CO_2} \quad (5.50)$$

Where, in this case, $Y_2 = 1 - Y_1$. Since the reaction rate depends on the bubble radius (different mass fraction profiles are obtained for different bubble radius), equation 5.48 is used to calculate bubble radius after a certain time dt , and a new reaction rate is calculated with equation 5.50 for the smaller bubble radius: in this way, a proper reaction rate is estimated for a number of bubble radius during droplet depletion time. For example, considering the bubble initial diameter of 0.4 mm, five values of reaction rate have been calculated from the initial diameter to the final complete bubble depletion. The mean reaction rate during bubble depletion can be, then, evaluated. The parameter influencing the calculated reaction rate is the sodium temperature, since it establishes the sodium vapor concentration at bulk. Figure 5.12 shows the calculated sodium mass fraction profile inside the bubble, for a sodium temperature of 973 K and a pre-exponential factor of $1 \cdot 10^9 \text{ m}^3 \cdot (\text{mol} \cdot \text{s})^{-1}$. It can be observed how all the sodium vapor is consumed by the reaction in a very narrow region. It must be considered that the bubble dimension is one order of magnitude higher than the sodium droplet, and two orders of magnitude higher than the sodium droplet boundary layer thickness: comparing with results of sodium vapor mass fraction profile inside the droplet boundary layer (reported in figures 5.5 and 5.6), it is consistent to expect that the region where diffusion and reaction occur along the bubble radius is much more confined than inside the sodium droplet boundary. In order to calculate the bubble reaction rate through equation 5.50, the Arrhenius rate must be determined through equation 5.23: similarly to the previous sodium droplet case, the value of the activation energy is supposed known and equal to $4 \cdot 10^4 \text{ J} \cdot \text{mol}^{-1}$, following the results obtained by Gicquel [15]. From this assumption, it follows that the pre-exponential factor is the variable which influences the resulting reaction rate.

As an example, for a pre-exponential factor of $1 \cdot 10^9 \text{ m}^3 \cdot (\text{mol} \cdot \text{s})^{-1}$, figure 5.13 shows the sodium vapor mass fraction profile as a function of sodium temperature, whereas figure 5.14 shows the calculated sodium reaction rate (proportional to the CO₂ reaction rate) of a single bubble, as a function of

the sodium temperature. Figure 5.15 shows the bubble radius depletion as a function of time.

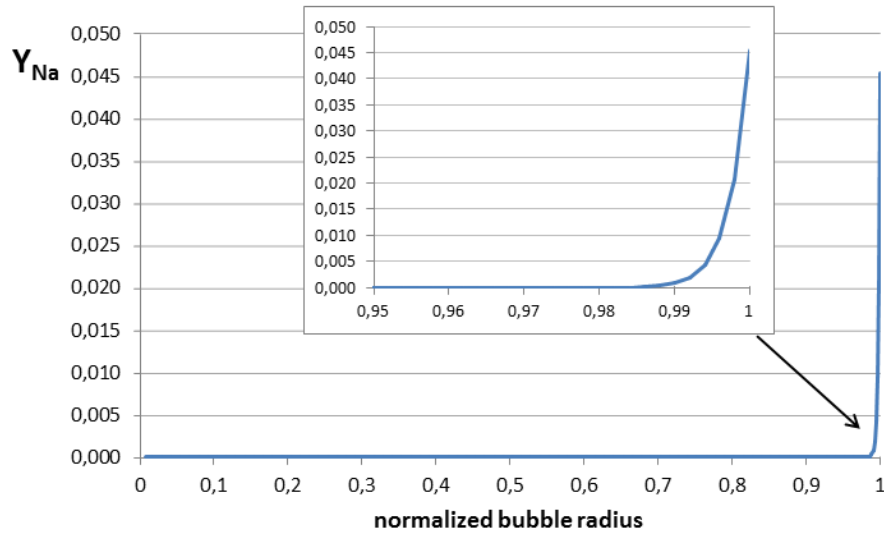


Figure 5.12: Sodium vapor mass fraction profile inside the CO₂ bubble.

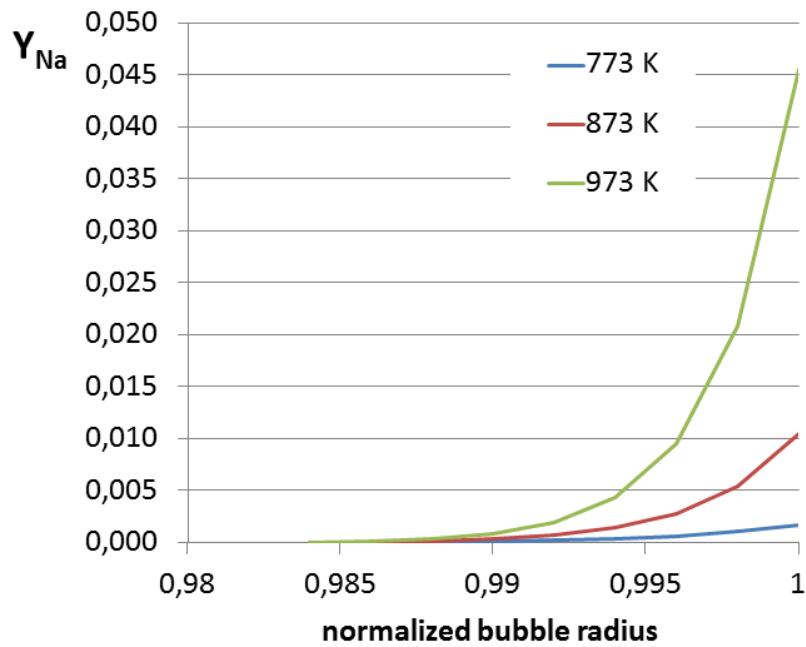


Figure 5.13: Sodium vapor mass fraction profile inside the bubble, as a function of sodium bulk temperature.

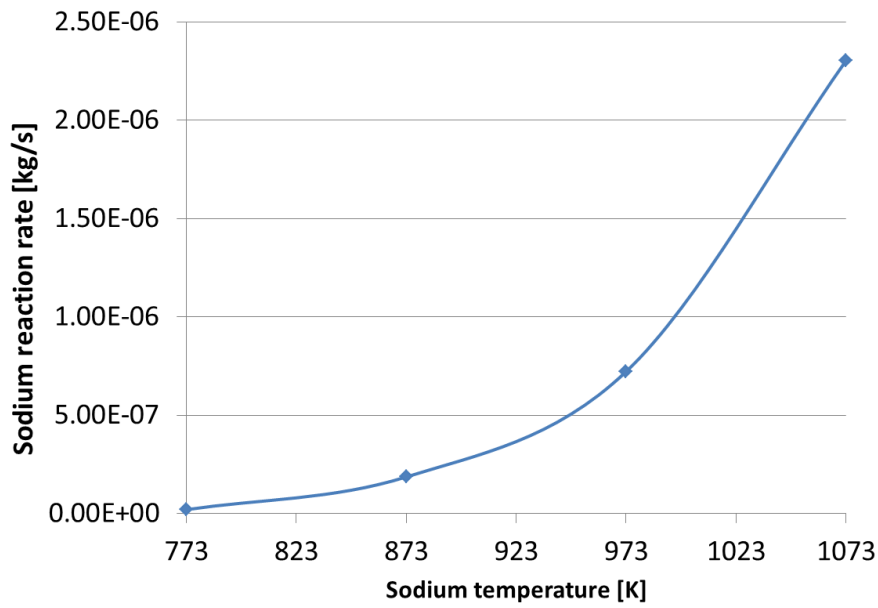


Figure 5.14: Sodium reaction rate for a single bubble, as a function of sodium bulk temperature, for a pre-exponential factor equal to $1 \cdot 10^9 \text{ m}^3 \cdot (\text{mol} \cdot \text{s})^{-1}$.

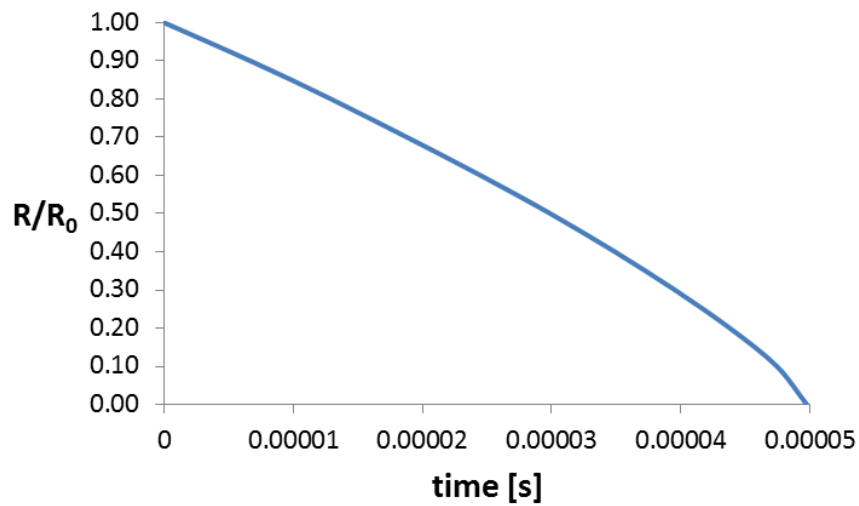


Figure 5.15: Bubble radius as a function of time, for a sodium temperature of 973K and $k_0 = 1 \cdot 10^{10} \text{ m}^3 \cdot (\text{mol} \cdot \text{s})^{-1}$.

5.3 Integral method for depletion rate calculation

In the previous paragraphs 5.1 and 5.2, a model for a sodium droplet reaction with surrounding CO₂ and a model for a CO₂ bubble reaction with surrounding sodium have been developed. The system of differential equations describing the diffusion-reaction mechanism has been solved through a numerical approach: the differential equations have been transformed into algebraic equations through finite difference method, and a numerical method has been applied in order to obtain the solution of the equations. The numerical algorithms are implemented into Scilab. In order to check the consistency of the obtained results, it is interesting to seek for an analytical solution of the system of equations of the reaction models.

The so called “integral method” is a method which allows to obtain an approximated analytical solution of a partial differential equation. The method consists in 1) integrating the differential equation inside the volume of the system, taking into account the boundary conditions, 2) substituting the solution with an approximated form of it (usually, a polynomial function), which must respect the boundary conditions and having only one unknown coefficient, 3) solve this algebraical equation with one unknown.

5.3.1 The integral method for the CO₂ bubble

It is chosen to start with the CO₂ bubble surrounded by liquid sodium, since it is easier to treat than the sodium droplet surrounded by CO₂.

The mass fraction distribution of sodium inside the bubble is described by equation 5.44. Its boundary conditions are represented by equations 5.47, 5.48 and 5.49. The numerical results found in the paragraph 5.2 show that the sodium mass fraction profile is very steep close to the bubble interface, going from $Y_{1,R}$ ($= Y_{1,sat}$) to zero in a very narrow portion of the bubble diameter. This type of trend is difficult to represent through a classical integral method, since the first derivative of the function $Y_1(r)$ changes too abruptly to be represented by a single approximated form of the solution. For this reason, it is chosen to consider only the region where $Y_{1,R} \leq Y_1 \leq Y_{1,R} \rightarrow 0$: inside this region, the integral method is applied, meaning that, once an approximated solution is assumed, the function is integrated inside the spatial limits $r(Y_{1,R}) = R$ and $r(Y_{1,R} \rightarrow 0) = \vartheta$. The following linear approximated solution is taken:

$$Y_1 = Y_{1,R} \left(\frac{r - \vartheta}{R - \vartheta} \right) \quad (5.51)$$

The corresponding profile is shown in figure 5.16.

The final goal is to determine the value of ϑ , in order to compare the results obtained with the integral method to the ones obtained in paragraph 5.2. In order to do that, the approximated solution 5.51 is substituted inside equation 5.44, which is, then, integrated between $r = \vartheta$ and $r = R$. One main simplification employed is that the conservation of energy is not considered and, therefore, the density is constant in the spacial region considered. Moreover, from equation 5.43 it results that:

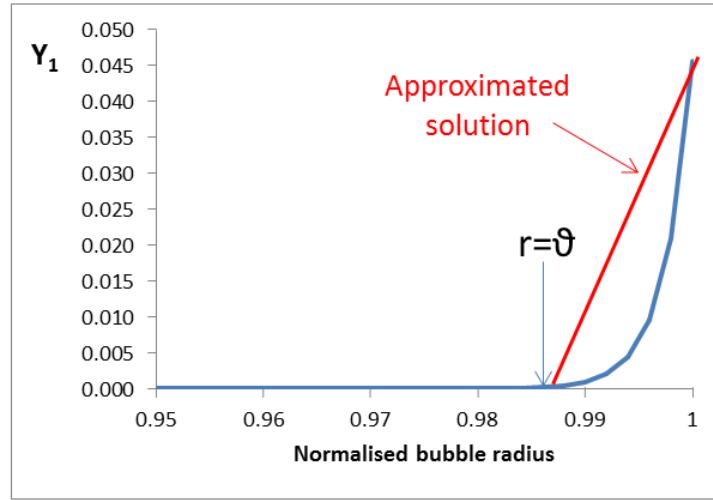


Figure 5.16: Approximated solution employed for the integral approach.

$$r^2 \rho v = R^2 \rho \frac{dR}{dt}$$

Therefore, equation 5.44 can be written as:

$$R^2 \rho \frac{dR}{dt} \int_{\vartheta}^R \frac{dY_1}{dr} dr = \frac{k\rho^2(-s_1)}{M_2} \int_{\vartheta}^R Y_{1,R} \left(\frac{r-\vartheta}{R-\vartheta} \right) \left(1 - Y_{1,R} \left(\frac{r-\vartheta}{R-\vartheta} \right) \right) r^2 dr + \left[r^2 D \rho \frac{dY_1}{dr} \right]_{\vartheta}^R \quad (5.52)$$

The main steps to achieve the solution of equation 5.52 are given in Annex 1. Here, only the final result is reported:

$$R - \vartheta = \left(\frac{DM_2}{k\rho} \right)^{\frac{1}{2}} \left[\frac{2}{\left(1 - \frac{2}{3} Y_{1,R} \right) (1 - Y_{1,R}) (s_1)} \right]^{\frac{1}{2}} \quad (5.53)$$

From equation 5.53, the value of ϑ , as a function of k , can be evaluated.

Some results of the integral method are reported in figure 5.17, where they are compared with the exact calculation, which refers to the calculation performed with numerical method detailed in paragraph 5.2. For different bubble diameters and pre-exponential factors, one can see that the results obtained with the two different numerical approaches are of the same order of magnitude: this represents a confirmation of the consistence of the numerical approach employed in paragraph 5.1.

| R_0 [μm] | k_0 [$\text{m}^3(\text{mol}\cdot\text{s})^{-1}$] | R- ϑ [μm] (integral method) | R- ϑ [μm] (exact calculation) |
|-------------------------|--|---|---|
| 100 | 10^7 | 5.0 | 17.0 |
| 100 | 10^9 | 0.5 | 2.5 |
| 300 | 10^7 | 5.0 | 20.0 |
| 300 | 10^9 | 0.5 | 3.0 |

Figure 5.17: Results obtained with the integral method versus results obtained with the numerical approach described in paragraph 5.1 (“exact calculation”). R_0 is the bubble diameter considered, k_0 the pre-exponential factor of the Arrhenius equation 5.23.

5.3.2 The integral approach for the sodium droplet

We consider equations 5.7 and 5.8: subtracting equations 5.8 from 5.7 and doing some rearrangements, the following equation is obtained:

$$\rho v \frac{dU}{dr} = \frac{1}{r^2} \frac{d}{dr} \left(r^2 \rho D \frac{dU}{dr} \right) \quad (5.54)$$

With $U = M_2 s_2 Y_1 - M_1 s_1 Y_2$. The assumption of constant density and zero velocity ($v = 0$) inside the droplet boundary layer will be taken. Using these assumptions, equation 5.54 can be integrated and solved, using the boundary conditions for Y_1 and Y_2 . The equation obtained for U is:

$$U = (M_2 s_2 Y_{1,R+\delta} - M_1 s_1 Y_{2,R+\delta} - c_2) \frac{R+\delta}{r} + c_2 = (U_{R+\delta} - c_2) \frac{R+\delta}{r} + c_2 \quad (5.55)$$

Substituting 5.55 into 5.8, and integrating, one obtains:

$$\frac{k(-s_2)}{M_2 s_2 M_1} \int_R^{R+\delta} \rho^2 Y_2 \left[M_1 s_1 Y_2 + (U_{R+\delta} - c_2) \frac{R+\delta}{r} + c_2 \right] r^2 dr + \left[r^2 D \rho \frac{dY_2}{dr} \right]_R^{R+\delta} = 0 \quad (5.56)$$

c_2 is an integrating constant. At this point, an approximated solution is assumed for Y_2 . A second order polynomial approximation is chosen:

$$Y_2 = a_0 + a_1 r + a_2 r^2 \quad (5.57)$$

Equation 5.57 must respect the corresponding boundary conditions 5.15 and 5.14, so that the final expression obtained for Y_2 is:

$$Y_2 = Y_{2,\infty} + a_2 \left[(r - R)^2 - \delta^2 \right] \quad (5.58)$$

By using the boundary condition 5.12, one first relation between the c_2 and a_2 constants is deduced. Then, the constant a_2 is obtained by substituting equation 5.58 into 5.56. The steps of the calculation are reported in Annex 2. Finally, the expression for the droplet depletion time can be obtained:

$$\rho_{Na} \frac{dR}{dt} = \frac{\rho D}{M_2 s_2} (c_2 - U_{R+\delta}) \frac{R + \delta}{R^2}$$

Figure 5.18 shows the results obtained for different values of the boundary conditions ($Y_{2,bulk}$, T_{Na} and k_0), compared with the corresponding solution obtained through the numerical method of paragraph 5.1.

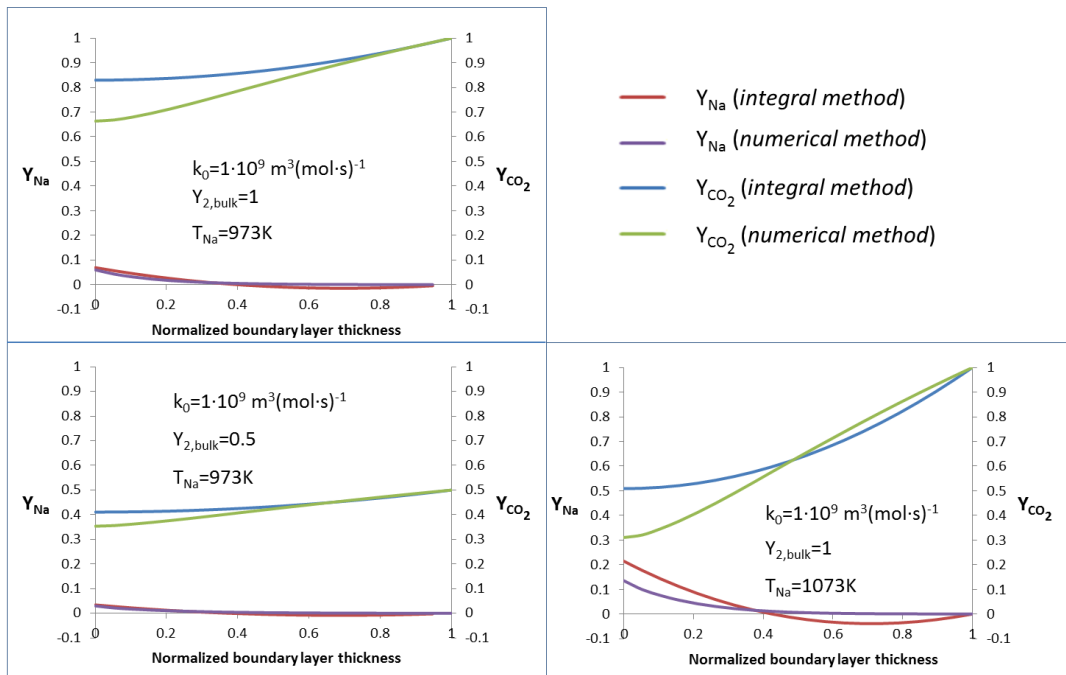


Figure 5.18: Comparison between the mass fraction profiles, inside the boundary layer δ , obtained with the integral approach and with the numerical method.

As one can see from equation 5.39, the gradient of sodium mass fraction in $r = R$ is the parameter influencing the droplet depletion rate. Looking at the results shown in figure 5.18, it is verified that the numerical and the analytical results give a very similar $\left[\frac{\partial Y_1}{\partial r}\right]_R$. Therefore, this gives evidence of the consistency of the obtained results in terms of droplet depletion rate.

Chapter 6

Underexpanded reactive CO₂-into-sodium jet

Nomenclature:

- M : molecular weight [$kg \cdot (kmol)^{-1}$]
- h^f : enthalpy of formation [$kJ \cdot (mol)^{-1}$]
- h : enthalpy [$kJ \cdot (mol)^{-1}$]
- \dot{r} : reaction rate [$kmol \cdot (m^3s)^{-1}$]
- s : stoichiometric coefficient of reaction 6.2
- S : mass transfer source term due to heterogeneous reactions [$kg \cdot (m^3s)^{-1}$]
- U : velocity [$m \cdot s^{-1}$]
- S^U : momentum transfer source term due to heterogeneous reactions [$N \cdot m^{-3}$]
- S^H : energy source term due to heterogeneous reactions [$kJ \cdot (m^3s)^{-1}$]
- Y : mass fraction [$kg \cdot (kg_{tot})^{-1}$]
- ρ : density [$kg \cdot m^{-3}$]
- J : diffusion flux [$kg \cdot (m^2s)^{-1}$]
- D : mass diffusion coefficient [$m^2 \cdot s^{-1}$]
- α : volume fraction [-]
- \dot{m} : particle reaction rate [$kg \cdot s^{-1}$]
- T : temperature [K]
- N : number of particle per unit volume [m^{-3}]
- X : number of moles per unit volume [$kmol \cdot m^{-3}$]

- k : molar kinetic constant [$m^3 \cdot (mol \cdot s)^{-1}$]
- D : diffusion coefficient [$m^2 \cdot s^{-1}$]
- T : temperature [K]
- k_0 : pre-exponential factor of the Arrhenius law [$m^3 \cdot (mol \cdot s)^{-1}$]
- γ : ratio between gas heat capacities (c_p/c_v)

Subscripts:

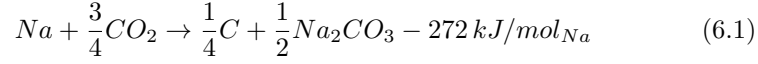
- p : relative to the generic phase p
- l : relative to the liquid phase
- g : relative to the gas phase
- i : relative to the generic species i
- d : droplet
- b : bubble

In chapter 4, the modeling approach developed for a non-reactive underexpanded gas-into-liquid has been presented. In chapter 5, a model for taking into account the chemical reaction between sodium and CO₂ in a corresponding CO₂-into-sodium jet has been developed. Considering the final goal of the present work, the last step to accomplish is the coupling of the non-reactive jet and the chemical reaction models, in order to obtain a complete numerical description of the underexpanded CO₂-into-liquid-sodium reactive jet. Doing this, numerical results on temperature distribution inside the jet would be obtained and, through the comparison with the experimental results, information about the CO₂-Na reaction kinetics could be derived. In the present chapter, the approach employed for the modeling of a reactive underexpanded CO₂-into-Na will be described, and the results will be presented.

6.1 Modeling approach

In paragraph 4.1.2, the equations employed for the modeling of an underexpanded non-reactive gas-into-liquid jet have been detailed. In order to couple the chemical reaction model with the non-reactive jet model, the idea is to add source terms inside the two-fluid model equations (equations 4.7, 4.8 and 4.9). These source terms have to take into account the influence of the chemical reaction between CO₂ and Na, in terms of mass, momentum and energy production/destruction for each phase.

As detailed in chapter 5, the following reaction path is considered in the present work:



As it can be seen, liquid sodium and gaseous carbon dioxide produce carbon and sodium carbonate. Carbon is a solid product, whereas the Na_2CO_3 fusion point is 851°C. In order not to further complicate the numerical approach, the main assumption is made that the products of reaction and liquid sodium belong to a unique condensed phase: the addition of a third, solid, phase would significantly increase the complexity of the numerical approach formulation. Following this assumption, reaction 6.1 can be rewritten as:



Where P_{liq} represents the total amount of reaction products, in liquid phase. Reaction 6.2 is equivalent to 6.1 provided that, besides the assumption that all the reaction products are in liquid phase, the molar mass of P is equal to the effective molar mass of the carbon and sodium carbonate mixture of reaction 6.1, and that the enthalpy of formation of P is such that the enthalpy of reaction of 6.2 is equal to the one of the reaction 6.1. Therefore, the molecular mass and the enthalpy of formation of P can be evaluated as follows:

$$M_P = \frac{1}{4}M_C + \frac{1}{2}M_{Na_2CO_3} = 56 \frac{kg}{kmol}$$

$$\frac{3}{4}h_{CO_2}^f - h_P^f = 272 \frac{kJ}{mol} \Leftrightarrow h_P^f = -567 \frac{kJ}{mol}$$

Where h_i^f is the enthalpy of formation of the species i , at thermodynamic standard conditions.

6.1.1 Mass transfer due to chemical reaction

Let's consider the continuity equation for the phase p , equation 4.7. The source term S_p takes into account the mass transfer caused by the production or destruction of the phase p , due to an heterogeneous chemical reaction. If the chemical reaction produces species in the phase p , then S_p will be positive; if the chemical reaction leads to the production of species only in the phase q , then S_p will be negative. At the same time, since the total mass of the two-phase system must be conserved, a source term S_q of phase q , such that $S_q = -S_p$, must be added in the continuity equation of phase q . The general form of the mass transfer for the phase p is given by:

$$S_p = \dot{r} \left(\sum_{pr_p} s_{pr_p} M_{pr_p} - \sum_{r_p} s_{r_p} M_{r_p} \right) \quad (6.3)$$

Where \dot{r} , s and M are, respectively, the reaction rate in $kmol \cdot (m^3s)^{-1}$, the stoichiometric coefficient and the molecular mass. The subscript r_p stands for the reactant r of the phase p and the subscript pr_p stands for product pr of the phase p . Considering the specific reaction path 6.2, and employing subscripts l and g for the liquid and gas phase, respectively, the mass source terms for the two phases will be:

$$S_l = \dot{r} (M_P - M_{Na}) \quad (6.4)$$

$$S_g = \dot{r} \left(-\frac{3}{4} M_{CO_2} \right) \quad (6.5)$$

It can be verified that $S_l = -S_g$, as expected.

6.1.2 Momentum transfer due to chemical reaction

In the momentum equation 4.8 for the phase p , the term $S_p^{\vec{U}}$ takes into account the momentum transfer due to heterogeneous chemical reactions. For momentum transfer, the approach employed by Ansys Fluent [70] is adopted. It is assumed that the reactants mixture and the products take momentum in the ratio of the rate of their formation. The general expression of the net velocity, \vec{U}_{net} , of the reactants is given by:

$$\vec{U}_{net} = \frac{\sum_r s_r M_r \vec{U}_r}{\sum_r s_r M_r} \quad (6.6)$$

Where U_r is the velocity of the reactant r . The general expression for the momentum transfer for the phase p is:

$$S_p^{\vec{U}} = \dot{r} \left(\sum_{pr_p} s_{pr_p} M_{pr_p} \vec{U}_{net} - \sum_{r_p} s_{r_p} M_{r_p} \vec{U}_{r_p} \right) \quad (6.7)$$

For the specific reaction path 6.2 considered, equations 6.6 and 6.7 become:

$$\vec{U}_{net} = \frac{M_{Na} \vec{U}_l + \frac{3}{4} M_{CO_2} \vec{U}_g}{M_{Na} + \frac{3}{4} M_{CO_2}} \quad (6.8)$$

$$S_l^{\vec{U}} = \dot{r} (M_P \vec{U}_{net} - M_{Na} \vec{U}_l) \quad (6.9)$$

$$S_g^{\vec{U}} = \dot{r} \left(-\frac{3}{4} M_{CO_2} \vec{U}_g \right) \quad (6.10)$$

6.1.3 Heat transfer due to chemical reaction

Considering the energy equation 4.9 for the phase p , the term S_p^H takes into account the heat transfer due to heterogeneous chemical reactions. In order to calculate this term, the approach employed by Ansys Fluent [70] is adopted. Let's consider the net enthalpy of the reactants, which is given by:

$$h_{net} = \frac{\sum_r s_r M_r h_r^f}{\sum_r s_r M_r} \quad (6.11)$$

It is assumed that this net enthalpy is distributed to the products in the ratio of their mass production rates. Therefore, the heat transfer for the phase p is given by:

$$S_p^H = \dot{r} \left(\sum_{pr_p} s_{pr_p} M_{pr_p} h_{net} - \sum_{r_p} s_{pr_p} M_{pr_p} h_{pr_p}^f \right) \quad (6.12)$$

For the specific reaction path 6.2, equations 6.11 and 6.12 become:

$$h_{net} = \frac{M_{Na} h_{Na}^f + \frac{3}{4} M_{CO_2} h_{CO_2}^f}{M_{Na} + \frac{3}{4} M_{CO_2}} \quad (6.13)$$

$$S_l^H = \dot{r} \left(M_P h_{net} - M_P h_P^f \right) \quad (6.14)$$

$$S_g^H = 0 \quad (6.15)$$

6.1.4 Species transport equation

When a chemical reaction is considered, new species are created: in the present case, following reaction path 6.2, it can be observed that two species exist in the liquid phase, that is Na and P . A transport equation for these species is, therefore, required in order to predict the local mass fraction of each species, in the liquid phase. The number of species transport equations to be solved corresponds to $N_{species} - 1$, because the local mass fraction of the last species can be obtained through the equation:

$$\sum_{i,p} Y_{i,p} = 1 \quad (6.16)$$

Where $Y_{i,p}$ is the mass fraction of species i inside the phase p . For the present case, this means that only one species transport equation is required for the liquid Na and P mixture. The generalized species conservation equation for a multiphase mixture can be written in the following form:

$$\frac{\partial}{\partial t} (\alpha_p \rho_p Y_p) + \nabla \cdot (\alpha_p \rho_p \vec{U}_p Y_{i,p}) = -\nabla \cdot \alpha_p \vec{J}_{i,p} + S_{i,p} \quad (6.17)$$

In 6.17, \vec{J}_i is the diffusion flux of species i inside the phase p and $S_{i,p}$ is the source term accounting for production or destruction of species i in the phase p , due to chemical reaction. In Ansys Fluent, the Fick's law is used to model mass diffusion due to concentration gradients, under which the diffusion flux can be written as:

$$\vec{J}_i = -\rho D_{i,p} \nabla Y_i$$

Where D_i is the mass diffusion coefficient of species i in the mixture of phase p .

For the Na and P liquid mixture, it is chosen to solve the transport equation for the Na species. The mass diffusion coefficient of Na inside the liquid mixture has been fixed to $10^{-9} m^2 s^{-1}$, a typical value for mass diffusion coefficient in liquids. The source term taking into account the chemical reaction will be:

$$S_{Na,l} = -\dot{r} M_{Na} \quad (6.18)$$

6.2 Implementation of the chemical reaction into the two-fluid model

In the previous paragraph, the source terms to be added to the two-fluid Euler-Euler approach, in order to take into account the chemical reaction between phases, have been detailed: all these terms depend on the reaction rate \dot{r} . The reaction rate, for the specific $Na - CO_2$ interactions occurring in an underexpanded reactive CO₂-into-Na jet, has been calculated in chapter 5. Specifically, sodium reaction rate for a single sodium-droplet inside gaseous CO₂, and for a CO₂ bubble inside liquid sodium, have been determined. This "single-particle" reaction rate are, now, employed in order to calculate the source terms (equations 6.4, 6.5, 6.9, 6.10, 6.14, 6.15, 6.18) to be added to the continuity, momentum, energy and species equations for taking into account the heterogeneous chemical reaction 6.2.

In Ansys Fluent, a specific User Define Function (called "DEFINE_HET_RXN_RATE") can be employed for defining a user defined chemical reaction rate. Once the reaction rate is calculated inside this function, Ansys Fluent uses it to calculate to source terms 6.4, 6.5, 6.9, 6.10, 6.14, 6.15 and 6.18. In order to do that, also the enthalpy of formation and the stoichiometric coefficient of every species must be defined inside Ansys Fluent.

In a CFD approach, the reaction rate to be provided for the evaluation of the different source terms, has the unit of $kmol \cdot (m^3 s)^{-1}$, where the m^3 refer to

the computational cell volume. Since, in the considered two-phase flow, droplet flow and bubbly flow coexist, a similar approach to the one employed for the calculation of the interfacial drag force and heat transfer is employed also for the evaluation of the reaction rate inside a single computational cell: if, inside the cell, $\alpha \geq \alpha_d$, then only droplets inside continuous CO₂ are considered for the evaluation of the reaction rate; if $\alpha < \alpha_b$, then only CO₂ bubble inside continuous liquid sodium are assumed for the evaluation of the reaction rate; for the transition flow between α_d and α_b , a transition reaction rate must be evaluated.

6.2.1 Reaction rate for droplet flow ($\alpha \geq \alpha_d$)

The reaction rate of a single sodium droplet has been calculated in chapter 5. The numerical method developed for this calculation cannot be directly implemented inside the calculation procedure of Ansys Fluent: in fact, the calculation of a droplet reaction rate for a single set of boundary conditions (sodium temperature and CO₂ bulk concentration) requires too long computational time to be performed for each cell of the numerical domain, for each time step. Therefore, data obtained in chapter 5 are used to build a correlation for the evaluation of the reaction rate, as a function of sodium (droplet) temperature (T_{Na}) and CO₂ concentration at the bulk ($Y_{CO_2,bulk}$). The following correlation has been found to well represent the reaction rates numerically calculated:

$$\dot{m}_{Na,droplet} \left[\frac{kg}{s} \right] = (A \cdot T_{Na}^3 + B \cdot T_{Na}^2 + C \cdot T_{Na} + D) \cdot (Y_{CO_2,bulk})^{0.4} \quad (6.19)$$

Where the coefficients A, B, C and D depend on the pre-exponential factor employed in the Arrhenius equation 5.23.

As an example, figure 6.1 shows the correlation compared to the exact calculation, for different values of sodium temperature and CO₂ mass fraction at bulk, for a pre-exponential factor of $1 \cdot 10^9 \text{ m}^3 \cdot (\text{mol} \cdot \text{s})^{-1}$.

In order to evaluate the total reaction rate inside a computational cell, the total number of droplet per unit volume, N_d , must be calculated:

$$N_d \left[\frac{1}{m^3} \right] = \frac{V_{Na,cell}}{V_d} = \frac{\frac{Y_{Na,l}}{\rho_{Na}} \rho_l \alpha_l}{\frac{4}{3} \pi \left(\frac{d_d}{2} \right)^3} \quad (6.20)$$

Where $V_{Na,cell}$ is the sodium to the total cell volume ratio, $Y_{Na,l}$ is the Na mass fraction in the liquid phase. Furthermore, the CO₂ concentration at bulk must be evaluated in order to calculate the reaction rate. Inside a computational cell, droplet can be imagined as surrounded by CO₂ and reaction products. The CO₂ at the bulk does not correspond to CO₂ mass fraction inside the computational cell, but to the CO₂ concentration inside the mixture (CO₂ and products P) surrounding the droplets. Considering that, for every cell, $Y_{CO_2} + Y_{Na} + Y_P = 1$, the CO₂ mass concentration at the droplet bulk can be calculated as follows:

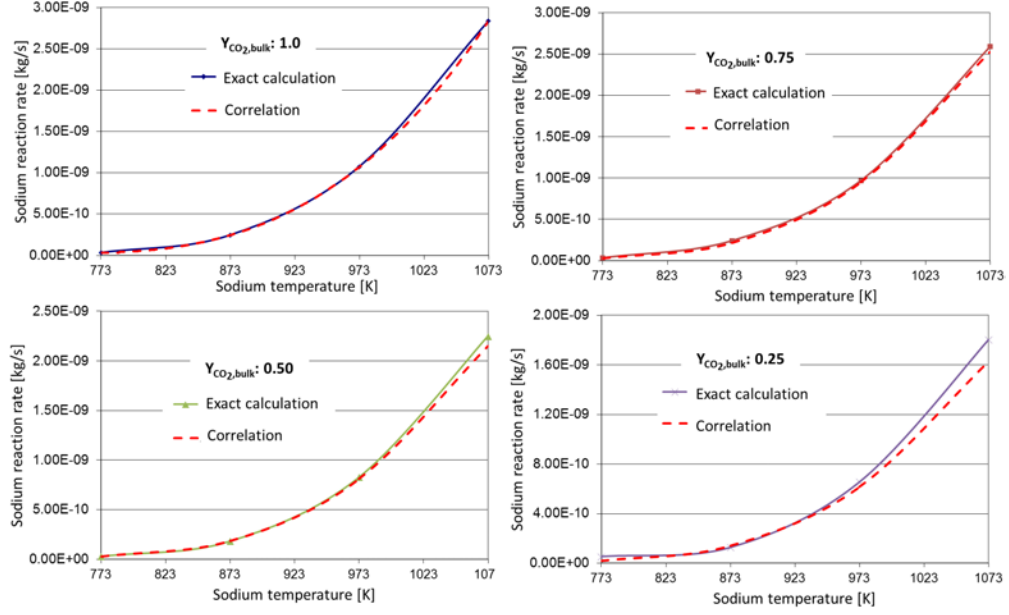


Figure 6.1: Comparison between exact numerical results and the correlation 6.19, for a pre-exponential factor of $1 \cdot 10^9 m^3 \cdot (mol \cdot s)^{-1}$. For this value, the coefficients in equation 6.19 are equal to: $A = 5.4619 \cdot 10^{-17}$, $B = -1.1221 \cdot 10^{-13}$, $C = 7.5665 \cdot 10^{-11}$, $D = -1.6635 \cdot 10^{-8}$.

$$Y_{CO_2,bulk} = \frac{Y_{CO_2}}{Y_{CO_2} + Y_P} = \frac{Y_{CO_2}}{1 - Y_{Na}} \quad (6.21)$$

Through equations 6.19, 6.20 and 6.21, the reaction rate per unit volume can be calculated:

$$\dot{r}_{Na,droplet_{total}} \left[\frac{kmol}{m^3 s} \right] = \frac{N_d \cdot \dot{m}_{Na,droplet}}{M_{Na}} \quad (6.22)$$

The reaction rate obtained through equation 6.22 is realizable provided that enough CO₂, compared to the stoichiometry, is available inside the computational cell. The number of moles of CO₂, X_{CO_2} , inside the cell can be evaluated as:

$$X_{CO_2} \left[\frac{kmol}{m^3} \right] = \alpha_g \frac{\rho_{CO_2}}{M_{CO_2}} \quad (6.23)$$

It follows that the actual reaction rate, $\dot{r}_{eff,droplet}$, inside the computational cell must be evaluated as follows:

$$\dot{r}_{eff,droplet} \left[\frac{kmol_{Na}}{m^3s} \right] = \min \left(\dot{r}_{Na,droplet_{total}}, \frac{\gamma_{Na}}{s_{CO_2}} \frac{X_{CO_2}}{\Delta t} \right) \quad (6.24)$$

Where Δt is the current time step of calculation.

6.2.2 Reaction rate for bubbly flow ($\alpha \leq \alpha_b$)

Similarly to the case of droplet flow, also for the bubbly flow the results obtained in chapter 5 are used to build a correlation for the evaluation of the reaction rate. As detailed in paragraph 5.2, the bubble reaction rate depends only on the sodium temperature. The following type of equation has been found to well correlate the numerical results:

$$\dot{m}_{Na,bubble} \left[\frac{kg}{s} \right] = (A' \cdot T_{Na}^3 + B' \cdot T_{Na}^2 + C' \cdot T_{Na} + D') \quad (6.25)$$

In order to keep the similarity between the two cases, the reaction rate refers to the quantity of sodium consumed, and not to the CO₂, also for the bubble. The coefficients A' , B' , C' and D' depend on the pre-exponential factor employed in the Arrhenius equation 5.23. As an example, figure 6.2 shows the comparison between the correlation and the exact numerical results, for the case of a pre-exponential factor of $1 \cdot 10^9 m^3 \cdot (mol \cdot s)^{-1}$.

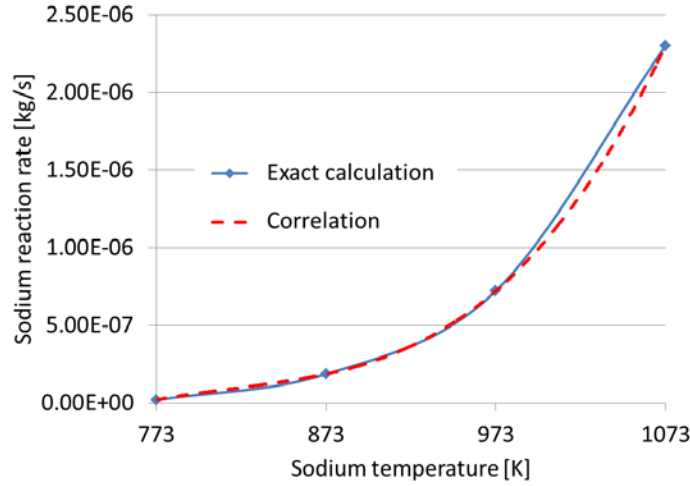


Figure 6.2: Comparison between exact numerical results and the correlation 6.25, for a pre-exponential factor of $1 \cdot 10^9 m^3 \cdot (mol \cdot s)^{-1}$. For this value, the coefficient in equation 6.25 are equal to: $A = 1.1264 \cdot 10^{-13}$, $B = -2.7654 \cdot 10^{-10}$, $C = 2.2768 \cdot 10^{-7}$, $D = -6.2764 \cdot 10^{-5}$.

In order to evaluate the total reaction rate inside a cell, the total number of bubble per unit volume, N_b , must be calculated:

$$N_b \left[\frac{1}{m^3} \right] = \frac{V_{CO_2,cell}}{V_b} = \frac{\alpha}{\frac{4}{3}\pi \left(\frac{d_b}{2}\right)^3} \quad (6.26)$$

Through equations 6.25 and 6.26, the reaction rate per unit volume can be calculated:

$$\dot{r}_{Na,bubble_{total}} \left[\frac{kmol}{m^3s} \right] = \frac{N_b \cdot \dot{m}_{Na,bubble}}{M_{Na}} \quad (6.27)$$

The reaction rate obtained through equation 6.27 is realizable provided that enough CO₂, compared to the stoichiometry, is available inside the computational cell. The number of moles of CO₂, X_{CO_2} , inside the cell can be evaluated through equation 6.23. It follows that the actual reaction rate, $\dot{r}_{eff,bubble}$, inside the computational cell must be evaluated as follows:

$$\dot{r}_{eff,bubble} \left[\frac{kmol_{Na}}{m^3s} \right] = \min \left(\dot{r}_{Na,bubble_{total}}, \frac{s_{Na}}{s_{CO_2}} \frac{X_{CO_2}}{\Delta t} \right) \quad (6.28)$$

Where Δt is the current time step of calculation.

6.2.3 Reaction rate for the transition flow ($\alpha_b < \alpha < \alpha_d$)

For void fractions between α_b and α_d , the same approach employed for the drag force and heat transfer calculation has been employed: the reaction rate is continuously interpolated between the reaction rate at α_b and the reaction rate at α_d , using a logarithmic average.

The number of droplets and bubbles inside a computational cell where the condition $\alpha_b < \alpha < \alpha_d$ is verified, is given, respectively, by:

$$N_{d,transition} \left[\frac{1}{m^3} \right] = \frac{V_{Na,cell_{droplet}}}{V_d} = \frac{\frac{Y_{Na,l}}{\rho_{Na}} \rho_l (1 - \alpha_d)}{\frac{4}{3}\pi \left(\frac{d_d}{2}\right)^3} \quad (6.29)$$

$$N_{b,transition} \left[\frac{1}{m^3} \right] = \frac{V_{CO_2,cell_{bubbly}}}{V_b} = \frac{\alpha_b}{\frac{4}{3}\pi \left(\frac{d_b}{2}\right)^3} \quad (6.30)$$

Where $V_{Na,cell_{droplet}}$ is the effective volume of sodium represented by droplet flow, and $V_{CO_2,cell_{bubbly}}$ is the effective volume of CO₂ represented by bubbly flow. The corresponding reaction rate for the droplet and bubbly flows are, respectively:

$$\dot{r}_{Na,droplet_{transition}} \left[\frac{kmol}{m^3s} \right] = \frac{N_{d,transition} \cdot \dot{m}_{Na,droplet}}{M_{Na}} \quad (6.31)$$

$$\dot{r}_{Na,bubble_{transition}} \left[\frac{kmol}{m^3s} \right] = \frac{N_{b,transition} \cdot \dot{m}_{Na,bubble}}{M_{Na}} \quad (6.32)$$

The reaction rate for a generic void fraction α , when $\alpha_b < \alpha < \alpha_d$, is estimated as follows:

$$\dot{r}_{transition} = exp \left[x_b \log (\dot{r}_{Na,bubble_{transition}}) + x_d \log (\dot{r}_{Na,droplet_{transition}}) \right] \quad (6.33)$$

Since the calculated reaction rate is realizable only if enough CO₂, compared to the stoichiometry, is available in the computational cell, it follows that the actual reaction rate for the transition regime is evaluated as:

$$\dot{r}_{eff,transition} \left[\frac{kmol_{Na}}{m^3s} \right] = \min \left(\dot{r}_{Na,bubble_{total}}, \frac{s_{Na}}{s_{CO_2}} \frac{X_{CO_2}}{\Delta t} \right) \quad (6.34)$$

Where Δt is the current time step of calculation.

6.3 Results

6.3.1 Preliminary considerations on experimental results

The available experimental results concern the temperature distribution inside the jet. The temperature profile along the jet centerline, obtained by Gicquel, for the SCR, and by Sekkouti, for the SWR, are reported in figures 6.4 and 6.3, respectively. The results obtained by Gicquel and Sekkouti are not qualitatively similar. Gicquel found a sudden temperature rise of more than 800°C very close to the nozzle (at an axial distance of 4.3 nozzle diameters), followed by a sudden decrease of the measured temperature, which at 7.1 nozzle diameters is already 670°C lower than at 4.3 nozzle diameters. Starting from this point, the temperature further decreases very slowly along the axial distance. For the same gas injection pressure, the temperature profile obtained by Sekkouti is more regular than the one obtained by Gicquel: the measured temperature increases along the jet centerline, until reaching its maximum at a distance corresponding to 12 nozzle diameters, which is three times the distance where the maximum temperature value was found by Gicquel. Starting from the maximum temperature, Sekkouti found a much smoother decrease of the measured temperature along the centerline, than Gicquel. Moreover, another main difference is represented by the fact that the maximum temperature measured by Gicquel lies in a very narrow region (corresponding to only two experimental measures, at an axial distance of 4.3- and 5.7-nozzle-diameters), whereas the measurements performed by Sekkouti show that the temperature keeps close to its maximum value in a region starting at about 10 nozzle diameters and ending at about 25 nozzle diameters.

Giving a proper interpretation to the results obtained by Gicquel and Sekkouti is a complicate task. As already discussed in paragraph 2.1.1.3, one main critical aspect concerning temperature measurements, using thermocouples,

inside high-speed gas flows is the fact that the thermocouple is supposed to always measure a stagnation temperature. For example, if one considers the measurement performed at 4.3 nozzle diameters, the numerical results reported in paragraph 4.2.2 show that gas Mach number, in this region, is still equal or higher than one. The total to static temperature ratio can be evaluated with the following isentropic equation:

$$\frac{T_{tot}}{T_{st}} = 1 + \frac{\gamma - 1}{2} M^2 \quad (6.35)$$

Through equation 6.35, one can verify that the static temperature is 87 per cent of the total temperature, in the case of $M=1$, and 75 per cent of the total temperature, if $M=1.5$. Therefore, in both the results obtained by Gicquel and Sekkouti, this phenomenon must be taken into account, meaning that the actual static temperature inside the jet is lower than the measured value, above all in the region very close to the nozzle.

Not only the measured temperature is the total value, but an additional heating to the thermocouple may have to be considered. In the field of aerospace engineering, the ability to accurately predict surface heating rates has proven to be one of the most significant issues to the design of hypersonic re-entry vehicles. Convective heating that occurs in the boundary layer adjacent to the body as the vehicle passes through the surrounding atmosphere is due to frictional forces because the kinetic energy of the flow is dissipated into internal energy, as viscous dissipation. However, this heating is compounded by what is known as shock-wave heating which occurs from the hot compressed gas ahead of the vehicle and behind the very strong shock that forms as a result from the extreme velocities reached during reentry [71]. This issue is also referred to as “stagnation point heat transfer” [72]. Even if the Mach numbers reached during space re-entry are higher than the ones obtained in the underexpanded jets here considered, an analogy can be made between the thermocouple tip inserted inside a high Mach gas flow and a space vehicle moving at high Mach speed inside the atmosphere. One of the most accurate equation for the calculation of the stagnation heat flux is the one developed by Fay and Riddell [73]. It is not the scope of this work to achieve a detailed analysis of the stagnation point heat transfer in a thermocouple-gas-flow interaction. However, the existence of this issue must be considered in order to evaluate the consistency of the measured temperatures.

Another important aspect to consider, regarding experimental temperature results obtained by Gicquel and Sekkouti, is the geometry of the comb of thermocouples employed: both the authors used a comb of thermocouples of big dimensions, compared to the nozzle diameter. The comb of thermocouples employed by Gicquel has been described in paragraph 3.1.1: its width is about 80 mm, with a thickness of about 2 mm. This means that, in the case of placing it at 3 mm from the nozzle, the gas flow exiting the nozzle is significantly perturbed by the presence of the comb. The same considerations are valid for the tests performed by Sekkouti, since the type of thermocouple comb was similar to the one employed by Gicquel.

From the previous considerations, one can understand the difficulty in trusting a thermocouple measurement of a temperature at 3 nozzle diameters down-

stream the nozzle, due to the high gas speed and to the important flow perturbation caused by the physical presence of the comb.

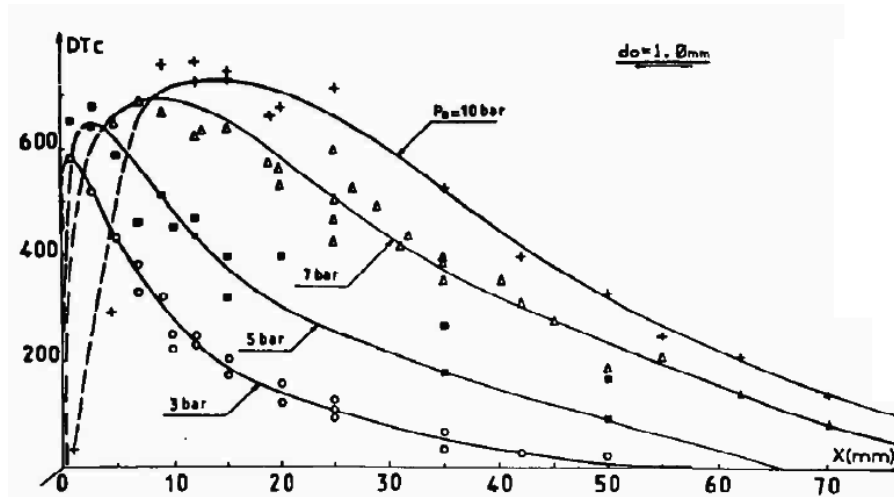


Figure 6.3: Temperature profile along the jet axis measured by Sekkouti [23]. DT_C represents the difference between the measured temperature and the sodium temperature in the pool far away from the jet.

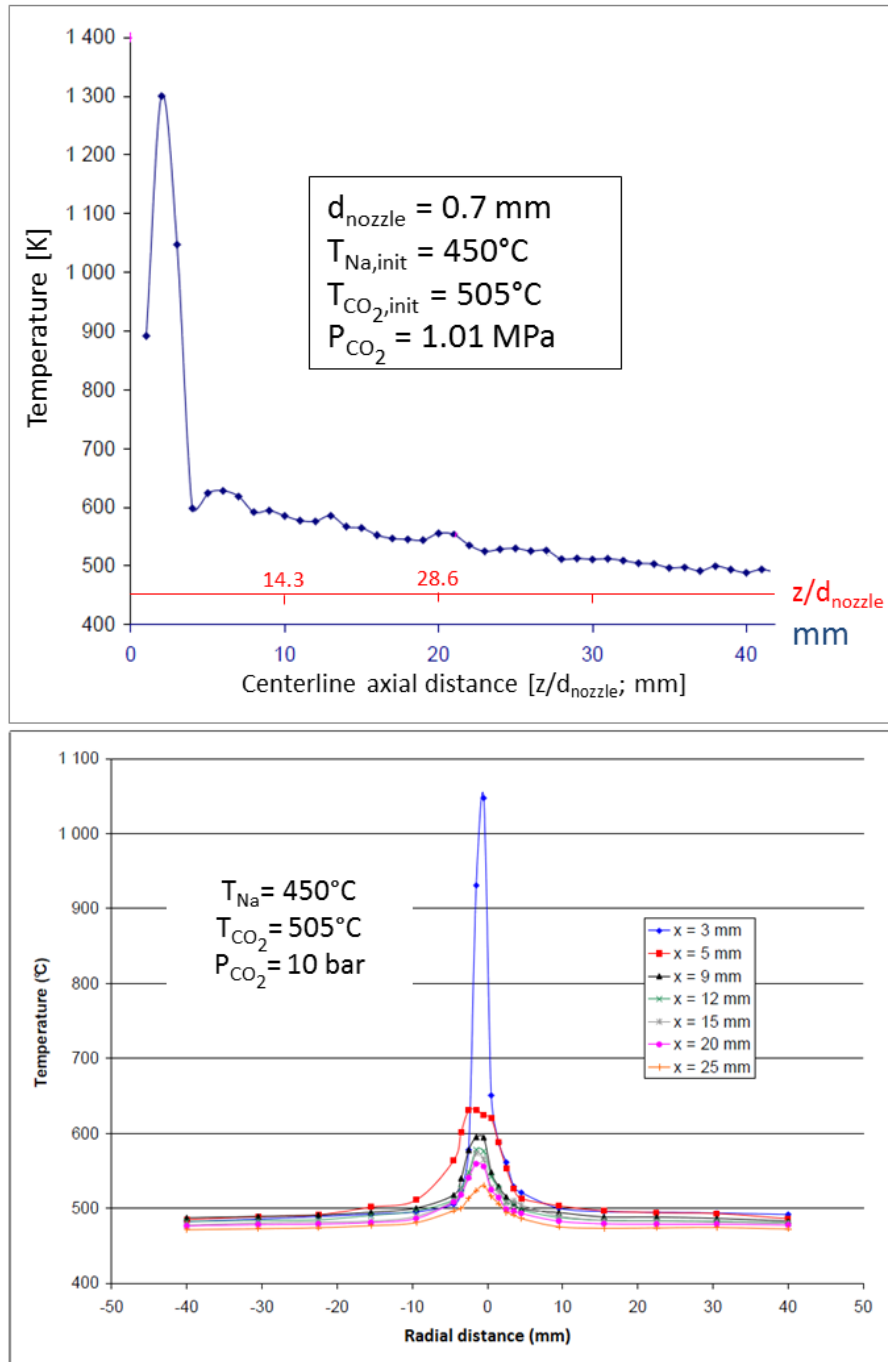


Figure 6.4: Axial and radial temperature profiles measured by Gicquel [15], for a sodium initial temperature of 450°C.. x stands for the axial distance from the nozzle, which had a diameter of 0.7 mm.

6.3.2 Numerical results and validation

6.3.2.1 Numerical details

Since the numerical results will be compared to the experimental ones obtained using the experimental facility described in 3.1.1, the computational domain employed corresponds to the same computational domain employed for the simulations of the non-reactive N₂-into-water jet, detailed in chapter 4. This geometry corresponds to the experimental pool filled with liquid-sodium, where the CO₂ is injected and the CO₂-into-sodium jet is realized. The same computational mesh of chapter 4 has been retained also for the simulations of reactive jets. The finest of the two meshes tested in chapter 4 was employed: it features 98,000 cells.

The same kind of boundary conditions adopted for the non-reactive jet simulations, described in chapter 4, were employed for the simulations of reactive jets. Of course, gas and liquid properties have been changed, from nitrogen and water, to carbon dioxide and liquid sodium. CO₂ was considered as a compressible gas with an ideal gas law, whereas liquid sodium was treated as incompressible. Since sodium density depends on temperature, and the present calculations are expected to feature significant spatial temperature variations (due to the exothermic reaction), a mean sodium density was employed. The initial sodium temperature considered is 500°C, corresponding to the operative temperature inside the heat exchanger in the considered region: at 500°C, sodium density is 830 kg/m³. Following the experimental results obtained by Gicquel, described in 2.2, the reaction is supposed to lead to rise in temperature of several degrees: a mean temperature of 600°C was retained for fixing the sodium density, which, at this temperature, is equal to 800 kg/m³.

As already discussed in chapter 4, the numerical stability of a two-fluid computation of an underexpanded gas-into-liquid jet is a critical aspect, mainly due to the high Mach numbers reached. The addition of source terms in each equation, for taking into account the heterogeneous chemical reaction, further increases the complexity of the numerical formulation. One direct consequence is the fact that numerical convergence could not be obtained adopting second order spatial discretization for the numerical simulations. Therefore, first order upwind had to be adopted for the spatial discretization of each equation.

The reaction was implemented inside the numerical calculation using the Stiff Chemistry Solver, available in Ansys Fluent: for each time step, all the equations are first solved spatially with the reaction term (equation 6.24 or 6.28 or 6.34) set to zero; in the second fractional step, the reaction term is integrated in every cell using a stiff Ordinary Differential Equation solver. This method has shown to guarantee a higher numerical stability than the case of directly taking into account the reaction rate in the calculation.

6.3.2.2 Numerical results

For the numerical simulations, sodium initial temperature was fixed to 500°C. From figure 5.1, the corresponding CO₂ temperature, in the section of the heat exchanger where sodium is at 500°C, is about 475°C. Therefore, this is the CO₂ stagnation injection temperature employed. Since the experimental results obtained by Gicquel and Sekkouti [15, 23], used for the numerical-experimental

comparison, were performed at a CO₂ total pressure of 1.00 MPa, this was the total pressure employed for the CO₂ injection in the numerical simulation.

Figure 6.5 shows the numerical temperature profile obtained on the jet centerline, for different values of the pre-exponential factor k_0 of equation 5.23.

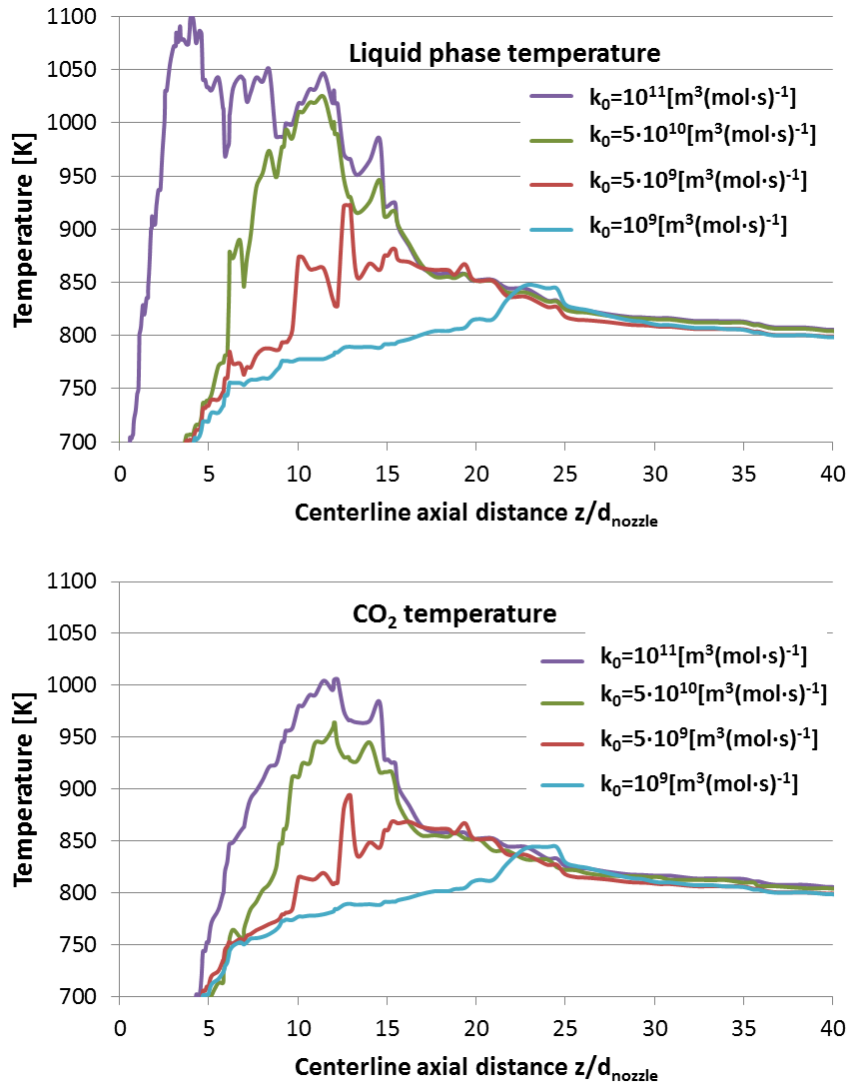


Figure 6.5: Liquid and gas phase static temperature along the jet centerline, as a function of the chemical reaction rate (through the pre-exponential factor k_0).

One can see that, as expected, the increasing of the chemical reaction rate leads to a shift of the maximum temperature peak towards the nozzle. As expected, the liquid phase temperature is higher than the gas phase temperature, since no

enthalpy is transferred to the gas phase by the chemical reaction (the source term 6.15 is zero). It is the liquid phase that heats the gas phase, through the interfacial heat transfer described in equation 4.30. The irregular shape of the calculated profile is due to the tetrahedral mesh, which is cut by the jet centerline axis in different regions of different cells. It has to be recalled that Fluent stores the temperature (and also all the other variables, pressure included) values at the cell centers. Therefore, the reported centerline temperatures in figure 6.5 correspond to the cell center values of the cells encountered along the axial centerline.

The maximum temperature found by Gicquel was 1300K, corresponding to a rise of about 550K, considering the initial sodium and CO₂ temperatures. The static temperature corresponds to about the 80% of the stagnation 1300K measured, if one considers a Mach number of 1-1.5 at a distance of 4.3 nozzle diameters, the region where this temperature was measured. Therefore, considering that in this region the void fraction is practically one, the temperature rise must be reduced to about 300K.

Looking at the numerical results, the maximum static temperature calculated for the higher pre-exponential factor assumed ($k_0 = 1 \cdot 10^{11} m^3 \cdot (mol \cdot s)^{-1}$) corresponds to a temperature rise of 250K in the gas phase (considering the initial CO₂ temperature of 750K) and 330K in the liquid phase (considering the initial sodium temperature of 773K). The peak in the gas static temperature is found at an axial distance of about 11-12-nozzle-diameters, whereas the maximum temperature in the liquid phase is reached at 4-nozzle-diameters. However, looking at the corresponding calculated void fraction profiles reported in figure 6.6, it is likely to assume that, up to a distance of 12-nozzle-diameter distance, the temperature experimentally measured corresponds to the gas phase temperature, since a very low liquid fraction exists at this distance. For the same reason, it can be stated that the numerical profile of the liquid phase temperature is meaningless for a distance lower than 10-nozzle-diameters. The calculated liquid temperature profile even very close to the nozzle derives from the fact that the gas volume fraction is exactly 1 only at the inlet boundary (where this is imposed as boundary condition): starting from this point, a minimum liquid fraction is calculated by the model. This fraction is meaningless: at 2-nozzle-diameters it is equal to 0.1%, at 5-nozzle-diameter it is equal to 0.4%, at 8-nozzle-diameters it is equal to 0.7% (these order of magnitude are true for all the obtained results, independently on the specific pre-exponential factor adopted). Following these considerations, one can conclude that considering the liquid phase temperature profile for an axial distance lower than 10-nozzle-diameter is meaningless.

In order to perform a numerical-experimental comparison, the results obtained with the pre-exponential factor equal to $k_0 = 1 \cdot 10^{10} m^3 \cdot (mol \cdot s)^{-1}$ and $k_0 = 1 \cdot 10^{11} m^3 \cdot (mol \cdot s)^{-1}$ are taken into account, since they are the ones giving a temperature rise closer to the one obtained experimentally by Gicquel. As a first observation, one can notice that the calculated centerline temperature profile is not as sharp as the one measured by Gicquel (figure 6.4), with a sudden temperature peak followed by a very quick cooling. The region where the maximum temperatures are reached, as well as the cooling region, are more similar to the experimental profiles found by Sekkouti: he measured the maximum temperature for an axial distance going from about 10- to 20-nozzle-

diameters, whereas in the numerical results here presented this maximum lies between 10- and 15-nozzle-diameters. In the Gicquel's results, the temperature peak was measured only at an axial distance of 4.3-nozzle-diameters.

As expected, the increasing of the reaction rate (through the pre-exponential factor) leads to a shift of the CO₂ total consumption towards the nozzle: this can be observed in figure 6.6, which shows how the void fraction begins to significantly decrease and finally approaches zero at a lower axial distance, for an increasing of the pre-exponential factor.

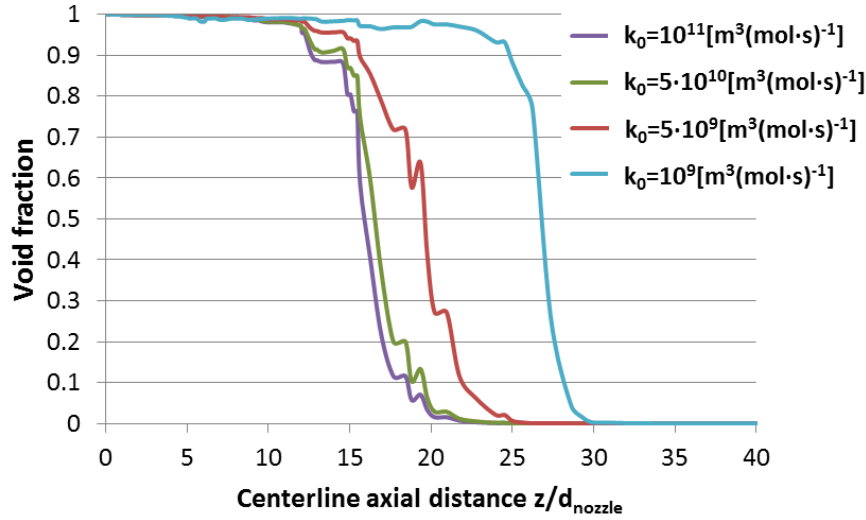


Figure 6.6: Void fraction along the jet centerline, as a function of the chemical reaction rate (through the pre-exponential factor k_0).

Figures 6.8, 6.9, 6.10 and 6.11 show the numerical radial temperature profiles, for the case of $k_0 = 1 \cdot 10^{10} \text{ m}^3 \cdot (\text{mol} \cdot \text{s})^{-1}$.

Let's consider, first, the gas phase (i.e. the CO₂): as expected, close to the nozzle, the gas static temperature decreases due to the underexpansion; this can be observed for an axial distance up to 6 nozzle diameter, at the centerline ($r = 0$), since the gas temperature results lower than the injection temperature, which is 750K (475°C). Starting from a 7-nozzle-diameter distance, the gas temperature gradually increases, until reaching its maximum value at 12 nozzle-diameters. It is interesting to notice that, for $r/d_{nozzle} < 9$, the temperature at the jet border ($r/d_{nozzle} = \pm 2$) is higher than on the centerline: in fact, as it can be seen from figure 6.7, this is the region where the gas-liquid interface lies, and, thus, where the reactants can chemically react. This can also be observed in figure 6.12, which show the numerical contours of gas and liquid temperature, obtained for $k_0 = 1 \cdot 10^{10} \text{ m}^3 \cdot (\text{mol} \cdot \text{s})^{-1}$.

The liquid phase profile is qualitatively similar to that of the gas phase. The region where $r/d_{nozzle} < 10$ is practically meaningless, since it is characterized by an insignificant quantity of liquid, as it can be seen from figure 6.6. The liquid gradually heats until its maximum temperature, reached at 11 nozzle diameters. Starting from this distance, the cooling down region begins.

Figure 6.13 shows the calculated contour of void fraction, for $k_0 = 1 \cdot 10^{10} \text{ m}^3 \cdot (\text{mol} \cdot \text{s})^{-1}$.

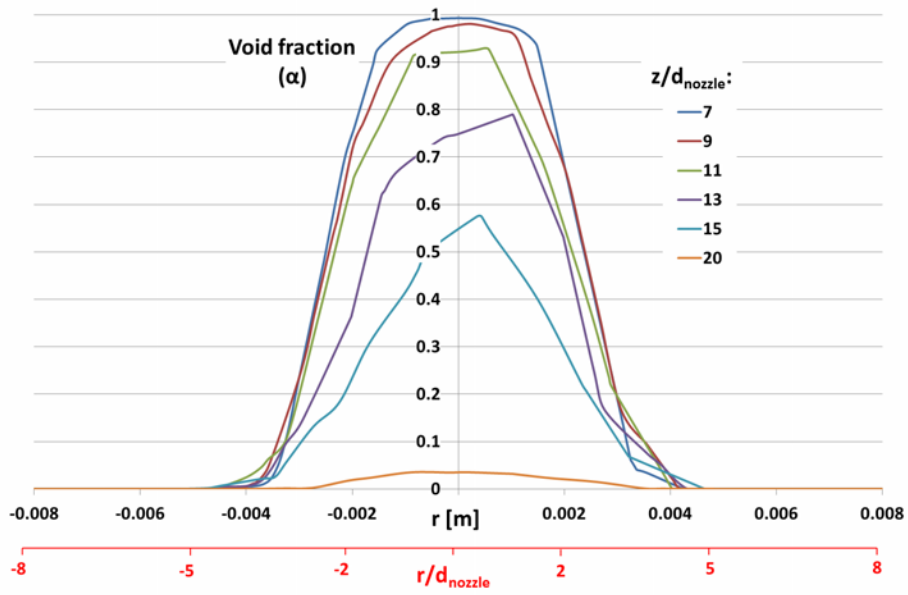


Figure 6.7: Radial void fraction profile, for $7 \leq r/d_{\text{nozzle}} \leq 20$, for the case of $k_0 = 1 \cdot 10^{10} \text{ m}^3 \cdot (\text{mol} \cdot \text{s})^{-1}$

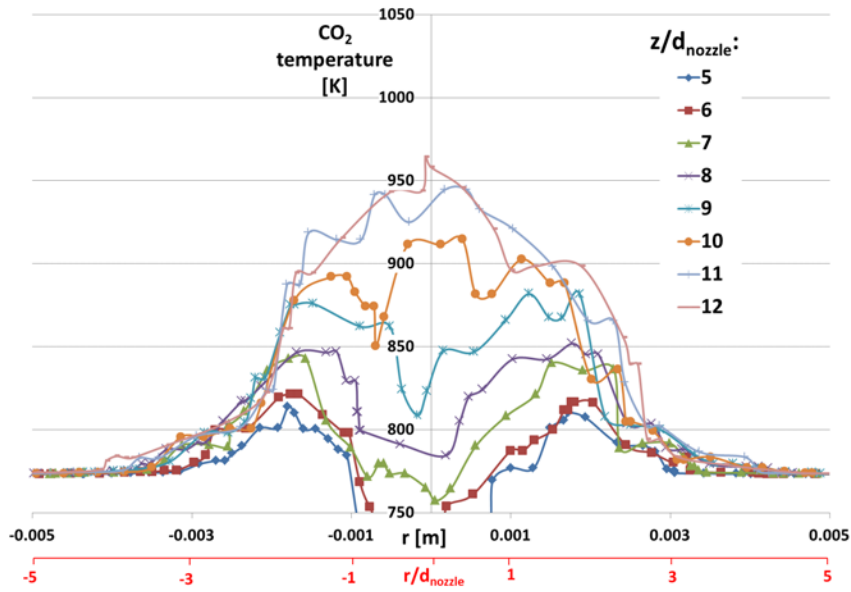


Figure 6.8: Radial CO₂ temperature profile, for $5 \leq r/d_{nozzle} \leq 12$, for the case of $k_0 = 1 \cdot 10^{10} \text{ m}^3 \cdot (\text{mol} \cdot \text{s})^{-1}$

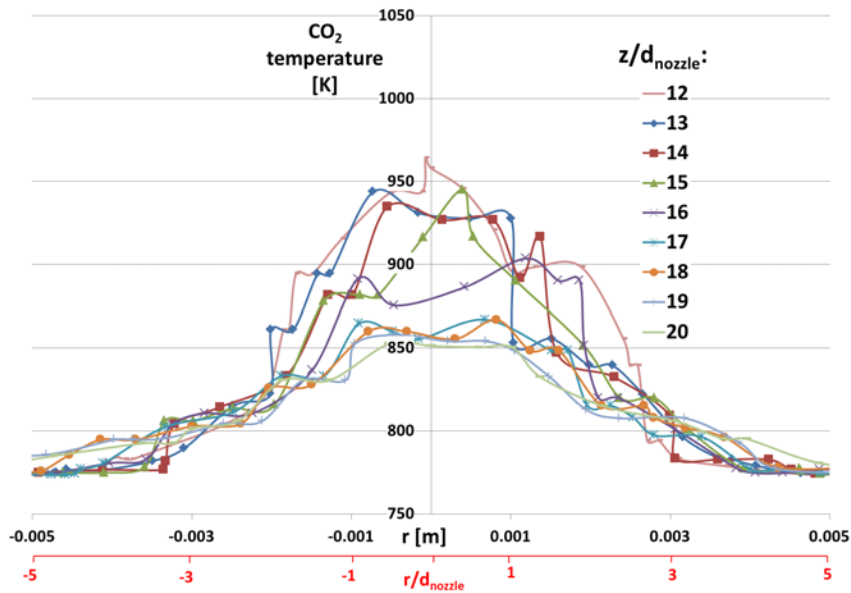


Figure 6.9: Radial CO₂ temperature profile, for $12 \leq r/d_{nozzle} \leq 20$, for the case of $k_0 = 1 \cdot 10^{10} \text{ m}^3 \cdot (\text{mol} \cdot \text{s})^{-1}$

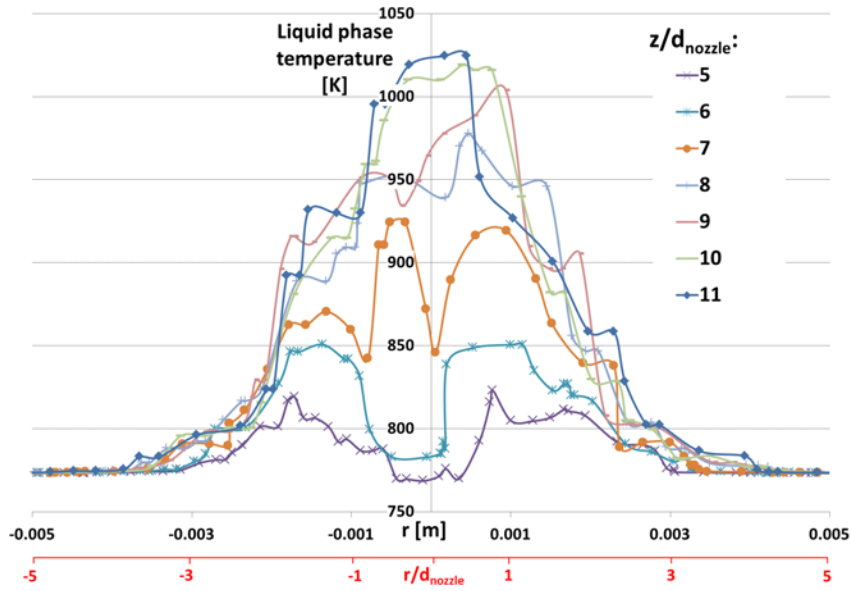


Figure 6.10: Radial liquid phase temperature profile, for $5 \leq r/d_{nozzle} \leq 11$, for the case of $k_0 = 1 \cdot 10^{10} \text{ m}^3 \cdot (\text{mol} \cdot \text{s})^{-1}$

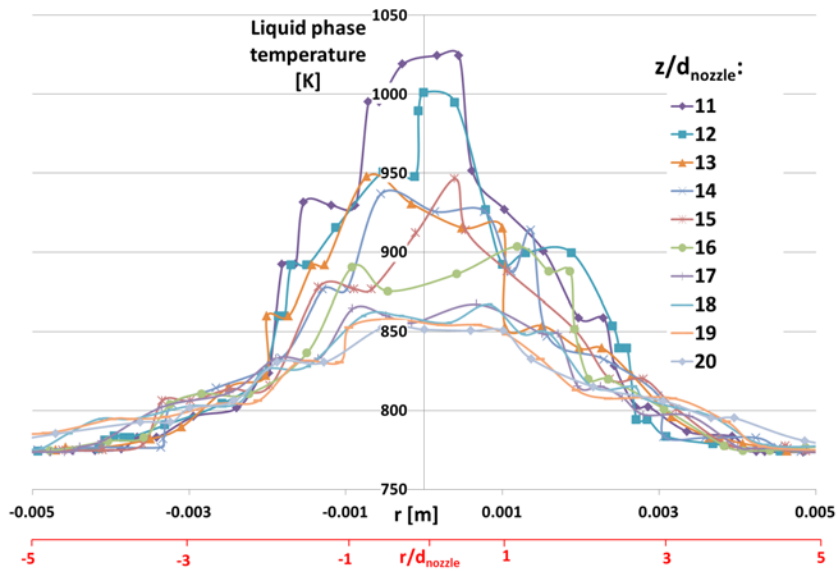


Figure 6.11: Radial liquid phase temperature profile, for $11 \leq r/d_{nozzle} \leq 20$, for the case of $k_0 = 1 \cdot 10^{10} \text{ m}^3 \cdot (\text{mol} \cdot \text{s})^{-1}$

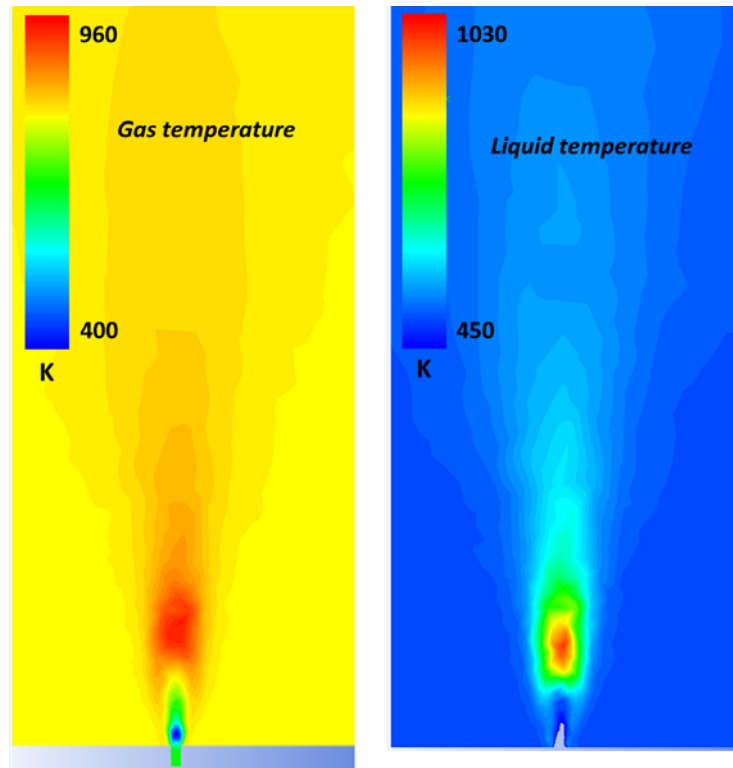


Figure 6.12: Contours of gas and liquid phase temperature, calculated for $k_0 = 1 \cdot 10^{10} \text{ m}^3 \cdot (\text{mol} \cdot \text{s})^{-1}$. For the liquid phase, the region close to the nozzle is out of range (however, one should remember that liquid temperature in this region is meaningless, due to practically zero liquid volume fraction).

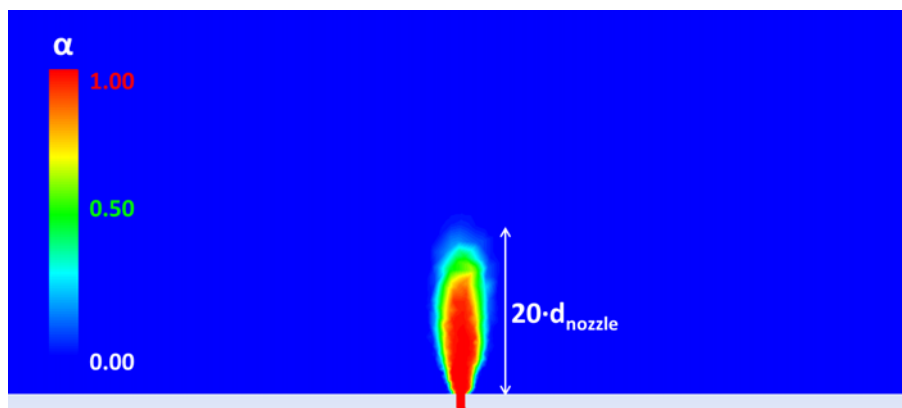


Figure 6.13: Contours of void fraction, calculated for $k_0 = 1 \cdot 10^{10} \text{ m}^3 \cdot (\text{mol} \cdot \text{s})^{-1}$.

Conclusions and perspectives

Conclusions

The goal of this PhD work was the developing of a numerical approach able to describe the evolution of an underexpanded reactive CO₂-into-liquid-sodium jet. Such a numerical model is required in order to evaluate the consequences of an accidental leakage scenario, inside the Na-CO₂ heat exchanger of an SFR coupled with a supercritical CO₂ Brayton cycle.

The first part of the work was dedicated to the comprehension of the specific two-phase flow regimes occurring in an underexpanded gas-into-liquid jet. The application of the available two-phase regime maps and the visual experimental results obtained, suggest that this kind of two-phase jets features mist flow close to the nozzle outlet, whereas the gas phase breaks up further downstream the jet axis, leading to high void fraction bubbly flow. Beside this aspect, the main specific feature of the considered two-phase flow is the high velocities encountered: gas leaves the nozzle at sonic conditions, then it suddenly accelerates to supersonic speeds, due to the underexpansion. Therefore, the numerical model needs to be able to represent void fractions from zero to one, with flow regime transition, and with high Mach numbers in the gas phase, which is a critical issue to be treated numerically.

A two-fluid Euler-Euler approach has been developed, using the commercial CFD package Ansys Fluent. A specific interfacial friction and heat transfer model, which takes into account the droplet to bubbly flow transition, has been implemented inside Fluent. A dedicated work has been done in order to estimate proper mean diameters and drag coefficients of the dispersed phases. An experimental facility has been built with the aim of measuring void fraction inside underexpanded gas-into-water jets, employing optic probe technique for the gas-liquid phase discrimination. The numerical results have been compared to the experimental results obtained inside underexpanded N₂-into-water jets, and show consistency in terms of axial and radial void fraction profiles.

Once the purely fluid-dynamic model was validated, a transposition to the specific CO₂-into-liquid-sodium case had to be realized. In order to that, the first aspect to treat was the study of the CO₂-Na chemical interactions. Based on the assumptions concerning the two-phase regimes and the dispersed phase dimensions inside underexpanded gas-into-liquid jets, a consistent model for the CO₂-Na chemical reaction has been developed: it considers the reaction between a sodium droplet with the surrounding CO₂ environment, inside the region where mist flow is assumed, and between a CO₂ bubble with the surrounding Na environment, inside the region where bubbly flow is assumed.

The model treats a single droplet (or bubble) depletion. Thus, the droplet (or bubble) reaction rate, as a function of the influencing parameters (such as temperature and Arrhenius pre-exponential factor), could be obtained.

At this point, the data obtained through the droplet (or bubble) chemical reaction model, had to be implemented inside the two-fluid approach, in order to develop a complete model of the reactive CO₂-into-Na jet. The coupling between the two models have been realized through the addition of source terms inside the constitutive equations of the two-fluid Euler-Euler model. These source terms take into account the mass, momentum and energy transfer between the phases, as a function of the reactant reaction rate. The total reaction rate, inside a computational cell, was determined through the single droplet (or bubble) chemical reaction model, employing different kinetics parameter (i.e. the pre-exponential factor of the Arrhenius equation).

Comparing the numerical temperature profiles with the available experimental data, the kinetics of reaction could be estimated. The present work focused on the Na-CO₂ chemical reaction occurring for temperatures higher than 460-500°C. For these operating conditions, the following Arrhenius expression is the one which allows the closest similarity between the numerical and experimental results:

$$k = k_0 \cdot \exp\left(\frac{-E_a}{RT}\right)$$

Where $k_0 = 1 \cdot 10^{11} \text{ m}^3 \cdot (\text{mol} \cdot \text{s})^{-1}$ and $E_a = 4 \cdot 10^4 \text{ J/mol}$.

Perspectives

Experimental tests

The Na-CO₂ interaction facility developed by the CEA, described in chapter 3, has been deeply utilized during this work: unfortunately, no exploitable results could be obtained. In fact, the DISCO2 facility has remained out work for a long time, due to several technical reasons, ranging from thermocouple replacement, to sodium plugging in different parts, to software problems. When all the problems were fixed and the facility was finally working, three CO₂-into-sodium tests were performed in 2013, with sodium at 500°C and CO₂ at 480°C. The temperature values recorded during these tests have shown the evidence of major problems in the thermocouples placed on the comb, since almost no temperature variation was recorder by them during the CO₂ injections. The replacement of thermocouples inside the comb was considered unfeasible with regard to the PhD scheduled deadlines.

Therefore, the current available experimental data on temperature profiles inside underexpanded CO₂-into-sodium jets, are the ones obtained by Gicquel, who employed exactly the same experimental facility. In chapter 6, it has been discussed the difficulty of interpreting these results, due to the complicate temperature measurement inside a high speed flow and to the fact that only a single measurement has been realized for each initial sodium/CO₂ temperature. In order to perform a more rigorous numerical-experimental result comparison,

more experimental data have to be investigated. Moreover, a dedicated study should be performed in order to comprehend the flow-single-thermocouple and the flow-thermocouple-comb interactions inside the facility and, thus, decrease the uncertainties on the measured temperature profiles. From this point of view, a validation of the temperature measured by the thermocouples could be performed employing a non-reactive single phase gas flow. For such a flow, reliable numerical results could be obtained using a CFD approach for the simulation of the entire nozzle and thermocouple comb system.

Transposition to the real pressure conditions

In the available experimental results on Na-CO₂, CO₂ pressure never exceeds 1.0 MPa. Following the goal of the present work, which was the numerical validation through experimental results, also the numerical simulations were run using this value of pressure. However, for a transposition to the real operating conditions, higher pressure must be considered. CO₂ pressure inside the heat exchanger is about 25.0 MPa, meaning that, in case of leakage, the sonic pressure of the CO₂ flowing into the sodium would be around 13.5 MPa: at these thermodynamic conditions, CO₂ is still supercritical (its critical pressure and temperature are 7.29 MPa and 31.3°C). In this case, the ideal gas law employed in the present work would not be applicable, and it would be required to replace it by a proper density law. Moreover, a further complication derives from the fact that, during underexpansion, CO₂ pressure decreases from 13.5 MPa to the sodium pressure, meaning that a supercritical-to-subcritical condition transition occurs. In order to properly take into account this issue, a specific CO₂ density law needs to be developed.

Improvement of the numerical two-fluid approach

Some improvements should be investigated regarding the numerical approach. The main assumption retained in this work was that droplet-to-bubbly flow transition could be modeled using an interpolation between these two regime flows, without using the correlations for churn flows. This approach, adopted and validated in literature, prevents from defining an intermediate churn flow, which would complicate the numerical modeling for two main reasons: the first is that one new mean dispersed flow dimension would be required, the second is that, since the characteristic dimensions of the dispersed flow in a churn regime is some order of magnitude higher than in bubbly flow, this could cause limitation to the mesh refinement (since, in an Euler-Euler description, the dispersed flow dimensions must always be lower than the computational cell size). Nevertheless, even keeping the assumption of not directly considering churn flow, some improvements could be achieved by employing an interfacial area transport approach. For the specific case of underexpanded gas-into-liquid jets, the difficulty of employing such an approach is linked to the two-phase regime transition: interfacial area transport equations have been employed for purely bubbly (or droplet) flows, where the interfacial area transport of a single phase needs to be solved. In the case where a droplet-to-bubbly regime transition occurs, a single transport of interfacial area for one phase is no longer sufficient.

Tobita et al. [42] implemented a multi-phase, multi-component, interfacial area transport inside the SIMMER-III code. The flow map regime adopted in SIMMER-III has been discussed in chapter 4, and it employs the same approach which has been adopted in the present work: bubbly flow for low void fractions, dispersed flow for high void fractions and transition flow between them at intermediate void fractions. Following the approach employed by Tobita et al., two interfacial areas, with their respective transport equations, should be defined: one for the droplets in the mist flow, one for the bubbles in the bubbly flow. In addition, the boundary area between the bubbly and the mist region must be defined. Tobita et al. also defined the transfer rate of interfacial area from the bubbly to the dispersed region.

Even if physically more consistent than assuming a constant dispersed phase dimension, one can understand the significant increase of complexity that an implementation of interfacial area transport equations would cause. Furthermore, the source terms in the transport equations for the interfacial areas, which take into account break-up and coalescence (besides transfer rate of interfacial area from the bubbly to the dispersed region), would need to be investigated in order to verify their applicability for the specific high velocity flow encountered in underexpanded gas-into-liquid jets. However, the implementation of an interfacial area transport approach surely represents a solution to be investigated in order to further improve the consistency of the numerical results.

Another possible improvement could be achieved by employing a multi-field approach: for example, a three-field approach may be investigated, with one field describing the gas phase, one field dedicated to the continuous liquid phase and one field dedicated to the droplet liquid phase.

The present model only considers drag force for the calculation of the interfacial friction. In order to check the validity of this assumption, an estimation of the virtual mass to drag force ratio can be evaluated along the jet axis. For the calculation of the virtual mass force through equation 4.17, two adjacent cells on the jet axis have to be considered for estimating the acceleration of each phase and the velocity gradients. Applying equation 4.17 along the axial distances (considering only the gradient in the axial direction) and comparing the results to the calculated drag force, it is found that, for the droplet flow region (void fraction higher than 80%), the F_{VM}/F_D ratio does not exceed the 20%, with an average value lower than 10%. Nevertheless, it is found that the ratio F_{VM}/F_D is significantly higher for the bubbly flow region (void fraction lower than 50%), where the virtual mass force can locally have the same order of magnitude of the drag force.

Even having in mind that these are estimations and not exact calculations of the virtual mass force, this suggests that the accounting of the virtual mass effect could be important for the bubbly flow region. Considering the goal of the present work, virtual mass is not supposed to play an important role, since, how it was shown in paragraph 6.3, the bubbly flow region is very limited inside the reactive CO₂-into-sodium jet. However, in case of employing the present numerical model for the investigation of non-reactive gas-into-liquid jets over a large computational domain (where bubbly flow would characterize a significant part of it), the influence of the virtual mass effect should be investigated. Of course, besides the need of employing a proper closure law, the problem of

numerical instabilities connected with the virtual mass calculation (discussed in paragraph 4.2.5) must be overcome in order to have numerical converged results when including the virtual mass effect.

Another important issue concerns the turbulence modeling. As detailed in paragraph 4.1.5, a standard two-equation $k - \varepsilon$ model has been employed for the gas-liquid mixture of the underexpanded gas-into-liquid jet. It is however known in literature that, in high strain rate regions, eddy viscosity models tend to over-predict turbulent kinetic energy. Pope [74] was the first author who discussed this issue, finding that the $k - \varepsilon$ model over-predicts the spreading and decay rate of a round jet flow. Durbin [75] investigated the over-prediction of turbulence kinetic energy in high strain rate regions, referring this problem to “stagnation point anomaly”, finding that these higher values of k are due to an overestimate of production term P_k . Through testing of a steady jet flame, Buckrell [76] observed that the flow-field calculations performed adopting the typical $k - \varepsilon$ model lead to an over-prediction of spreading and, thus, an under-prediction of penetration.

In these cases, in order to improve the accuracy of the two-equation turbulence models, the turbulence constants $C_{1,\varepsilon}$ and $C_{2,\varepsilon}$ may be modified, as they are responsible for the generation/destruction of the turbulent energy dissipation. An alternative, mathematically and physically more rigorous, method has been proposed by Durbin [75, 77], who demonstrated that the turbulence production cannot violate the condition:

$$P_k \leq 2\rho k \sqrt{\frac{2|S_{ij}S_{ij}|}{3}} \quad (6.36)$$

The inequality 6.36 also suggests that the turbulence production should increase linearly with the mean strain tensor. However, following the eddy viscosity constitutive model, the turbulence production is calculated as:

$$P_k = 2\mu_t S_{ij} S_{ij} \quad (6.37)$$

which means that turbulence production increases quadratically with the mean strain rate. Inserting equation 6.37 into 6.36, the following bound for the turbulent viscosity is obtained:

$$\mu_t \leq \frac{2\rho k}{\sqrt{6}S_{ij}} \quad (6.38)$$

Using a timescale $T = k/\varepsilon$ and the definition of the turbulent viscosity, one obtains $\mu_t = C_\mu \rho k T$. Thus, equation 6.38 can be written as timescale bound:

$$T \leq \frac{2}{\sqrt{6}C_\mu S_{ij}} \quad (6.39)$$

Which is the analogous result that Durbin [75] derived as a realizability condition. It can be demonstrated [75] that the realizability constraint for Reynolds stress tensor to be definite positive, leads to the stronger constraint:

$$T \leq \frac{1}{\sqrt{6}C_\mu S_{ij}} \quad (6.40)$$

Which can be met adopting the following limiter:

$$T = \frac{\mu_t}{C_\mu \rho k} = \min \left(\frac{k}{\varepsilon}, \frac{\alpha}{\sqrt{6}C_\mu S_{ij}} \right) \quad (6.41)$$

The bound 6.40 is satisfied for any $\alpha \leq 1$.

The value $\alpha = 0.6$ was selected and validated by Behnia et al. for an elliptic relaxation turbulence model ($v^2 - f$ model) [78], for simulate the flow and heat transfer in circular confined and unconfined impinging jet configurations. Following these results, Medic and Durbin [79] applied the same value of α for the $k - \varepsilon$ and validated it for the computations of turbulent flow in a transonic turbine passage.

Adopting the same parameters employed for obtaining the results reported in paragraph 4.2, the correction 6.41 to the turbulent viscosity has been implemented inside the two-phase mixture $k - \varepsilon$ model employed for all the previous simulations reported in this work, described in paragraph 4.1.5. Referring to equation 6.41, it was assumed $\alpha = 0.7$ (a purely first try value). Figure 6.14 shows a comparison between the results reported in paragraph 4.2, employing the standard turbulent viscosity definition, and exactly the same simulation, but with the adoption of the formulation 6.41 for the evaluation of the turbulence viscosity. As it was expected, the modified formulation of the turbulence production limits the spreading rate and, as a consequence, the gas penetration is higher.

A validation of the proper value of α may be obtained performing a simulation of single-phase underexpanded round gas jets, in order to understand the consistent turbulence production expression to be employed for underexpanded gas-into-liquid jets. In fact, no validation on the α value has been realized on free jets yet.

Improvement of the chemical reaction model

The chemical reaction models, that have been developed in order to evaluate the sodium droplet and the CO_2 bubble depletion rates, are based on the assumption of an Arrhenius-type reaction rate:

$$k = k_0 [Na]^a [CO_2]^b$$

Moreover, following the results obtained by Gicquel [15], a first order of reaction for both Na and CO_2 has been retained, meaning the $a = b = 1$. The first order with respect to the CO_2 concentration was determined experimentally

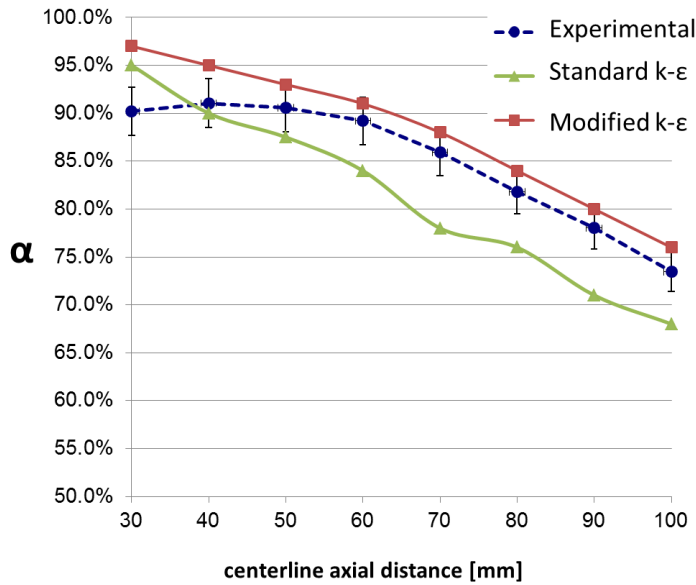


Figure 6.14: Comparison between the results obtained adopting the standard turbulent viscosity definition in the $k - \epsilon$ model and the results obtained with the modified turbulent viscosity proposed by Durbin [75].

by Gicquel, for temperatures lower than 500°C. However, the validity of this assumption for higher temperature has to be investigated. Furthermore, the order with respect to the sodium vapor concentration should be confirmed, since it was not directly investigated experimentally.

Therefore, an important future study should be aimed at determining the exact values of the order of reaction for the two reactants.

Taking into account of the solid phase

The main products of the Na-CO₂ chemical reaction are C and Na₂CO₃. In the present work, the assumption that these products are in liquid phase is taken, in order not to further increase the complexity of the numerical approach and because of the lack of knowledge about the solid phase dimensions.

Even keeping a two-phase gas-liquid description, the effects of the solid products could be investigated in terms of their influence on the diffusion mechanism between gaseous reactants in the particle reaction process.

An important aspect to be investigated in the future is the time and space distribution of the solid products inside the heat exchanger, following a leakage scenario, since they could lead to plugging issues. The present model could provide the initial concentration profiles of the reaction products, as the starting point for the evaluation of the nucleation, growth and agglomeration processes of the solid products. For this reason, a dedicated study on the nucleation, growth and agglomeration processes would be useful for the future application of the present model.

Bibliography

- [1] IAEA. <http://www.iaea.org/programmes/a2/index.html>.
- [2] NEI. <http://www.nei.org/resourcesandstats/documentlibrary/reliable-andaffordableenergy/graphicsandcharts/>.
- [3] DOE/EIA-0484(2011). International energy outlook 2011, 2011.
- [4] G. Capus. Que savons nous des ressources mondiales d'uranium. les clefs du CEA no 55, Systemes nucleaires du futur, Generation IV, 2007.
- [5] World Nuclear Association. <http://www.world-nuclear.org/info/current-and-future-generation/fast-neutron-reactors>.
- [6] A.M. Judd et al. The under-sodium leak in the PFR superheater 2, February 1987. *Nucl. Energy*, 3:221–230, 1992.
- [7] R.N. Newman and C.A. Smith. Sodium/water combustion and the chemistry of wastage at sodium/water leak sites. *Journal of Nuclear Materials*, 52:173–183, 1974.
- [8] J.H. Eoh et al. Wastage and self-plugging by a potential CO₂ ingress in a supercritical CO₂ power conversion system of an SFR. *Journal of NUCLEAR SCIENCE and TECHNOLOGY*, 47:1023–1036, 2010.
- [9] S. Kishore et al. An experimental study on impingement wastage of Mod 9Cr 1Mo steel due to sodium water reaction. *Nuclear Engineering and Design*, Volume 243:49–55, 2012.
- [10] F. Beauchamp et al. Cooperation on impingement wastage experiment of mod. 9Cr-1Mo steel using SWAT-1R sodium-water reaction test facility. In *Int. Conf. on Fast React. and Related Fuel Cycles: Safe Technol. and Sustainable Scenarios, Paris, FR13 4-7, ID 41987 (T1-CN-199)*, 2013.
- [11] L. Cachon et al. Innovative power conversion system for the French SFR prototype, ASTRID. *Proceedings of ICAPP 2012, Chicago, USA, June 24-28 June 2012*.
- [12] J. Floyd et al. A numerical investigation of the sCO₂ recompression cycle off-design behaviour, coupled to a Sodium cooled Fast0 Reactor, for a seasonal variation in the heat sink temperature. *Nuclear Engineering and Design*, 260:78–92, 2013.

- [13] N. Alpy et al. Gas cycle testing opportunity with ASTRID, the French SFR prototype. In *Supercritical CO₂ Power Cycle Symposium, May 24-25, 2011, Boulder, Colorado*.
- [14] Anton Moiseyev and James J. Sienicki. Investigation of alternative layouts for the supercritical carbon dioxide brayton cycle for a Sodium-cooled Fast Reactor. *Nuclear Engineering and Design*, Volume 239:1362–1371, 2009.
- [15] L. Gicquel. *Etude des mécanismes et cinétiques des interactions sodium CO₂. Contribution à l'évaluation d'un système de conversion de l'énergie au CO₂ supercritique pour les réacteurs rapides à caloporteur sodium*. PhD thesis, 2010.
- [16] W.H. Gunther. *Sodium technology*. Atomic International, North American Rockwell, California, 1970.
- [17] Flow Structures of Gaseous Jets Injected into Water for Underwater Propulsion. J.n. Tang et al. In *49th AIAA Aerospace Sciences Meeting including the New Horizons Forum and Aerospace Exposition, 4 - 7 January 2011, Orlando, Florida*.
- [18] E. Loth and G.M. Faeth. Structure of underexpanded round air jets submerged in water. *Int. J. Multiphase Flow*, 15:589–603, 1989.
- [19] E. Loth and G.M. Faeth. Structure of plane underexpanded air jets into water. *AIChE Journal*, 36, 1990.
- [20] V.A. Surin, V.N. Erchenko, and V.M. Rubin. Propagation of a gas jet in a liquid. *J. Eng. Phys.*, 45, 1983.
- [21] M. Epstein, H. K. Fauske, and N. Yoshioka. Establishment of analytical model for peak temperature within a sodium-water reaction jet, (II) mean droplet size in a submerged gas jet. *Journal of Nuclear Science and Technology*, 42:961 – 969, 2005.
- [22] H. Kudoh et al. Visualization on the behavior of inert gas jets impinging on a single glass tube submerged in liquid sodium. *Journal of Nuclear Science and Technology*, 50:72–79, 2013.
- [23] N. Sekkouti. *Caractéristiques thermiques d'un jet réactif vapeur d'eau - sodium liquide modélisation monodimensionnelle de la température dans le jet*. PhD thesis, Université de Poitiers, 1985.
- [24] T. Takata and A. Yamaguchi. Numerical approach to the safety evaluation of sodium-water reaction. *Journal of NUCLEAR SCIENCE and TECHNOLOGY*, 40, No. 10:708–718, 2033.
- [25] T. Takata et al. Computational methodology of sodium-water reaction phenomenon in steam generator of Sodium-cooled Fast Reactor. *Journal of NUCLEAR SCIENCE and TECHNOLOGY*, 46, No. 6:613–623, 2009.
- [26] G. J. Wilson and M.S. Kazimi. Development of models for the sodium version of the two-phase three dimensional thermal hydraulics code THERMIT. *Energy Laboratory Report*, No. MIT-EL 80-010, 1980.

- [27] W.C. Rivard and M.D. Torrey. Numerical calculation of flashing from long pipes using a two-field model. *LASM LAMS-NUREG-6330*, 1976.
- [28] H. Ninokata and T. Okano. SABENA: An advanced subchannel code for sodium boiling analysis. *Proc. 3rd Int. Mtg. on Reactor Thermal Hydraulics, Newport, Oct. (1985)*.
- [29] A. Uchibori, A. Watanabe, and H. Ohshima. Numerical analysis of supersonic gas jets into liquid pools with or without chemical reaction using the SERAPHIM program. *Nuclear Engineering and Design*, 249:35–40, 2011.
- [30] *RELAP5-3D[®] CODE MANUAL VOLUME IV: MODELS AND CORRELATIONS*, The RELAP5-3D[®] Code Development Team (2005).
- [31] S. Kim, J.H. Eoh, and S. Kim. Development of a numerical analysis methodology for the multi-dimensional and multi-phase phenomena of a sodium-water reaction in an SFR steam generator. *Annals of Nuclear Energy*, 34:839–848, 2007.
- [32] S.S. Gulawani et al. CFD simulation of flowpattern and plume dimensions in submerged condensation and reactive gas jets into a liquid bath. *Chemical Engineering Science*, 63:2420–2435, 2008.
- [33] S. Miyaharaa, H. Ishikawac, and Y. Yoshizawad. Experimental investigation of reaction behavior between carbon dioxide and liquid sodium. *Nuclear Engineering and Design*, 241:1319–1328, 2011.
- [34] J.H. Eoh et al. Sodium-CO₂ interaction in a supercritical CO₂ power conversion system coupled with a Sodium Fast Reactor. *Nuclear Technology*, 173, 2011.
- [35] M. Ishii and K. Mishima. Two-fluid model and hydrodynamic constitutive relations. *Nuclear E*, 82:107–126, 1984.
- [36] G.F. Hewitt and D.N. Roberts. Studies of two-phase patterns by simultaneous x-ray and flash photography. *UKAEA Report AERE M2159*, 1969.
- [37] R. Bell, B.E. Boyce, and J.G. Collier. The structure of a submerged impinging gas jet. *J. Brit. Energy Soc.*, 1972.
- [38] S. Someya, Y. Li, and K. Okamoto. An entrained droplet by an under-expanded gas jet into water. *15th Int Symp on Applications of Laser Techniques to Fluid Mechanics, Lisbon, Portugal, 05-08 July, 2010*, 2010.
- [39] M. Ishii. *Thermo-fluid dynamic theory of two-phase flow*. Collection de la Direction des Etudes et Recherches de Electricite de France, Eyrolles, Paris, France, 1975.
- [40] T.R. Auton. The lift on a spherical body in a rotational flow. *J. Fluid Mech.*, 218:183–199, 1987.
- [41] T.R. Auton. *The Dynamics of Bubbles, Drops and Particles in Motion in Liquids*. PhD thesis, University of Cambridge, 1988.

- [42] Y. Tobita et al. Interfacial area modeling for a multiphase, multicomponent fluid-dynamics code. In *Proceedings of The International Conference on Multiphase Flows 91 - Tsukuba*, 1991.
- [43] K. Morita et al. Applications of the SIMMER-III fast reactor safety analysis code to thermal interactions of melts with sodium and water. In *7th International Conference on Nuclear Engineering, Tokyo, Japan, April 19-23, 1999, ICONE-7250*, 1999.
- [44] M. Ahmad et al. CFD simulation of a stratified flow at the inlet of a compact plate heat exchanger. *Computational Methods in Multiphase Flow IV*, 56, 2007.
- [45] N. Mechtoua et al. Assessment of NEPTUNE CFD code for some free surface flows interesting fluvial hydraulic. In *7th International Conference on Multiphase Flow, ICMF 2010, Tampa, FL USA*, 2010.
- [46] C. Garnier, M. Lance, and J.L. Marie. Measurement of local flow characteristics in buoyancy-driven bubbly flow at high void fraction. *Experimental Thermal and Fluid Science*, 26:811–815, 2002.
- [47] Y. Taitel, D. Bornea, and A.E. Dukler. Modeling flow pattern transitions for steady upward gas-liquid flow in vertical tubes. *AIChE Journal*, 26, 3:345–354, 1980.
- [48] M. J. Walsh. Influence of particle drag coefficient on particle motion in high-speed flow with typical laser velocimeter applications. *NASA Technical Note D-8120*, 1976.
- [49] L. Schiller and Z. Naumann. Ver. deutsch ing. 1935.
- [50] H. Rusche and R.I. Issa. The effect of voidage on the drag force on particles, droplets and bubbles in dispersed two-phase flow. In *Japanese European Two-Phase Flow Meeting, Tshkuba, Japan*, 2000.
- [51] I. Roghair, M. Sintannaland, and H. Kuipers. Drag force on bubbles in bubble swarms. *Seventh International Conference on CFD in the Minerals and Process Industries CSIRO, Melbourne, Australia 9-11 December 2009*, 2009.
- [52] W. E. Ranz and W. R. Marshall. Evaporation from drops, I and II. *Chem. Eng. Prog.*, 48:141–146, 1952.
- [53] A.A. Troshko and Y.A. Hassan. A two-equation turbulence model of turbulent bubbly flows. *International Journal of Multiphase Flow*, 27:1965–2000, 2001.
- [54] D. Pflieger and S. Becker. Modelling and simulation of the dynamic flow behaviour in a bubble column. *Chemical Engineering Science*, 56:1737–1747, 2001.
- [55] B. E. Launder and D. B. Spalding. *Lectures in Mathematical Models of Turbulence*. 1972.

- [56] F. Birch and J.E. Eggers. A critical review of the experimental data on turbulent shear layers. Technical report, Tech. rep., NaSA SP 321, 1972.
- [57] D.C. Wilcox. *Turbulence Modeling for CFD*. DCW Industries, Inc., 2006.
- [58] S. Sarkar et al. The analysis and modeling of dilatational terms in compressible turbulence. *Journal of Fluid Mechanics*, 227:473–493, 1991.
- [59] S.A. Vasquez and V.A. Ivanov. A phase coupled method for solving multiphase problems in unstructured meshes. In *Proceedings of ASME FEDSM00: ASME 2000 Fluids Engineering Division Summer Meeting, Boston*.
- [60] S.V. Patankar. *Numerical Heat Transfer and Fluid Flow*. Hemisphere, Washington, DC, 1980.
- [61] C.M. Rhie and W.L. Chow. Numerical study of the turbulent flow past an airfoil with trailing edge separation. *AIAA Journal*, 21:1525–1532, 1983.
- [62] B.E. Launder and D.B. Spalding. The numerical computation of turbulent flows. *Comp. Methods Appl. Mech. Eng.*, 3:269–289, 1974.
- [63] P. Birkby and G.J. Page. Numerical predictions of turbulent underexpanded sonic jets using a pressure-based methodology. *Proceedings of the Institution of Mechanical Engineers, Part G: Journal of Aerospace Engineering*, 215:165–173, 2001.
- [64] *Ansys Fluent User's Guide, Release 14.0, 2011*.
- [65] J.O. Hinze. Fundamentals of the hydrodynamic mechanism of splitting in dispersion processes. *AIChE Journal*, 1:289–295, 1955.
- [66] A.N. Kolmogorov. On the disintegration of drops in a turbulent flow. *Dokl. Akad. Nauk. SSSR*, 66:825–828, 1949.
- [67] R. B. Bird, W.E. Stewart, and E.N. Lightfoot. *Transport Phenomena*. 2007.
- [68] John Buckmaster and Tadeo Takeno. *Mathematical modeling in combustion science*. Lecture notes in physics, 1995.
- [69] V. G. Levich Festschrift. *Physicochemical hydrodynamics*. Prentice Hall, 1962.
- [70] *Ansys Fluent Theory Guide, Release 14.0, 2011*.
- [71] K.T. Whittington. A tool to extrapolate thermal reentry atmosphere parameters along a body in trajectory space. Master's thesis, North Carolina State University, 2011.
- [72] R.D. Quinn and L. Gong. Real-time aerodynamic heating and surface temperature calculations for hypersonic flight simulation. *NASA Technical Memorandum 4222*, 1990.
- [73] J.A. Fay and F.R. Riddell. Theory of stagnation point heat transfer in dissociated air. *Journal of the Aeronautical Sciences*, 25:73–85, 1958.

- [74] S.B. Pope. An explanation of the round jet/plane jet anomaly. *AIAA Journal*, 16, 1978.
- [75] P.A. Durbin. On the k-epsilon stagnation point anomaly. *Int. J. Heat Fluid Flow*, 17:89–90, 1996.
- [76] A. Buckrell. Investigation of mixing models and finite volume conditional moment closure applied to autoignition of hydrogen jets. Master's thesis, University of Waterloo, 2012.
- [77] P.A. Durbin. Limiters and wall treatments in applied turbulence modeling. *Fluid Dyn. Res.*, 41, 2009.
- [78] M. Behnia, S. Parneix, Shabany, and P.A. Durbin. Numerical study of turbulent heat transfer in confined and unconfined impinging jets. *International Journal of Heat and Fluid Flow*, 20:1 – 9, 1999.
- [79] G. Medic and P.A. Durbin. Toward improved prediction of heat transfer on turbine blades. *Journal of Turbomachinery*, 124/187, 2002.

Annex 1. The integral approach for the bubble reaction

After having defined $u = \frac{\vartheta}{R}$ and $x = \frac{r}{R}$, equation 5.52 can be rewritten as follows:

$$\frac{R}{2D} \frac{dR}{dt} = \frac{k\rho s_1 R^2}{2DM_2} \int_u^1 \frac{x-u}{1-u} \left[1 - Y_{1,R} \frac{x-u}{1-u} \right] dx + \frac{1}{2(1-u)} \quad (6.42)$$

Defining $y = \frac{x-u}{1-u}$, 6.42 becomes:

$$\frac{R}{2D} \frac{dR}{dt} = \frac{k\rho s_1 R^2}{2DM_2} (1-u) \int_0^1 y [1 - Y_{1,R} y] dy + \frac{1}{2(1-u)} = \frac{k\rho s_1 R^2}{2DM_2} (1-u) \left(\frac{1}{2} - \frac{Y_{1,R}}{3} \right) + \frac{1}{2(1-u)} \quad (6.43)$$

Equation 6.43 can be written as:

$$A = B(1-u) \left(1 - \frac{2Y_{1,R}}{3} \right) + \frac{1}{2(1-u)} \Rightarrow B \left(1 - \frac{2Y_{1,R}}{3} \right) (1-u)^2 - 2A(1-u) + 1 = 0 \quad (6.44)$$

Let's consider, now, the boundary condition 5.48, which becomes:

$$-D \left[\frac{\partial Y_1}{\partial r} \right]_R - \frac{dR}{dt} (1 - Y_{1,R}) = 0 \Rightarrow -D \frac{Y_{1,R}}{R - \delta} - \frac{dR}{dt} (1 - Y_{1,R}) \Rightarrow \frac{R}{D} \frac{dR}{dt} = \frac{-Y_{1,R}}{(1 - Y_{1,R})(1 - u)} \quad (6.45)$$

Substituting 6.45 into 6.44, after rearrangement one obtains:

$$\frac{A^2}{B} = \frac{-\left(1 - \frac{2Y_{1,R}}{3}\right) Y_{1,R}^2}{4(1 - Y_{1,R})} = \frac{M_2}{2k\rho s_1 D} \left(\frac{dR}{dt} \right)^2 = \frac{M_2 R_0}{2k\rho s_1 D} \left(\frac{dR}{dt} \right)^2 \quad (6.46)$$

Considering the initial bubble radius, R_0 , and defining a characteristic diffusion time, $\tau_{diff} = R_0^2/D$, the 6.46 becomes:

$$\frac{A^2}{B} = \frac{M_2}{2k\rho s_1 \tau_{diff}} \left(\frac{d(R/R_0)}{d\left(\frac{t}{\tau_{diff}}\right)} \right)^2 \quad (6.47)$$

Now, through 6.46 and 6.47, one obtains:

p

$$\frac{-\left(1 - \frac{2Y_{1,R}}{3}\right) Y_{1,R}^2 s_1}{2(1 - Y_{1,R})} = \frac{\tau_{reac}}{\tau_{diff}} \left(\frac{d(R/R_0)}{dt'} \right)^2 \quad (6.48)$$

Where $\tau_{reac} = M_2/(k\rho)$ and $t' = t/\tau_{diff}$. From 6.45, one can write:

$$\frac{\frac{R}{R_0} d\left(\frac{R}{R_0}\right)}{dt'} = \frac{-Y_{1,R}}{(1 - Y_{1,R})(1 - u)} \quad (6.49)$$

Remembering that $u = \delta/R$, one can find:

$$\frac{R - \vartheta}{R_0} = \frac{Y_{1,R}}{(1 - Y_{1,R})} \left(\frac{\tau_{reac}}{\tau_{diff}} \right)^{\frac{1}{2}} \left[\frac{2(1 - Y_{1,R})}{-s_1 \left(1 - \frac{2}{3} Y_{1,R}\right) Y_{1,R}^2} \right]^{\frac{1}{2}} \quad (6.50)$$

Equation 6.50 corresponds to equation 5.53.

Annex 2. The integral approach for the droplet reaction

Equation 5.54, following the assumption of $v = 0$, can be written as:

$$\frac{1}{r^2} \frac{d}{dr} \left(r^2 \rho D \frac{dU}{dr} \right) = 0 \quad (6.51)$$

Integrating twice 6.51, one obtains:

$$U = M_2 s_2 Y_1 - M_1 s_1 Y_2 = \frac{c_1}{D\rho} \left(-\frac{1}{r} \right) + c_2 \quad (6.52)$$

c_1 and c_2 are integration constants.

Applying the boundary conditions in $r = R + \delta$, one obtains:

$$U = (U_{R+\delta} - c_2) \frac{R + \delta}{r} + c_2 \quad (6.53)$$

With $U_{R+\delta} = M_2 s_2 Y_{1,R+\delta} - M_1 s_1 Y_{2,R+\delta}$.

Considering the boundary conditions in $r = R$, equation 5.12 can be written as:

$$\left(1 - \frac{P_{sat}}{P} \right) \frac{Y_{1,R}}{M_1} = \frac{P_{sat}}{P} \frac{Y_{2,R}}{M_2} \quad (6.54)$$

Substituting 6.53 into 6.54, using the definition of U and rearranging, one obtains:

$$\frac{1}{M_1 s_2} \left[M_1 s_1 Y_2 + (U_{R+\delta} - c_2) \frac{R + \delta}{r} + c_2 \right] = \xi Y_2 \quad (6.55)$$

With $\xi = (P_{sat}/P) / (1 - P_{sat}/P)$.

In the paragraph 5.3.2 the expression for Y_2 was obtained (equation 5.57). Substituting 5.57 into 6.55, one can solve to obtain an expression for c_2 :

$$c_2 = c_{20} + c_{21}a_2$$

With:

$$c_{20} = U_{R+\delta} \frac{R+\delta}{\delta} - \frac{R}{\delta} (\xi M_1 s_2 - M_1 s_1) Y_{2,R+\delta}$$

$$c_{21} = \frac{R}{\delta} (\xi M_1 s_2 - M_1 s_1) \delta^2$$

Now, c_2 can be substituted into the conservation equation of Y_2 , equation 5.56 derived in paragraph 5.3.2. Doing that, after solving all the integrals, an equation of a_2 is found, which is of the type:

$$a_2^2 b_2 + a_2 b_1 + b_0 = 0$$

Where the coefficients b_2 , b_1 and b_0 are all known, since they are functions of known parameters. Therefore, a_2 can be determined and, in turn, c_2 .

Knowing a_2 , the profile of Y_2 as a function of r can be calculated, through equation 5.57. With c_2 , the value of U as a function of r can be found through equation 6.53. Finally, using the definition of U , the profile of Y_1 can be calculated.